January 2023

Meteorological Drivers Of Blowing Snow Events At Arm North Slope Alaska Site

Talia Dawn Kurtz

How does access to this work benefit you? Let us know!

Follow this and additional works at: https://commons.und.edu/theses

METEOROLOGICAL DRIVERS OF BLOWING SNOW EVENTS AT THE ARM NORTH
SLOPE ALASKA SITE

by

Talia Dawn Kurtz

Bachelor of Science, University of Nevada-Reno 2021

A Thesis

Submitted to the Graduate Faculty

of the

University of North Dakota

in partial fulfillment of the requirements

for the degree of
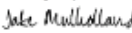
Master of Science

December

2023

Name: Talia Dawn Kurtz

Degree: Master of Science

        This document, submitted in partial fulfillment of the requirements for the degree from the University of North Dakota, has been read by the Faculty Advisory Committee under whom the work has been done and is hereby approved.
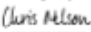
Aaron Kennedy

Jake Mulholland

JiangLong Zhang

_____

_____

_____

        This document is being submitted by the appointed advisory committee as having met all the requirements of the School of Graduate Studies at the University of North Dakota and is hereby approved.

Chris Nelson
Dean of the School of Graduate Studies

12/7/2023
_____
Date

PERMISSION

Title   Meteorological Drivers of Blowing Snow Events at ARM North Slope Alaska Site.

Department Atmospheric Sciences

Degree   Master of Science

In presenting this thesis in partial fulfillment of the requirements for a graduate degree from the University of North Dakota, I agree that the library of this University shall make it freely available for inspection. I further agree that permission for extensive copying for scholarly purposes may be granted by the professor who supervised my thesis work or, in his absence, by the Chairperson of the department or the dean of the School of Graduate Studies. It is understood that any copying or publication or other use of this thesis or part thereof for financial gain shall not be allowed without my written permission. It is also understood that due recognition shall be given to me and to the University of North Dakota in any scholarly use which may be made of any material in my thesis.

<div align="right">

Talia Dawn Kurtz
7 December 2023

</div>

TABLE OF CONTENTS

LIST OF FIGURES

LIST OF TABLES

ACKNOWLEDGEMENTS

ABSTRACT

Blowing snow is common in polar regions. Blowing snow and associated sublimation influence the surface energy budget and surface mass balance. For example, it is believed to play a critical role in the evolution of Arctic sea-thickness by reducing the amount of snow accumulated on the sea-ice surface, which is a pressing issue with the Arctic Amplification. Currently, most models do not include blowing snow as there has not been widespread validation of blowing snow parameterizations. Fortunately, the Atmospheric Radiation Measurements (ARM) North Slope Alaska (NSA) site located in Utqiaġvik, Alaska contains instrumentation that allows for the detection of this process. There are two objectives for this study. The first goal is to use particle size distribution (PSD) data from the Precipitation Imaging Package (PIP) and the Laser Precipitation Monitor (LPM) to identify periods of blowing snow at ARM NSA. This information is coupled to surface meteorological data to understand when blowing snow occurs. From this initial study, a long-term record of blowing snow frequency will be developed for the history of the NSA site. The second objective will identify meteorological regimes associated with blowing snow events. Synoptic patterns will be classified with Self Organizing Maps (SOMs). Collectively, this will give a climatology of blowing snow from January 1979 to February of 2022 for NSA. This study will determine the ability of the SOMs to classify weather patterns of specific atmospheric processes. Determining the weather patterns associated with blowing snow will allow for thorough validation of other modeling efforts. Eventually, this will lead to ample knowledge to confidently incorporate these schemes into weather and climate models. This will allow for better forecasting of reduced visibility conditions and allow for the inclusion of blowing snow in models that evaluate sea-ice evolution.

CHAPTER 1

INTRODUCTION AND BACKGROUND

1.1.Department of Energy Atmospheric Radiation Measurement Sites: North Slope of Alaska

Climate change is unequivocal and at the forefront of climate research. Physical changes in Earth's climate and atmosphere influence global economics, policy, and societal health (Hunt and Watkiss 2011). Understanding the physical processes that drive climate and climate change are critical for developing mitigation strategies. The Arctic is experiencing the brunt of climate change with warming rates exceeding the average global warming rate (Stamnes et al. 1999). The Arctic influences the thermohaline circulation (Broecker et al. 1988), ocean currents (Manabe et al. 1991), snow-ice albedo feedbacks (Budyko 1969), cloud-radiation feedbacks (Cury and Schramm 1993), and global radiative budgets (Stamnes et al. 1999). Large uncertainties exist in cloud-radiation, ocean-ice, and sea-ice albedo feedbacks and how such processes play into the global radiation budget in an evolving climate. In response to global climate change, the United States Department of Energy (DOE) has developed a network of atmospheric radiation measurement (ARM) sites to better observe the energy budget and related forcings including clouds and aerosols. Overall, the mission of ARM is to improve energy sustainability through global climate change research (Tobin et al. 2006).

ARM locations were selected to encompass a broad range of climates observed on Earth (Tobin et al. 2006). There are currently three fixed ARM locations including the Southern Great Plains (SGP) site in Lamont, Oklahoma, United States; the North Slope of Alaska (NSA) site in

Utqiaġvik, Alaska, United States; and the Eastern North Atlantic (ENA) site in Azores, Portugal. Each ARM site contains ground-based in-situ and remote sensing instruments. The ARM site in inquiry is NSA located within the Arctic Circle along the Beaufort and Chukchi Sea in Utqiaġvik, Alaska (Fig.1). NSA has been operational since 1997 (Zhang 2022).

NSA is one of the longest-term research facilities providing data and observations on Arctic and high-latitude processes (Berendes et al. 2004). Observations from NSA have been used in a wide variety of Arctic literature including the generation of aerosol vertical profiles (Zhang et al. 2022), satellite-to-surface-observation comparisons (Berendes et al. 2004), validation of radiosondes in the detection of cloud layers (Zhang et al. 2013), detecting ice production in supercooled Arctic Stratiform clouds (Zhang et al. 2017), theoretical derivation of cloud physical properties (Daniel et al. 2006), vertical motion within Arctic mixed-phase clouds and compounding relations with cloud physical properties (Shupe et al. 2008), and the generation of a 10-year record of seasonal variability in cloud fraction, radiative flux, and cloud radiative forcing (Dong et al. 2010). Like other high-latitude locations, NSA is prone to blowing snow due to the frequency of snowfall events, cold temperatures, and high winds. The diverse range of instrumentation and the high occurrence of blowing snow conditions makes NSA an ideal location for the analysis of blowing snow and associated processes.

NSA is composed of multiple instrumented locations including the NSA Central Facility (NSA C1), NSA E10, and Oliktok Point (Fig. 1). The NSA C1 site contains 43 instruments including radars, remote sensing instruments, and in-situ instruments (Zhang et al. 2022). NSA E10 is located north of NSA C1 and contains an on-site camera, an Eddy Correlation Flux Measurement System (ECOR; Cook and Sullivan 2020), a Surface Energy Balance System (SEBS; Sullivan et al. 2019), and a Laser Disdrometer (LDIS; Bartholomew 2020). Oliktok Point is located

between NSA and Prudhoe Bay along the Arctic coastline. The ARM Mobile Facility 3, AMF3, was placed in Oliktok Point from September 2013 to August 2021 and contained 50 instruments. Oliktok Point also offered special-use airspace for aircraft observations (de Boer et al. 2018).

NSA provides various instrumentation capable of detecting blowing snow. In-situ instrumentation includes optical laser distrometers as well as a digital video distrometer that provides particle concentrations for a range of particle diameters (Meshesha et al. 2016; Pickering et al. 2019). Traditional meteorological data, including temperature, relative humidity, wind speed, atmospheric pressure, and visibility, are also available. Finally, multiple radars and lidars are available. For example, ceilometers, which have been used to detect blowing snow (Gossart et al. 2017; Loeb and Kennedy 2021; Loeb and Kennedy 2023), are located at NSA C1, the supplementary Atqasuk site, and Oliktok Point. At NSA, Chen et al. (2022) used multiple methods to detect blowing snow including the use of a ceilometer and meteorological thresholds based on wind speed and temperature. A key issue with these earlier papers was lack of analyzed particle data to confirm the presence of blowing snow.

1.2 Blowing Snow

Within high-latitude and polar regions, snow particles are transported by the wind. Snow mass transport describes the process of snow particles at the surface being dislodged by the wind. Lofted snow particles are then redistributed through blowing and/or drifting snow. Blowing snow, as defined by the American Meteorological Society Glossary of Meteorology, is the lofting of snow particles from the surface into the atmosphere at a minimum height of 2-m with a reduction in horizontal visibility to less than 11-km. Similarly, Mahesh et al. (2003) defined blowing snow as "masses of fine snow particles carried by the wind to fill the near-surface atmospheric layer and to

limit the horizontal visibility." Drifting snow, as defined by the American Meteorological Society Glossary of Meteorology, is the lofting of snow particles 6-ft or less within the atmosphere.

1.2.1 Blowing Snow Mechanisms

Blowing snow is initiated by the dislodging of snow/ice particles at the surface into the near-surface layer by the wind. Specific wind speed thresholds must be met to generate a strong enough shear stress to counter particle bonding and resistance (Shulski and Seeley 2004). Wind thresholds, or the wind speed at which snow/ice particles are lofted from the surface, are largely a function of the snowpack conditions. Relatively weak wind speeds ($3 - 8$ m s^{-1}) are necessary to loft snow particles that are loose from the surface (Mellor 1965; Li and Pomeroy 1997a). As the density of the snowpack increases, the wind speed threshold to initiate blowing snow increases (Mellor 1965). Li and Pomeroy (1997a) reported that the wind threshold for blowing dry snow conditions was ~7.7 m s^{-1} while blowing wet snow conditions required a wind threshold of ~9.9 m s^{-1}. Palm et al. (2011) stated that blowing snow conditions required wind speeds to be > 9 m s^{-1} and minimal-to-no blowing snow occurred at times where wind speeds fell below ~5 – 6 m s^{-1}. Wind speed thresholds for blowing snow are also influenced by the ambient temperature (Li and Pomeroy 1997a).

Temperature influences the amount of cohesion present in the snowpack and consequently the wind speed thresholds necessary for blowing snow formation. Li and Pomeroy (1997a) found a relationship between dry snow wind speed thresholds and the ambient temperature. Dry snow conditions were defined as those where temperatures remained < 0°C with no additional precipitation topping the snowpack. The relationship between dry snow wind speed thresholds and temperature showed that for temperatures between 0 °C and -25 °C, wind speed thresholds for

blowing snow increased as temperature increased and in conditions where temperatures are < -25

˚C, wind speed thresholds for blowing snow also increased with decreasing temperature.

Li and Pomeroy (1997a) found using statistical analysis that the relationship between the

ambient temperature and the wind speed threshold for blowing dry snow can be represented as

follows:

$$U_t a b T c T^2 \tag{1}$$

where U_t is the 10-m wind speed threshold applied (m s^{-1}), T is the temperature observed at a

height of 2-m (˚C), and $a = 9.43$ m s^{-1}, $b = 0.18$ m °C^{-1} s^{-1}, and $c = 0.0033$ m °C^{-2} s^{-1}.

Generally, as the temperature increases, the wind speed thresholds for blowing snow

increases due to the increased cohesion occurring, and as temperature drops to below -25 ˚C, wind

speed thresholds for blowing snow also increase (Li and Pomeroy 1997a). Wind speed thresholds

increase for temperature below -25 ˚C, due to the increased elastic and kinetic frictional forces.

1.3 Blowing Snow Impacts

Blowing snow within the Arctic impacts a diverse range of processes that influence global

climate change. Such processes include sea-ice deterioration and modification, aerosol and cloud

feedbacks, and way of life for local indigenous tribes. Each process is now discussed in detail.

1.3.1 Blowing Snow and Snow Depth

Blowing snow sublimation is a critical process for evolution of Arctic ice sheets and snow

depth as blowing snow sublimation alters the surface heat and mass budget. The redistribution of

snow particles increases the direct exposure of ice sheets to solar radiation (Déry and Tremblay

2004). A fresh thin layer of snow on the ice sheet acts to reflect most of the shortwave radiation

back into the atmosphere due to the high albedo of snow (Déry and Tremblay 2004). Thin snow layers also act to insulate the surface by trapping ocean heat in the lowest layers (Déry and Tremblay 2004). The removal of the thin snow layers increases the conductive heat flux from the ocean to the ice to the atmosphere (Landrum and Holland 2022). The heat loss results in cooler temperatures observed at the surface and an increased relative humidity throughout the boundary layer during the presence of blowing snow. The Arctic Coast snowfall experiences a 32% reduction due to blowing snow sublimation (Benson 1982). Chung et al. (2011) found that for the Surface Heat Budget of the Arctic Ocean (SHEBA), blowing snow sublimation reduced snow depth an average of 9-cm during the months of February through June (1997 – 1998).

Blowing snow and associated processes (e.g. sublimation) result in variable snow depth atop Arctic sea-ice. Spatial variability of snow depth and the processes that influence snow depth have become a key variable in the analysis of sea-ice evolution. The Intergovernmental Panel on Climate Change (IPCC) placed variable snow depth impacts on Artic sea-ice processes on a list of "Key Knowledge Gaps and Uncertainties" (Meredith et al. 2019). Current literature has focused on including variable snow depth on sea-ice throughout the winter season to evaluate the evolution of Arctic sea-ice thickness. Understanding this relationship between sea-ice thickness and snow depth presents challenges due to the lack of observational data on sea-ice thickness and sea-ice snow depth. Access to such data have increased, allowing studies to come out focusing on the inclusion of snow-depth variability. Mallett et al. (2021) performed a comparative study that looked at two Arctic sea-ice models. The first model, assembled from the Warren Climatology (hereafter "W99") (Warren et al. 1999), did not account for interannual variability of the snow present on sea-ice sheets. W99 is a 37-year climatology of snow depth and density measurements for Artic Ocean snow cover from Soviet drifting stations (Warren et al. 1990). The second model,

SnowModel-LG, derived snow depth from blowing snow sublimation, blowing snow redistribution, depth-hoar formation, and wind packing (Mallet et al. 2011 and Liston et al. 2020). The SnowModel-LG demonstrated that snow accumulations decreased throughout the Arctic study region from 2002 – 2018. W99 showed no statistical significance in the sea-ice thickness within the Chukchi Sea for the month of October, whereas the SnowModel-LG showed a statistically significant decline in sea-ice thickness for the month of October from 2002 - 2018. Further studies have demonstrated similar findings. Landrum and Holland (2022) found that atmosphere-only simulations that analyzed Arctic Amplification and sea-ice thickness in conditions with large concentrations of sea-ice, demonstrated decreasing conductive heat fluxes. However, when using models that account for changing sea-ice thickness and snow depth, the conductive heat fluxes increased. Thus, as demonstrated here, blowing snow plays an integral role in Arctic sea-ice processes.

1.3.2 Blowing Snow and Aerosols

The presence of aerosols influence the Arctic climate through modifications to the cloud microphysics and the scattering and absorption of solar radiation (Huang and Jaeglé 2017). Sea-salt aerosols (SSA) represent a large concentration of naturally occurring aerosols in the Arctic (Wang et al. 2019). Traditionally, SSAs were thought to be generated from breaking ocean waves, however, recent studies have hypothesized blowing snow as a source of SSAs. Huang and Jaeglé (2017) implemented a blowing snow emissions scheme within the GEO-Chem global chemical transport model to reproduce Arctic and Antarctic wintertime SSA concentrations. The inclusion of blowing snow within the model reduced open ocean model bias from 80 – 34% to 2 – 9% and accounted for daily variability better than simulations without the inclusion of blowing snow (Huang and Jaeglé 2017). Gong et al. (2023) found cloud condensation nuclei concentrations

increased up to ten times the mean amount due to SSAs generated from blowing snow sublimation. Furthermore, Choi et al. (2018) linked blowing snow generated SSAs to Arctic springtime bromine explosions resulting in the depletion of ozone.

Due to the lack of concrete blowing snow parameters, the inclusion of blowing snow within SSA simulations poses the potential of generating a positive bias in the concentrations of SSAs depending on the selected parameters used to determine blowing snow periods. Chen et al. (2022) conducted a study that analyzed Arctic springtime aerosols and atmospheric particles, focusing on the influence of blowing snow and leads on those concentrations. Blowing snow occurrences were determined using the methodology outlined in Li and Pomeroy (1997a) and Loeb and Kennedy (2021). This included detecting blowing snow based on wind speed and temperature. Blowing snow occurrences were compared to ceilometer data and it was found that blowing snow occurrences were overestimated from meteorological data alone (Chen et al. 2022). If blowing snow occurrences were overestimated, and such data were used to calculate SSAs from blowing snow sublimation, SSA values would also be overestimated.

1.3.3 Blowing Snow Impacts on Indigenous Tribes

The impacts of blowing snow and climate change have been observed and discussed among the local indigenous tribes. The Alaska Native Tribal Health Consortium reports climate change within the region, potential health and safety risks, and adaptive measures being taken by communities to account for the evolving climate (Brubaker et al. 2011). The depletion and early melting of sea-ice and near-zero visibility generated from blowing snow are concerns brought forth by the Native Village of Point Hope (Brubaker et al. 2011). Point Hope has implemented the use of rescue locator beacons. Beacons are loaned to individuals by the local fire department to enable tracking in case of an emergency (Brubaker et al. 2011). Willard Hunnicutt, a local Fire Chief,

stated "The storms have been very bad. Lots of wind and blowing snow. Hunters are using locator beacons that are tracked by Search and Rescue in Barrow. These result in rescues and saved lives" (Brubaker et al. 2011).

1.4 The Changing North Slope of Alaska Climate

The winter climatology of NSA is defined by high frequencies of strong wind events, falling precipitation, and blowing snow (Shulski and Wendler 2007). Atmospheric circulations and teleconnection phases drive synoptic-scale weather patterns and variability in the region (Cox et al. 2017; Cox et al. 2019). The most prevalent teleconnections in the region are the Pacific Decadal Oscillation (PDO) and the El Niño-Southern Oscillation (ENSO). Teleconnections influence the observed temperatures, accounting for some of the interannual temperature variability (Hartmann and Wendler 2005; McAfee 2014; Walsh and Brettschneider 2018). The strength and location of the Aleutian Low and the Beaufort Sea Anticyclone drive cold air advection (CAA) or warm air advection (WAA) within the Bering Strait, helping to determine the onset of spring snowmelt within northern Alaska (Cassano et al. 2016; Cox et al. 2017; Cox et al. 2019). The Aleutian Low is typically observed within the North Pacific off the Gulf of Alaska near the Aleutian Islands. WAA toward NSA occurs when southerly flow originates from the Gulf of Alaska and North Pacific Ocean. Cassano et al. (2011) found that Utqiaġvik positive temperature anomalies are associated with southerly flow or WAA; conversely, negative temperature anomalies or CAA are associated with northerly or easterly flow. When strong WAA does not occur and/or the Beaufort Sea Anticyclone blocks the advected warm air, the snowpack deteriorates slower (Cox et al. 2019). The relationship between the Aleutian Low strength and location and the Beaufort Sea Anticyclone has been formulated into a climate index for the determination of spring snowmelt by Cox et al. (2017) and has been investigated using an analog methodology by Walsh and Brettschneider

(2018). The Aleutian Low and the Beaufort Sea Anticyclone are prevailing climatological features driving climate within the Alaskan winter season (Shulski and Wendler 2007; Cassano et al. 2015; Cox et al. 2017; Cox et al. 2019).

NSA is a region strongly impacted by climate change and compounding Arctic Amplification (Cox et al. 2017). Evidence of an evolving climate within the region is seen in the melting of sea-ice, the earlier onset of spring snowmelt, the degradation of permafrost, etc. (Cassano et al. 2016; Cox et al. 2017). Within the Northern Hemisphere, Alaska has experienced an enhanced severity in climate change (Walsh and Brettschneider 2018). In comparison to the United States "lower-48", Alaska has experienced ~50% more warming (Ballinger et al. 2023). Ballinger et al. (2023) compromised a comprehensive climate trend analysis for Alaska (1957 to 2021) that revealed overall precipitation amounts within NSA have shown a significant increasing trend; conversely, spring and fall precipitation has shown decreasing trends. Sea-ice coverage within Alaska typically peaks in the month of March. Sea-ice coverage within March has steadily declined each decade shortening the continuous sea-ice coverage season and altering the surface radiation budget (Cox et al. 2017; Ballinger et al. 2023). The sea-ice melting season has increased by ~3 weeks due to the earlier onset of melting and the later date of continuous freezing (Ballinger et al. 2023). Arctic Amplification is enhanced by Arctic sea-ice coverage reductions and the increased exposure of open ocean, generating a positive feedback loop. Open ocean has a significantly lower albedo than sea-ice and snow, resulting in the increased absorption of radiation at the surface. Vertical temperature structures within the polar regions under the influence of Arctic Amplification are projected to display substantial warming confined to the surface that decreases with height (Kay et al. 2012; Gervais et al. 2016). The full impacts of climate change on the climatology and teleconnections observed within NSA is not yet fully understood, however, it is

apparent the climate is evolving. Blowing snow directly influences the Arctic climate and is, therefore, critical to research to help understand how and what the climatology of NSA will look like in the coming decades.

PURPOSE OF THIS STUDY

Blowing snow in the Arctic influences the surface heat/energy budget (Landrum and Holland 2022), surface mass budget (Chung et al. 2011), hydrological cycle (Benson 1982), indigenous people safety (Brubaker 2011), and is a major source of uncertainty in sea-ice evolution (Meredith et al. 2019). Currently, most models do not include blowing snow as there has not been widespread validation of blowing snow parameterizations. Fortunately, NSA contains instrumentation from 31 October 2003 to present day that offers an unprecedented opportunity to analyze and detect blowing snow and understand how blowing snow may be changing in time. The purpose of this study is to identify periods and frequency of blowing snow at the ARM NSA site and identify the local and synoptic forcing mechanisms for this process. Blowing snow is identified using in-situ instrumentation located at NSA including a laser disdrometer, digital video disdrometer, and various surface-based sensors. Blowing snow is segregated as a function of various meteorological variables and observed particle counts. Such data will allow for the verification of meteorological parameters used to classify blowing snow conditions within models. Furthermore, this allows for the understanding of the strengths and weaknesses of ARM instrumentation in the observation and detection of blowing snow events.

The classification of blowing snow on the synoptic scale is accomplished using Self-Organizing Maps (SOMs). SOMs were initialized and trained using ERA5 Reanalysis mean sea-level pressure (MSLP) data. This allows for an even longer record of historical blowing snow events prior to the existence of in-situ instrumentation. The meteorological thresholds found prior

can be applied to the SOM data to calculate the expected blowing snow frequency for historical periods. Collectively, this allows for trends in blowing snow to be identified. Furthermore, this enables future researchers to develop and test hypotheses and new parameters regarding blowing snow impacts in an evolving climate.

IMPACTS AND LIMITATIONS OF THIS STUDY

Determining the weather patterns associated with blowing snow will allow for thorough validation of other modeling efforts, and eventually, this will lead to ample knowledge to confidently incorporate these schemes into weather and climate models. The incorporation of blowing snow into weather and climate models will allow for better forecasting of reduced visibility conditions and consequently blizzard forecasting, improving overall human safety. Furthermore, the ability of a SOM to classify specific weather patterns conducive to blowing snow will be determined. This study heavily investigates the use of ARM NSA in-situ instrumentation for the detection of blowing snow. Thus, this study will highlight the strengths and weaknesses of in-situ instrumentation for blowing snow detection. Highlighting the weaknesses in such instrumentation will allow future scientists to improve such weaknesses. Improved instrumentation will benefit a wide range of individuals within the weather and climate community. As mentioned in Chapter 1, the Arctic climate is undergoing a large shift due to Arctic Amplification and a warming planet. Current literature suggests that snow redistribution and the removal of thin snow layers by processes such as blowing snow and resulting sublimation play a critical role in the evolution of Arctic sea-ice thickness. The enhanced understanding of blowing snow conditions, specifically in the Arctic, can potentially allow for blowing snow and sublimation processes to be more readily represented in current sea-ice models.
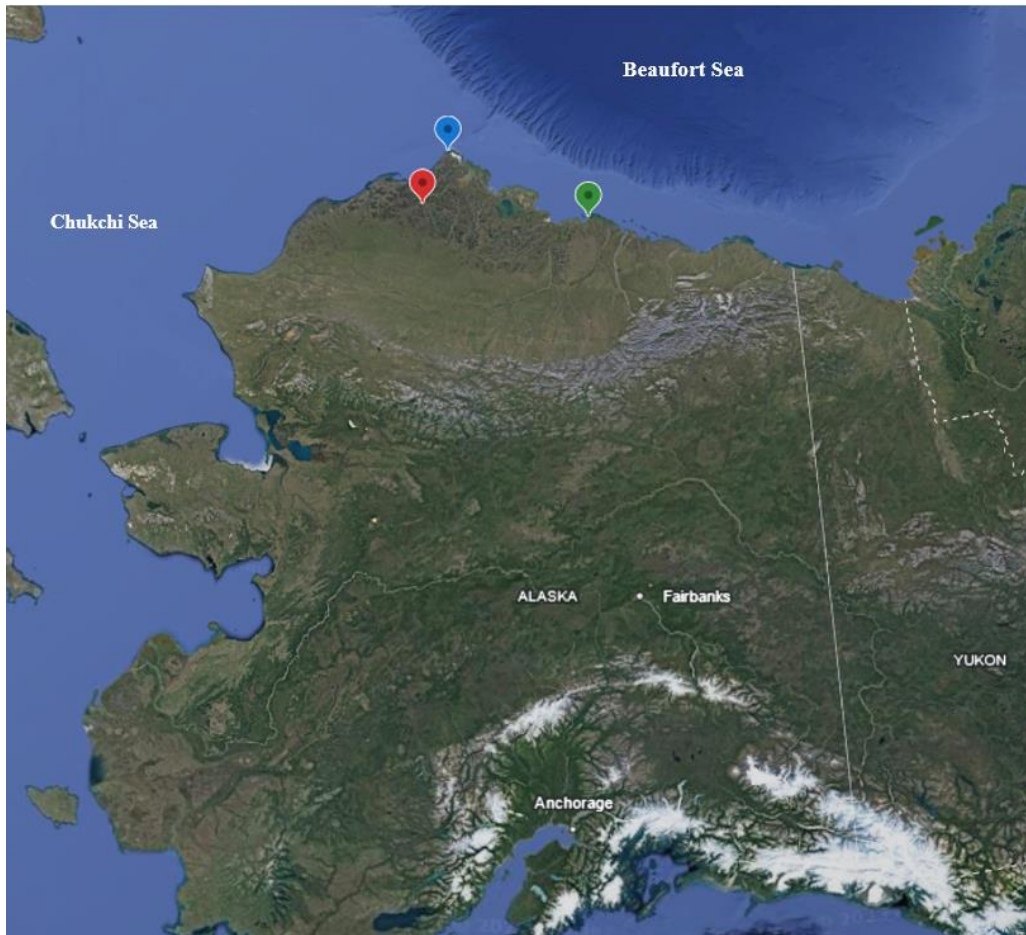
Figure 1. Location of the ARM NSA sites. The C1 main site is marked by the blue pin. The Atqasuk facility (no longer in operation) is marked by the red pin. The ARM Mobile Facility 3, AMF3, is located at Oliktok Point and marked by the green pin.

CHAPTER 2

DATA AND METHODS

This chapter begins with a description of instrumentation used in this study. Background material for each instrument is provided along with an explanation of the data streams and data processing performed. The following instruments are discussed: Surface Meteorological Instrumentation (MET), the Precipitation Imaging Package (PIP), and the Laser Precipitation Monitor (LPM). The methods used to assess the ability of the LPM and PIP to detect blowing snow periods are then described. This section is then followed by a discussion of datasets and tools used to classify synoptic patterns including the ERA5 Reanalysis and Self Organizing Maps (SOMs). The chapter concludes with the methods used to calculate the historical frequency of blowing snow.

2.1 SURFACE INSTRUMENTATION

2.1.1 Surface Meteorological Instrumentation

Standard meteorological variables are provided by the MET data stream at NSA. MET data reports 1-minute average measurements for pressure, precipitation, relative humidity, temperature, and horizontal wind (Ritsche et al. 2011). Measurements are taken by a variety of Vaisala in situ instruments on 10 m towers (Ritsche et al. 2011). MET has used two different sensors to report present weather data and visibility data. Prior to 2010, the Present Weather Sensor (PWS) was used. In 2010, NSA transitioned to the Present Weather Detector (PWD). The PWS and PWD

measurements are identical, meaning that PWS and PWD variables were merged with PWS data making up 2003 – the end of 2009 data, and PWD data making up 2010 – 2022 data. Wind speed is reported at a height of 10 m while temperature and relative humidity (RH) are measured at a height of 2 m. These measurements are made with a Vaisala HMT330 RH and temperature transmitter (Andreas et al. 2002; Gong et al. 2023). Reported RH is made with respect to water (Gong et al. 2023). As this study is confined to the Arctic winter months, RH was calculated with respect to ice using the method of Andreas et al. (2002). For

- 40˚C $\leq$ T$_a$ $\leq$ 0˚C (Buck 1989) the equation is:

$$e_{sat,w(T_a)} = (1.0007 + 3.46 \times 10^{-6})6.1121\exp\left(\frac{17.966T_a}{247.15 + T_a}\right), \tag{1}$$

while for - 50˚C $\leq$ T$_a$ $\leq$ 0˚C:

$$e_{sat,i(T_a)} = (1.0003 + 4.18 \times 10^{-6})6.1115\exp\left(\frac{25.452T_a}{272.55 + T_a}\right), \tag{2}$$

where, T$_a$ is the ambient temperature (˚C), P is the pressure in hPa, e$_{sat,w}$ is the saturation vapor pressure over water (hPa), and e$_{sat,i}$ is the saturation vapor pressure over ice (hPa).

NSA MET data (DOI: 10.5439/1786358) are available from 31 October 2003 to present day. Data were retrieved from the ARM Data Discovery (https://adc.arm.gov/discovery/#/) between 2003-2022. October through April were selected for analysis as prior work done by Liston and Sturm (2002) focused on 1 September through 30 April. September was not included due to the lack of time blowing snow conditions were observed as defined by the AMS and Mellor (1965). Wind speeds must be $\geq$ 3 m s^{-1}, 2 m air temperatures $\leq$ 0 ˚C, and visibility $\leq$ 11-km. These

conditions were only met ~2.7 % of the time in September. Provided the higher frequencies of blowing snow in other months, September was omitted to prevent potentially skewing other results of this study such as the SOM classification of synoptic-scale patterns.

The MET data stream was quality controlled according to the Data Quality Reports (DQRs), provided by the ARM data archive. Individual write-ups for flagged data were investigated to understand how they related to variables of interest: 2 m temperature, 2 m pressure, 2 m RH, 10 m wind speed, precipitation rate, visibility, and cumulative snowfall. Embedded DQR flags were referenced for each variable to ensure bad data were masked.

The MET data were resampled from 1-minute averages to 5-minute averages. MET data were also obtained from the ARM Mobile Facility located in Oliktok Point between 30 April 2017 – 31 December 2021. All variables mentioned above were selected for Oliktok Point and quality controlled following the same procedures. Oliktok Point MET data were included to generate a particle size distribution (PSD) plot segregated by wind speed for the Oliktok Point LPM. The methodology used to generate the PSD plots are discussed in Section *2.2.1*.

2.1.2 Precipitation Imaging Package

The PIP is a digital video disdrometer developed by Larry Bliven of the National Aeronautics and Space Administration (NASA). The PIP has two main components: 1) a high-speed camera that captures 380 frames per second and 2) a halogen lamp located 2 m away to allow for hydrometeor backlight (Pettersen et al. 2021; Helms et al. 2022). Hydrometeors are captured in an open sampling volume of 64 mm × 48 mm between the halogen lamp and the backlight with a resolution of 0.1 mm × 0.1 mm (Pettersen et al. 2021; Helms et al. 2022). Images undergo processing that determines individual particle properties, including PSDs, liquid-water-

equivalent (LWE) snowfall rate, and bulk particle density (Kulie et al. 2021; Pettersen et al. 2021). The PIP has 131 unique particle diameter bins ranging from ≤ 0.1 mm to 26 mm.

PIP data have been used in a diverse range of studies focusing on wintertime precipitation. Pettersen et al. (2020) compared microphysical properties directly measured or derived from the PIP to surface observations from the National Weather Service (NWS) forecast office located in Marquette, Michigan (MQT). Accumulations of LWE snowfall derived from the PIP for high and low snow-liquid-ratios (SLRs) matched the measurements reported by the office. The PIP has been shown to accurately represent precipitation phase changes. Pettersen et al. (2021) compared rain-to-snow and snow-to-rain onsets and end times of 13 events between January 2017 – January 2020 in Marquette, MI, with a denoted phase change reported by the NWS MQT office. PIP onset times of snow-to-rain events were within 15-minutes of the NWS MQT times and end times were within 20-minutes of each other (Pettersen et al. 2021). PIP onset times of rain-to-snow events were within 15-minutes of each other, and end times were within 25-minutes of each other (Pettersen et al. 2021). Kulie et al. (2021) conducted a multi-sensor observational study to analyze the various snowfall regimes within the northern Great Lakes. The sensors used included a Micro Rain Radar (MRR), PIP, and ground-based surface observations. The PIP and MRR effectively captured the microphysical characteristics of shallow lake-effect, lake-orographic, and transition snowfall events. Furthermore, the PIP has been used in comparative studies looking at the performance of in situ snowfall sensors (Maahn et al. 2023). Minimal research has focused on the performance of the PIP in cases of blowing snow conditions.

NSA contains one PIP located at the Central Facility. The PIP stand is 7 ft 10 in tall and with the additional height added by the case and the video camera itself, the PIP's approximate height is ~8 ft, or 2.44 m, off the snow-free surface. PIP data are available from 23 October 2018

to present day (DOI: 10.5439/1489525). PIP data for this study were taken from 23 October 2018 to December 2021. Data were quality controlled with DQRs supplied by the ARM data archive. PIP PSD data were resampled from 1-minute data to 5-minute summed bins. Smaller-sized particles were investigated due to the typical blowing snow size distribution (e.g., particle diameters ≤ 1.125 mm).

2.1.3. Laser Precipitation Monitor

The Laser Precipitation Monitor (LPM) is a type of optical laser disdrometer designed and engineered by the German company Adolf Thies GmbH & Co KG. The LPM has a 46 cm^2 horizontal sampling volume for hydrometeors. As hydrometeors enter the sampling volume, particles pass through an infrared laser beam. The signal is measured by a photodiode across from the laser and processed to characterize particle diameter, precipitation type, and fall velocity (Meshesha et al. 2016; Pckering et al. 2019). Precipitation intensity and type is derived using optical principles and reported by the LPM (Fehlmann et al. 2020). The LPM has 22 unique particle bins ranging from ≤ 1.125 mm to > 8 mm.

The LPM has mainly been used for mixed-phased precipitation and hydrology-based studies. Meshesha et al. (2016) used the LPM to determine drop-size distributions for simulated rainfall and used those data to develop a relationship between rainfall kinetic energy and intensity to investigate soil erosion due to rain splash. Pickering et al. (2019) constructed a network of Thies LPMs throughout the United Kingdom (UK) to monitor extreme precipitation events and verify the ability of the LPM to classify phase-transitions. Pickering et al. (2019) investigated three case studies that covered rain-snow, intense convective rainfall, and graupel shower events. The LPM properly diagnosed the onset of rain-snow transitions observed by the varying particle diameters and fall velocities, during the 23 February 2017 winter storm. Fehlmann et al. (2020) determined

instrument bias for the LPM by measuring various precipitation events using two Thies LPMs located in Innereriz, Switzerland. Over the two-year study period, Fehlmann et al. (2020) found that the LPM systematically underestimated snowfall for particles > 0.75 mm in diameter. Fargey et al. (2014) used LPM PSDs and particle concentration data to help characterize features of a unique snowfall event occurring in Iqaluit, Nunavut. The LPM supplemented weighing gauge measurements (Fehlmann et al. 2020). Gultepe et al. (2017) denoted the importance of using optical disdrometers such as the LPM to optimize snowfall measurements as traditional weighing gauges are subject to large degrees of uncertainty and to aid in general Arctic related measurements. Like the PIP, there is little information about instrument performance for blowing snow. Loeb and Kennedy (2021), however, documented erroneous PSDs with the OTT Hydrometer Parsivel[2] which is a competing laser disdrometer.

Three NSA LPM instruments were used including sensors at the main site, co-located E10, and Oliktok Point. The fourth LPM available at NSA was excluded as it became operational after this research was started. Each LPM stands at a height of 2 m above the snow-free surface. LPM data for the main site are available from 27 April 2017 to the present day (DOI: 10.5439/1390571). LPM data for the E10 location is available from 30 September 2018 to the present day (DOI: 10.5439/1390571). LPM data from Oliktok Point is available from 30 April 2017 to 14 June 2021 (DOI: 10.5439/1390571). Data from each LPM was analyzed between October 2018 to December 2021 for the cold season months of October to April. LPM particle spectrum data were summed along the dimension of particle fall velocity and then resampled from 1-minute data to 5-minute summed bins. Smaller-sized particles were investigated due to the typical blowing snow size distribution (e.g., particle diameters ≤ 1.125 mm). All LPM data were QC'ed in the same manner as the PIP.

2.2. METHODS

To determine the meteorological variables associated with blowing snow, conditions must be identified and then analyzed as a function meteorological regime. Ground truth is considered as microphysical imager data, but the LPM and PIP must be compared to determine the strengths and limitations of each instrument to detect blowing snow. Contingency tables were created to determine the performance of various meteorological thresholds in forecasting blowing snow conditions to ultimately pick a set of parameters that optimized the selection of blowing snow conditions from meteorological data alone.

2.2.1. LPM and PIP Comparison

Mean logarithmic PSDs were created for the NSA main site (C1) PIP and C1, E10, and Oliktok Point LPMs and segregated by MET 10 m wind speed as with the investigation of the Parsivel[2] in Loeb and Kennedy (2021). PSDs for all instruments were restricted to ≤ 8 mm for particle counts > 0. The large particle diameter restriction was selected to encompass the full PSD. Times that reported no particles, i.e., clear sky conditions, were omitted as the point of the analysis was to focus on performance during falling and blowing snow conditions. A 3 m s^{-1} minimum 10 m wind speed threshold was also applied as a lower limit for blowing snow (Mellor 1965; Li and Pomeroy 1997a). To avoid sampling related bias, data were binned into increments of 2 m s^{-1} for wind speed and 5 ˚C for temperature. Several variations of the 2-D histograms were generated. The first series included particle counts > 0 for particle diameters ≤ 1.125 mm to emphasize the occurrence of blowing snow. Remaining experiments focused on changing the minimum particle count threshold to understand the sensitivity to meteorological variables. 2-D histograms were created for minimum 5-minute particle count thresholds of 200, 300, 500, and 1000.

2.2.2 Assessment of Meteorological Conditions

Forecasters' 2×2 contingency tables were used to derive the Critical Skill Index (CSI), False Alarm Ration (FAR), Probability of Detection (POD), Heidke Skill Score (HSS), and frequency of various meteorological thresholds with respect to blowing snow. A sample contingency table modeled off Gold et al. (2020) and Schaefer (1990) is displayed in Fig. 2 and is referenced as an example for calculations of CSI, FAR, POD, and HSS.

In this study, particle imagers reaching a threshold particle count represent ground truth while meteorological thresholds (e.g., wind speed exceeding a value) represent the forecast. A positive hit means both conditions are met. The overall frequency is the ratio of times blowing snow occurred given a set of meteorological thresholds to the number of times the meteorological threshold occurred. Frequency values < 1 represent under-forecasting of blowing snow conditions, whereas frequency values > 1 represent over-forecasting. A frequency value = 1 represents perfect forecasting of blowing snow given the meteorological thresholds.

The CSI (Fig. 2) is defined as the ratio of correctly forecasted events to the total number of forecasted events (Schaefer 1990; Wilks 2019). CSI values range from 0 to 1, with 1 representing a perfect forecast and is given by:

$$\boldsymbol{CSI} = \frac{a}{a+b+c}.$$

(3)

Schaefer (1990) defines FAR (Fig. 2) as "the ratio of unsuccessful positive forecasts to the total number of positive forecasts." FAR values range from 0 to 1, with 0 representing no false positives in the forecast and is given by (Wilks 2019):

$$\boldsymbol{FAR} = \frac{b}{a+b}.$$

(4)

The POD (Fig. 2) is the ratio of successfully forecasted events to the total number of events (Schaefer 1990). POD values range from 0 to 1, with 1 representing all positive forecasted events being properly forecasted and is given by (Wilks 2019).

$$POD = \frac{a}{a+c}. \qquad (5)$$

The HSS (Fig. 2) is a score used as verification for categorical forecasting (Barnston 1992). The HSS is derived by scaling the proportion of correct forecasts by the number of correct forecasts expected by chance. A perfect forecast will have a HSS of 1 (Barnston 1992). Equations 6 and 7 adapted from Barnston (1992) were used to calculate the HSS and are given by:

$$(6)$$
$$\textbf{Expected Correct } (EC) = \left(\frac{1}{Total\ Forecasts}\right) * [((a + c) * (a + b)) + ((d + c) * (d + b))],$$

$$HSS = \frac{((a+d)-EC)}{Total\ Forecasts-EC}. \qquad (7)$$

The maximum visibility and minimum wind speed thresholds determined for each method were applied to the MET data stream. The frequency of blowing snow detected by the particle imager using the definition of blowing snow was calculated for each particle count threshold and denoted as the "Particle Imager Frequency." The frequency of blowing snow detected by just the meteorological thresholds was calculated and denoted as "MET". The two values were compared to see how well the MET method was at detecting blowing snow compared to particle imagers. In addition to the frequency comparisons, regression analysis was done. R-squared values were calculated for each MET method. The "best" set of meteorological thresholds possessed a balance of a high HSS and R-squared values and MET frequencies without substantial bias compared to particle imagers.

2.3. SELF-ORGANIZING MAPS AND REANALYSIS DATA

Self-Organizing Maps (SOMs) (Kohonen 1990) were made to objectively classify the synoptic-scale patterns associated with blowing snow events. ERA5 Reanalysis data were used to initialize, train, and generate the SOMs. A description of the ERA5 Reanalysis will be provided followed by a brief background on SOMs, and the methodology used to make the SOMs. This section concludes with a description of how SOMs are used to derive a historical record of blowing snow at NSA.

2.3.1 ERA5 Reanalysis

The European Centre for Medium-Range Weather Forecasts (ECMWF) ERA5 Reanalysis is a fifth-generation global climate and weather reanalysis product (Hersbach et al. 2020). ERA5 combines model data output and observational data to create a globally gridded representation of the Earth's surface and atmosphere. ERA5 was engineered to replace its predecessor, ERA-Interim (Hersbach et al. 2020). ERA5 provides hourly data with 31 km horizontal grid spacing and 137 vertical levels from the surface to a height of 80 km (Albergel 2018). ERA5 single-level data are available from 1959 to present day (Albergel 2018).

ERA5 sea-level pressure, 10 m zonal horizontal wind component, and 10 m meridional horizontal wind component were used in this study to generate SOMs for NSA. ERA5 data from 1 January 1979 to 28 February 2022 for the winter months of October – April were used. ERA5 data were re-gridded to the CESM LENS2 grid decreasing the horizontal grid spacing from 0.25˚ x 0.25˚to 1˚ x 1˚ and thus, decreasing the computational time. These data were supplied by Taylor Dolan (University of North Dakota); the original code was written and processed by Dr. Maria Molina (University of Maryland). The ERA5 re-gridded data were spatial interpolated to a grid centered at the NSA site at 71.99˚ N and 156.36˚ W (Fig. 3). The resulting grid was 20˚ x 60˚ with

1˚ latitude and longitude spacing to ensure synoptic-scale features would be preserved while also decreasing the computing time to create the SOMs.

2.3.2 SOM background

SOMs are a form of unsupervised learning that uses a competitive neural network to cluster alike data. While similar to K-means clustering, SOM classes (or nodes) are related to one another through a neighborhood function (Sheridan and Lee 2011). SOM clustering techniques have been found to be more representative of datasets in comparison to traditional clustering methods that organize data based on a set distribution or model type. Michaelides and Tymvios (2009) analyzed long-term rainfall variability in Cyprus using traditional clustering methods and SOMs. They determined that the SOM output classified synoptic-scale patterns better than traditional clustering methods. Statistical-based clustering methods tend to map a few prevailing patterns and the remainder represent outliers within the dataset (Michaelides and Tymvios 2009). SOMs produced patterns that represented the data as a whole and transitions between patterns were more gradual. SOMs can represent non-linear characteristics in data and treat datasets as a continuum with is more representative of atmospheric patterns (Cassano et al. 2006; Kennedy et al. 2016, 2019).

2.3.3 SOM methods

SOMs were created to capture the prevailing wintertime synoptic-scale atmospheric patterns at NSA. SOMs were generated using the Python-based MiniSom package (https://github.com/JustGlowing/minisom). Slight discrepancies exist in the terminology of MiniSom vs. SOM literature. The neighborhood radius parameter, for example, is denoted as "sigma".

Two types of SOMs were generated using one-step training. The first iteration of SOMs were trained using the spatially averaged 20˚ x 60˚ (every 1˚ longitude; every 1˚ latitude) ERA5 Reanalysis mean sea-level pressure (MSLP) data re-gridded to the CESM LENS2 grid. Prior to being input into the SOM, data were resampled every 6-hours. The traditional boreal winter was extended (October – April) to account for the elongated winter season observed in the North Slope region (Liston and Strum 2002). Data were reshaped into a 2-D array of shape (nhours, nlat*nlon), with nhours representing each 6-hour MSLP value and the nlat*nlon representing the stacked latitude and longitude fields. MSLP means were removed from each sample to calculate MSLP anomalies. Data were normalized by determining the maximum and minimum MSLP anomalies for the dataset, subtracting the minimum from the maximum, and dividing 100 by that value to calculate a normalization factor. The normalization factor was multiplied to the entire 2-D array and input into the SOM.

The second iteration of SOMs were trained using the spatially averaged 20˚ x 60˚ (every 1˚ longitude; every 1˚ latitude) ERA5 Reanalysis MSLP, 10 m zonal horizontal wind component, and 10 m meridional horizontal wind component, re-gridded to the CESM LENS2 grid. Wind was included in the generation of SOMs due to the critical relationship between wind speed thresholds and blowing snow processes (Li and Pomeroy 1997; Mellor 1965; Palm et al. 2011). The 10 m zonal and meridional components of the wind were normalized using the same method as with the MSLP field. Several variations of training were used to create the SOMs.

A two-step training process, following Kennedy et al. (2019), Kim et al. (2022), and Lennard and Hegerl (2015), was initially used. This process involved using MiniSom in two consecutive phases with different values for the learning rate and neighborhood properties. SOMs of size 8 × 7, 10 × 7, 7 × 5, and 5 × 4 were created. For all SOM trials made using the two-step

training process, the neighborhood function was set to "Bubble" and the topology of the SOM was rectangular to model the work of Kennedy et al. (2019). The sigma for the first phase of training, $sigma_1$, was (y-1), i.e., if the SOM was a 10×7, then $sigma_1$ was 6 (7-1). For the second phase of training, the sigma, $sigma_2$, was reduced to < $sigma_1$. Generally, $sigma_2$ was set to 1, however, this value changed for several SOM iterations to understand the influence of the reduced $sigma_2$ and see if there was potential improvement in the output with varying $sigma_2$ values. The learning rate was largely manipulated between SOM trials. The learning rate for phase #1 (denoted herein as LR_1) was always > the learning rate for phase #2 (denoted herein as LR_2). The reduction in the learning rates between phases ranged from 0.02 – 0.04. The two-step training method was only performed using MSLP data, as this method was not the primary SOM training technique. All remaining training iterations followed a one-step process.

One-step training using MSLP data only involved the changing of each individual SOM parameter, the number of nodes, and the shape of the SOM grid per SOM trial. SOMs of size 10×7, 9×6, 8×5, 4×2, and 5×4 were generated with sigma values set to one minus the number of rows (y-1) and learning rate values ranging from 0.05 to 0.0005. Similar to the two-step training, the neighborhood function was set to "Bubble" for all iterations to model the work of Kennedy et al. (2019). A decay function was applied in the one-step training. Asymptotic decay was used for all SOM iterations. Weights were trained 100,000 iterations to achieve the lowest quantization error (q-error). For each set of parameters, 10 total SOMs were created. One-step training using MSLP and wind data followed the same procedures for the MSLP only SOMs; however, SOMs of size 9×7 and 8×5 were only used. No larger and/or smaller SOMs were created for the MSLP and wind SOMs. This was done as increasing the size of the SOM reduced the number of samples

in each node and when using multiple variables as input into the SOM, the SOM must be larger to account for the increased complexity.

To determine a 'winning' SOM, three different plots were created to visualize the output. Frequency plots were made to visualize the spatial distribution of nodes. A "good" frequency plot displayed evenly distributed data among nodes, whereas a "bad" frequency plot showed data concentrated within a few nodes (Fig. 4). Sammon plots were created to determine the level of distortion of the SOM (Fig. 5). Sammon mapping is the process of comparing individual nodes to its' adjacent neighbors (Cassano et al. 2006). As mentioned prior, SOM clustering nodes are not treated independently, meaning that winning nodes influence and modify the surrounding nodes. This process is governed by the neighborhood radius (Sheridan and Lee 2011). Due to this, nodes adjacent to one another should resemble similar patterns with small Euclidean distances. Sammon plots represent each node as a dot and the Euclidean distance between neighboring nodes as a solid black line connecting the nodes. The most accurate Sammon plot is one in which the average Euclidean distance is minimized (Lennard and Hegerl 2015). Sammon plots with large Euclidean distances display heavy distortion and twisting (Lennard and Hegerl 2015). For SOMs trained exclusively with MSLP data, MSLP anomalies were plotted by node to display the SOM derived patterns. For SOMs trained using MSLP and wind data, MSLP anomalies and wind barbs were plotted according to node to display the SOM derived patterns. For the purposes of this study, a "winning SOM" is one in which 1) spatial distribution of node frequency is present with 2) connectiveness between nodes with minimal distortion, and 3) high-pressure systems and low-pressure systems are plotted on opposing sides of the SOM matrix with similar patterns being plotted adjacent to one another.

2.3.4 Identifying the historic frequency of blowing snow

To determine the historic frequency of blowing snow at NSA, a climatological frequency was derived from the contingency table analysis mentioned in Section *2.2.2* and applied to the SOM. In this study, the climatological frequency represented the frequency of blowing snow per SOM node. To calculate this, the meteorological thresholds found in Section *2.2.2* were applied to the entire MET data stream to achieve a time series of blowing snow occurrence. Any months within the MET data stream that contained > 75% missing times were omitted from the analysis to prevent potential bias in the frequencies. Smaller missing data thresholds (e.g. > 50%), were applied. Table 4 displays the monthly percentages of missing 5-minute intervals. The winning SOM was subset to match the times MET data were available (e.g. October 2003 – December 2021). The blowing snow time series was separated by SOM nodes. For each node, the climatological frequency of blowing snow was calculated as the number of times blowing snow occurred divided by the total number of times the node occurred. Using the climatological frequency, a SOM-only derived blowing snow frequency was calculated for the subset SOM data. For each time within the SOM subset, the associated node was found. Using the node information, the expected blowing snow frequency for that time was found by looking up the node within the climatological frequency. The expected blowing snow frequency was calculated for each timestamp. To derive the SOM-only blowing snow frequency per node, the expected blowing snow frequencies for each node were summed and divided by the total amount of times within the node. This method will be referred to as "SOM."

Blowing snow frequencies were calculated for each year and individual months from October 2003 – December 2021 using the MET and SOM methods. The MET and SOM derived frequencies were plotted as a scatter plot and the corresponding R-squared value was calculated.

The R-squared value was calculated to prove that the SOM could reasonably calculate blowing

snow frequencies in the absence of available MET data.

	Observed		Totals
	Yes	No	
Forecast Yes	a	b	a + b
Forecast No	c	d	c + d
	a + b	b + d	a+b+c+d = n

Figure 2: A forecaster's 2 × 2 contingency table adapted from Wilks (2019).
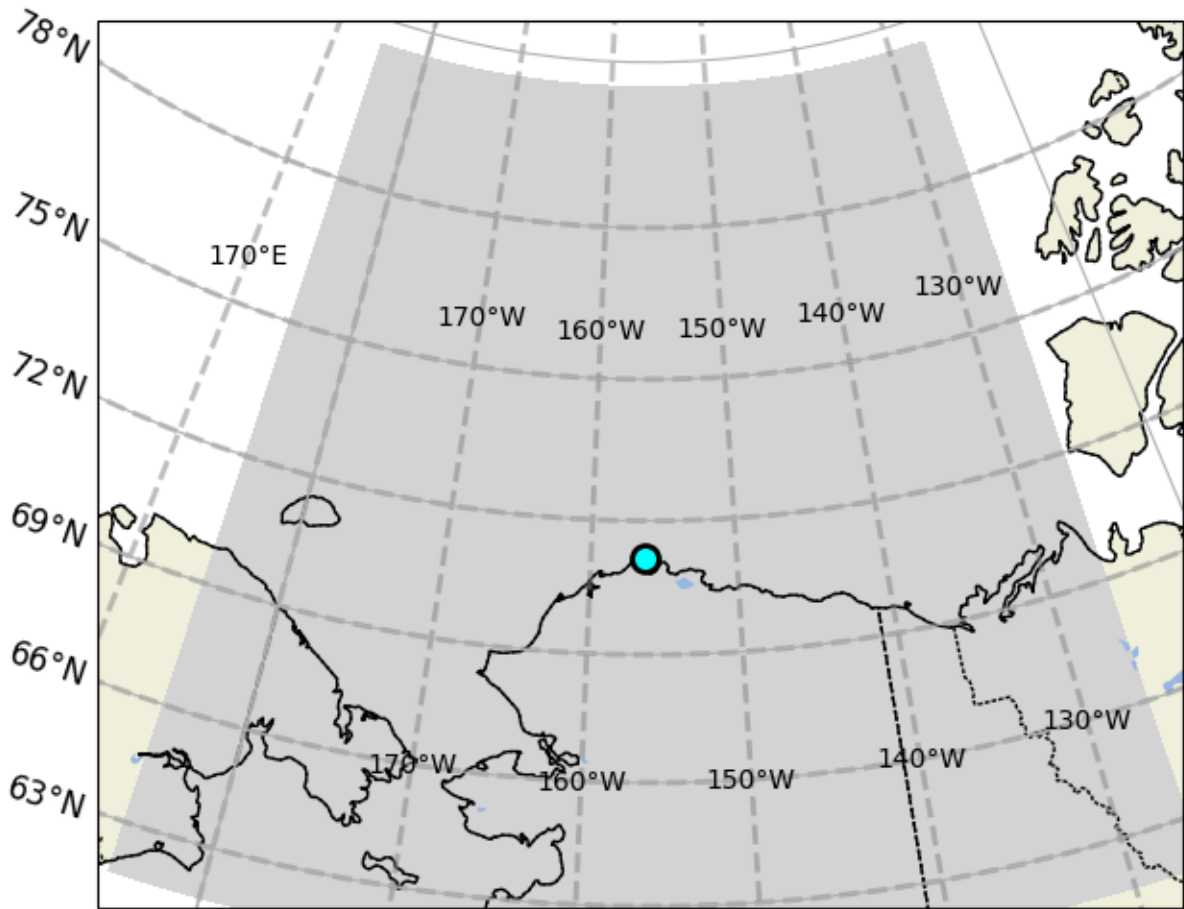
Figure 3: Domain used for this study. The grey area represents the geographic region ERA5 data were obtained for. NSA is denoted by the cyan dot.
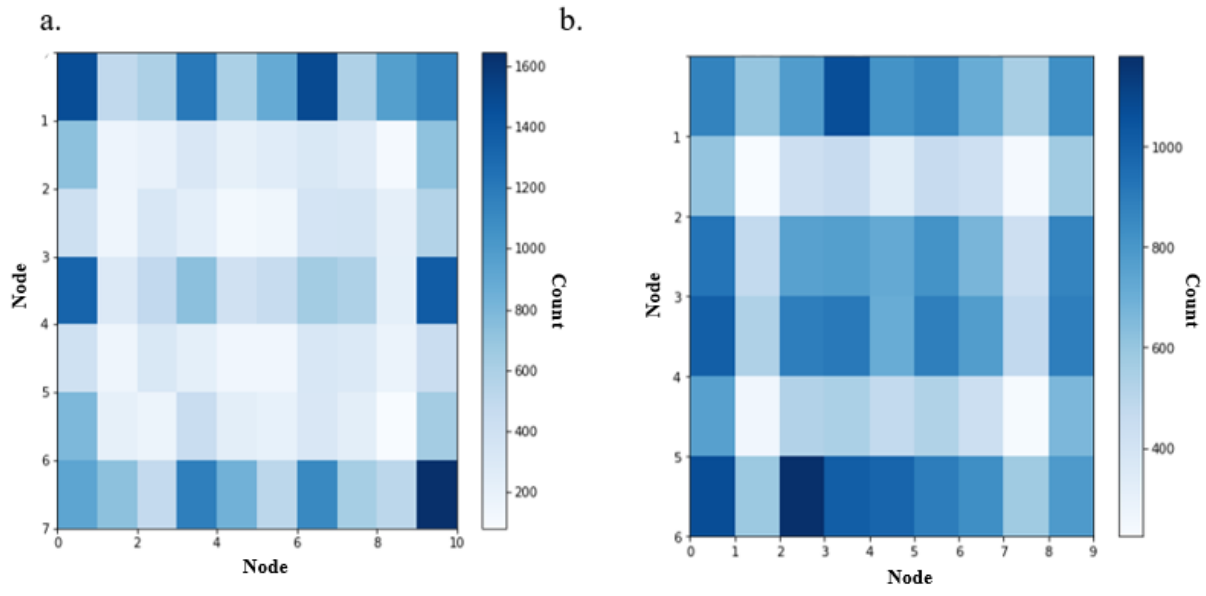
Figure 4: Sample SOM frequency plots for a (a) "bad" and (b) "good" SOM.
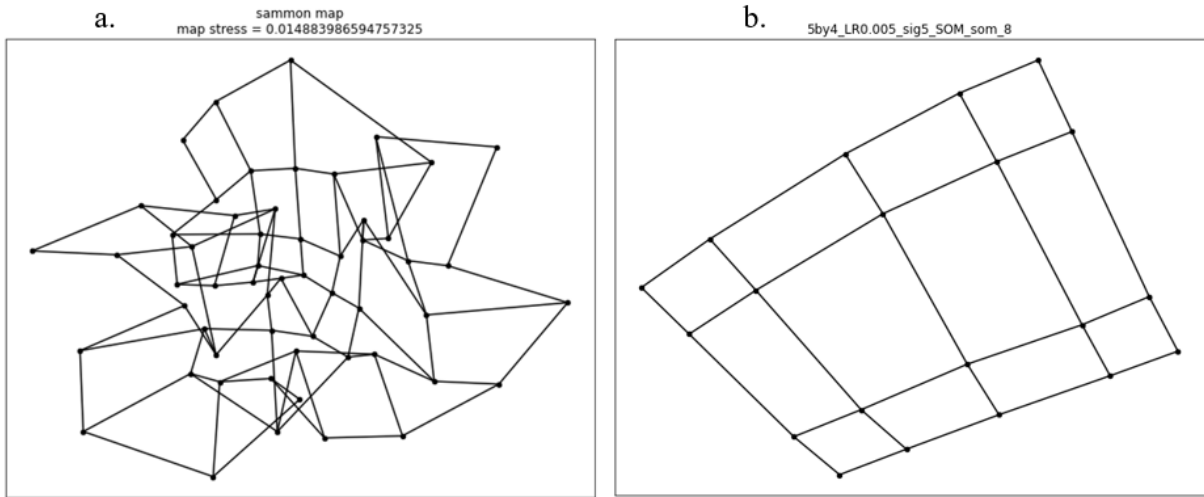
Figure 5: Sample SOM Sammon frequency plots for a (a) "bad" and (b) "good" SOM.

Table 1: Two-step SOM training parameter experiments. This is a sub-sample of parameters used for the two-step training method.

SOM Size	Sigma$_1$	Sigma$_2$	LR$_1$	LR$_2$	Neighborhood Function
8×7	6	1	1	0.05	Bubble
10×7	6	1	1	0.005	Bubble
7×5	4	1	1	0.04	Bubble
5×4	3	1	0.5	0.05	Bubble

Table 2: One-step MSLP only SOM training experiments.

SOM Size	Sigma	LR	Decay Function	Neighborhood Function
5 × 4	3	0.005	Asymptotic	Bubble
8 ×5	4	0.05	Asymptotic	Bubble
4 ×2	1	0.005	Asymptotic	Bubble
4 ×3	2	0.005	Asymptotic	Bubble
8 ×5	4	0.0005	Asymptotic	Bubble
8 ×5	4	0.005	Asymptotic	Bubble
9 ×7	6	0.0005	Asymptotic	Bubble
9 ×5	4	0.0005	Asymptotic	Bubble
4 ×3	2	0.0005	Asymptotic	Bubble

Table 3: Winning one-step MSLP and wind SOM training parameters.

SOM Size	Sigma	LR	Decay Function	Neighborhood Function
8 ×5	4	0.0005	Asymptotic	Bubble
9 ×7	6	0.0005	Asymptotic	Bubble

Table 4: Monthly percentage of missing 5-minute MET data. A value of 100% represents an entire month of missing data.

Year	Jan.	Feb.	March	April	Oct.	Nov.	Dec.
2003	100	100	100	100	96.8	2.2	0.7
2004	0.7	6.1	5.5	0.1	40.0	7.1	60.0
2005	100	100	100	86.0	1.1	7.6	0.8
2006	56.5	8.3	3.0	0.0	16.6	10.2	3.7
2007	16.1	1.3	3.2	70.6	29.7	4.9	4.8
2008	20.6	0.1	5.2	0.6	1.8	100	57.9
2009	2.0	18.5	16.7	9.8	6.7	3.3	0.1
2010	100	100	100	100	20.4	4.1	29.4
2011	15.6	0.5	1.2	14.2	6.4	76.7	100
2012	14	11.2	7.5	2.6	9.7	6.5	24.6
2013	100	100	100	100	5.6	0	0.0
2014	7.9	6.7	0.1	0	7.3	2.2	12.2
2015	0.2	0.2	0.3	0.2	0.2	0	3.1
2016	0	0.0	0.2	0.0	1.9	0.1	3.2
2017	19.5	95.4	4.3	0.2	3.8	0.0	0.1
2018	2.6	3.6	0.6	0.0	0.1	0.0	0.0
2019	0.1	0.0	0.4	0.9	0.1	1.0	0.0
2020	1.2	43.7	0.0	0.1	100	100	31.7
2021	11.3	4.2	2.6	0.0	2.1	73.5	48.4

CHAPTER 3

RESULTS – HYDROMETEOR IMAGERS

When developing a method to identify periods of blowing snow based on meteorological observations, it was critical to have separate 'ground truth' measurements. Serving this role were multiple, ground-based hydrometeor imagers including the three LPMs and PIP at NSA. PSDs for each instrument were calculated to determine how they represented periods of blowing snow. The results of this analysis are presented in this chapter. This includes a discussion of the strengths and limitations of each hydrometeor imager and relationships of observed blowing snow periods to meteorological observations.

3.1 PSDs

3.1.1. Characteristics associated with instrument type and location

Mean PSD plots segregated by wind speed are displayed in Fig. 6. A relationship exists between the observed 10 m wind speeds and the PSDs for all LPM instruments. As wind speeds increase, the concentrations of smaller-sized particles increases. The 10 m wind speed threshold for increased concentrations of smaller particles, i.e., particle diameters ≤ 1.125 mm, occurs at approximately $7 - 9$ m s^{-1} for each of the LPM instrument locations (Fig. 6a,c,d). Across all LPMs, counts of smaller particle sizes are similar, although a reduced number of larger particles (> 1 mm) is seen at Oliktok Point (Fig. 6c). As the particle diameter increases, the number of particles decreases for all LPM instrument locations resulting in a tapering, right-hand tail. Each LPM

displays a gamma-like distribution owing to the smaller sized particles. The PIP displays minimal increases in the number of smaller sized particles with increasing 10 m wind speed (Fig. 6b). The gamma-like PSD associated with the LPMs is not observed with the PIP.

To demonstrate the broad changes in PSDs across conditions to ensure either only falling or blowing snow, select PSDs are shown for 10 m winds > 5 m s^{-1} and between 15-20 m s^{-1} (Fig. 7). At wind speeds < 5 m s^{-1}, all instruments display low concentrations of particles with diameters ≤ 1.125 mm (Fig. 7a). At sizes > 1 mm, the PIP observes more particles, but the slope of the distributions is similar to the LPM. These characteristics are not seen for wind speeds between 15 – 20 ms^{-1} (Fig. 7b). The largest increases occur with particles having diameters ≤ 1.125 mm which is expected for periods of blowing snow. Conversely, the PIP displays little to no change in particle concentrations given the increasing wind speeds. Rather, particle counts increase for the largest size bins (> 5 mm), which is physically unrealistic.

The large discrepancies in the overall concentrations between the PIP and LPM are further investigated. Figure 8 shows a time series of the total particle concentrations ≤ 3 mm for the C1 PIP and C1 LPM for 1 November 2019. The LPM reports higher particle concentrations ≤ 3 mm. LPM counts exceed 25,000, whereas the PIP only detects particle counts < 15,000. The PIP struggles with the detection of smaller sized particles. Figure 9 shows a time series of the total particle concentrations > 3 mm for the same event. The overall detection of particles between the two instruments is more similar than shown in Fig.8. Overall, this case study demonstrates the largest differences between the PIP and LPM were observed for smaller sized particles.

3.1.2 Discussion of Hydrometeor Imager performance

A typical blowing snow PSD displays a gamma distribution (Gordon and Taylor 2009; Naaim-Bouvet et al. 2012; Pomeroy and Male 1988; Yu et al. 2020) skewed toward smaller sized particles (Pomeroy and Male 1988). Furthermore, blowing snow is largely a function of wind speed (Li and Pomeroy 1997a,b). As wind speeds increase, more particles are likely to be lofted from the surface into the atmosphere above resulting in blowing snow. With this knowledge in mind, Figs. 6-8 demonstrate that the LPM displays gamma-like distribution PSDs, with higher concentrations of smaller sized particles associated with higher wind speeds (Fig. 6). The PIP on the other hand, only displays gamma-like distribution PSDs for calm wind speeds when falling snow is occurring. No instrument properly represents the small end (i.e., particle sizes < 1 mm) of the blowing snow PSD, which relates to the resolution limits for both instruments (Fig. 6). The negative bias in small particle counts for the PIP cannot be completely attributed to the varying sampling volumes between the two instruments. For example, the LPM has a measuring area of 46 cm^2 (23.0 cm × 2.0 cm) (Pickering et al. 2019) while the PIP has a field of view of 6.4 cm × 4.8 cm for a total area of 30.72 cm^2 (Pettersen et al. 2020).

The performance of the PIP for categorizing small-sized particles (e.g., ≤ 1.125 mm) is poor and suggests this would not be the ideal instrument to identify blowing snow periods. The underestimation of smaller particles by the PIP was also noted in Maahn et al. (2023) when compared to the Video In Situ Snowfall Sensor (VISSS) stationed at the Hyytiälä Forestry Field Station in Helsinki, Finland, for the winter of 2021 – 2022. Maahn et al. (2023) hypothesized that PIP image processing was the source of error. Images captured by the PIP are dilated twice using a 3 × 3-pixel kernel. This process results in particles with a width of 0.4 mm being omitted by the PIP. It's possible that raw images could be re-processed to improve small diameter particle counts, but this is beyond the scope of this study.

The lack of increase for small particles and increase at large particle sizes is in some ways similar to results for the Parsivel[2] found in Loeb and Kennedy (2021). The limitation of the Parsivel[2] was hypothesized to be caused by large concentrations of blowing snow generating voltage signals that were similar to larger diameter particles. Although the Parsivel[2] hypothesized source of error is likely not the error observed in the PIP due to different instrument design (optical versus laser), the Parsivel[2] does operate similarly to the LPM. This suggests that processing routines may also be the culprit for Parsivel[2] errors.

Due to the performance of PIP for small particles, and physically realistic PSDs for the LPM, the NSA C1 Site LPM was selected for the detection of blowing snow for the remainder of this study. While the LPM is not perfect, known issues should not influence this study. For example, a major issue with the LPM in past hydrological studies was the reporting of excessively high concentrations of smaller-sized particles during rain events, due to rain drop breakup (Meshesha et al. 2016). Pickering et al. (2019) also found the LPM struggled to capture graupel in mixed-phase precipitation events along with issues associated with particle velocity. Considering the study herein was restricted to the Arctic winter (the temperature regime was limited to temperatures ≤ 0 ˚C) and particle velocities were not used due to the turbulent nature of blowing snow events, these issues are not expected.

3.2 RELATIONSHIP OF BLOWING SNOW TO METEOROLOGICAL VARIABLES

To develop a method of blowing snow detection based purely on meteorological variables, a variety of analyses were created to determine the best set of meteorological thresholds that predict blowing snow occurrence. First, this section presents 2-D histograms segregated by wind speed and temperature for various particle count thresholds. Second, this section discusses the

results of a forecaster's 2 × 2 contingency table analysis on a variety of meteorological variables. Finally, this section concludes with a discussion of the meteorological thresholds selected to identify blowing snow periods.

3.2.1. 2-D Histograms

The large change in particle counts at small particle sizes suggested particle count thresholds could be used to ensure blowing snow occurrence. An initial particle count threshold was selected as shown in Fig. 6. At approximately 200 particles per sampling period, counts rapidly increased owing to increased 10 m wind speeds. Higher particle count thresholds of 300, 500, 1000, 2000, and 5000 were tested with increased confidence that blowing snow was occurring for larger particle counts. Tests were performed to understand the lowest particle count threshold that could be used to guarantee blowing snow without accidently including pure falling snow cases.

Similar to Loeb and Kennedy (2021), 2-D histograms segregated by wind speed and temperature were made for each particle count threshold (Fig. 10) as well as a 2-D histogram showing the total number of times different meteorological conditions were observed (Fig. 11). For all thresholds, the largest concentration of events occurred at temperatures -10 - -25 ˚C with at winds between 7 –13 ms^{-1}. The results of this analysis demonstrate that particle thresholds of ≥ 200 and ≥ 300 particles include many events at wind speeds < 5 ms^{-1}. Further, as the particle count threshold increases toward and past ≥ 1000, the number of events observed at wind speeds < 7 m s^{-1} steadily drops off. For example, the number of 5-min periods with particle counts ≥ 5000 was 754 versus 4341 for counts ≥ 1000.

The relationship of blowing snow with respect to temperature is more difficult to discern. The bimodal nature of blowing snow occurrence (local maxima near -5 - 0 ˚C and -10 - -25 ˚C)

appears to be a function of the frequency of different meteorological conditions. This is confirmed when the frequency of blowing per meteorological bin is calculated (Fig. 12) which is simply a result of taking the data displayed in Fig. 10 divided by Fig. 11. Although noise is present along the upper tier of bins due to the rarity of these conditions, a broad increase in frequency is seen with increasing wind speed. At temperatures < -10 ˚C there is a general increase in blowing snow frequency that is more prevalent at lower wind speeds. For example, blowing snow frequency increases from 0.45 at wind speeds of $5 - 7$ m s^{-1} to .9 for particle counts ≥ 1000 for the $7 - 9$ m s^{-1} bin (Figure 12d).

3.2.2. Meteorological Thresholds

A forecaster's 2 × 2 contingency table analysis was used to analyze optimum thresholds for wind speed, mean visibility, temperature, and relative humidity to successfully detect blowing snow occurrence. The results of this analysis are provided in Tables 5-8 and Figs. 13-18. Figures 13-17 display 2-D histograms of the CSI, POD, FAR, HSS, and frequency for each particle count threshold. Figure 18 displays 2-D histograms of the HSS for each temperature bin for a particle count threshold of ≥ 1000. Table 5 displays the wind speed thresholds for each temperature bin and particle count threshold. Table 6 displays the calculated R-squared, particle imager frequency, MET frequency, and the associated HSS values for each temperature bin. The wind speed thresholds for the ≥ 500 particle count threshold are all ≤ 5.5 m s^{-1}, which is on the lower end of blowing snow wind speed thresholds (Mellor 1965). Further, the largest FAR values are observed in the regions of best reported frequencies (e.g. frequency = 1). The ≥ 500 particle count threshold displays the highest R-squared value of all thresholds, however, the bias is the highest out of the thresholds at 5.71%. The wind speed thresholds found using a particle count threshold of ≥ 1000 display a marginal increase in wind speed with cooling temperatures. At a temperature range of 0

- -5 ˚C, the wind speed threshold is 3.5 m s^{-1}, whereas at a temperature range of -25 - -30 ˚C, the threshold is 7 m s^{-1}. The overall change in wind speed thresholds with respect to temperature are quite small. The regions of optimized frequency coincide with the regions of lowest FAR values. The overall blowing snow frequency calculated for the temperature dependency method with a threshold of ≥ 1000 particle count is within +1.6% of truth. The temperature dependency method with a threshold of ≥ 1000 particle count has an R-squared value of 0.85. The temperature dependency method with a threshold of ≥ 1000 particle count performs the best in comparison. Wind speed thresholds found using the particle count threshold of ≥ 2000 closely resemble the pattern in wind speed seen in the values using the particle count threshold of ≥ 1000. The frequency bias is + 3.01% with an R-squared value of 0.83. The largest wind speed thresholds are observed using a particle count threshold of ≥ 5000. Additionally, the lowest R-squared value is found using this threshold. Due to the minimal cases meeting this threshold in colder temperatures, sampling errors arose impacting the FAR and CSI values reported for temperatures < 20˚C.

The results of the particle count threshold analysis omitting temperature dependency are now discussed. Figures 13-15 and Fig. 17 display the 2-D histograms of the FAR, POD, CSI, and frequency for each particle count threshold. Figures 16 displays the HSS for each particle count threshold. Table 7 displays the wind speed thresholds calculated for each particle count threshold while Table 8 displays the calculated R-squared, particle imager frequency, MET frequency, and the associated HSS values for each threshold. The wind speed thresholds for each particle count threshold without the inclusion of temperature are all equal to the average of the wind speed thresholds for each temperature bin and particle count threshold. The HSS values are all less than the values observed including temperature dependency. The bias values for each particle count

threshold are higher than that of the values in Table 6. In terms of overall frequency performance, the particle count threshold of ≥ 2000 results in only a + 1.78% bias.

Relative humidity taken at 2 m with respect to ice was included in the analysis to understand how it was related to blowing snow conditions (Fig. 19). In the past, this variable was used to help remove fog cases (Loeb and Kennedy 2021). Relative humidity has also been shown to play a role in the thermodynamic profile of blowing snow (Taylor 1998). The inclusion of a relative humidity threshold did not result in any improvement regardless of the methodology used. In fact, HSS and R-squared values calculated using wind speed, visibility, and relative humidity thresholds were substantially reduced (e.g., HSS values all < 0.3) and thus, no further insight was gained. Due to the lack of improvement in HSS and R-squared values, relative humidity was not included in the calculations of MET frequency.

3.2.3. Meteorological Threshold Performance Discussion

As the temperature decreased from 0 - -25 ˚C, the wind speed threshold showed no significant change (Table 5). Wind speed magnitudes increased on the order of $2 - 2.5$ ms^{-1}. The increase in wind speeds, however, was not consistently observed. For example, for particle count thresholds ≥1000, the wind speed decreased as the temperature went from -15 - -20 ˚C to -20 - -25 ˚C. Furthermore, the decrease in winds for that temperature bin was observed on all remaining particle count thresholds (Table 5). An increase in wind speed for all particle count thresholds was observed in the -25 - -30 ˚C temperature bin. Wind speed magnitudes increased on the order of 0.5 – 2 ms^{-1}. Minimal blowing snow cases existed at temperatures < -35 ˚C and, therefore, no comparison was made. The lack of a clear observed relationship between wind speed, temperature, and blowing snow occurrence has also been seen in the work of Loeb and Kennedy (2021), although prior studies have suggested the initiation of blowing snow is dependent on temperature

(Li and Pomeroy 1997a). Li and Pomeroy (1997a) stated that there is an observed relationship between the wind speed threshold and temperature. From 0 - -25 ˚C, Li and Pomeroy (1997a) found that wind speed thresholds increase with increasing temperature and for temperatures < -25 ˚C, wind speed thresholds marginally increase. Discrepancies between the results here and Li and Pomeroy (1997a) are hypothesized to be due to several factors. The first factor is Li and Pomeroy (1997a) focused on the wind speed thresholds for blowing snow initiation, whereas this study analyzed the duration of blowing snow events. Furthermore, this study was not strictly confined to pure blowing snow periods. Blowing snow conditions can be observed in conjunction with active precipitation. The current analysis did not segregate purely blowing snow events. The results found in this study suggest that there might be some pure falling precipitation events being filtered into the blowing snow analysis. Another key difference between the current work and Li and Pomeroy (1997a) is the geographic locations. Li and Pomeroy (1997a) focused on the Canadian prairies. The Canadian prairies contain more vegetation than NSA (Fang and Pomeroy 2009). Lastly, NSA is located at a higher latitude meaning that the thawing and refreezing of the snowpack is less likely than in the Canadian prairies.

Blowing snow frequencies derived using the wind speed and visibility values resulted in a slight overestimation of blowing snow conditions for each particle count threshold on the order of 1 – 6%. An overestimation of blowing snow frequency was also observed for MET frequencies derived without the inclusion of temperature. Similar findings were found in Gossart et al. (2017) and Chen et al. (2022). This overestimation in thresholds of particle counts of ≥ 500 and ≥ 1000 may be due to the inclusion of falling snow periods. The removal of falling snow periods to isolate pure blowing snow is a challenge in blowing snow research. For particle counts of ≥ 500 and ≥ 1000, the lowest temperature bins showed a wind speed threshold on the order of 3 m s^{-1}. Despite

3 m s^{-1} being denoted as a potential blowing snow threshold by Mellor (1965), the likelihood of observing ≥ 1000 particles with winds at 3 m s^{-1} without the presence of falling precipitation is negligible. Wind speeds associated with particle count thresholds ≥ 2000 and ≥ 5000 were more conducive to pure blowing snow conditions. These wind speeds were between 5.5 – 8.5 m s^{-1}.Although these wind speeds were more conducive to blowing snow, the R-squared values decreased, and frequency biases increased from the values observed for the particle count threshold of ≥ 1000. This suggests that despite having a wind speed threshold of 3 m s^{-1}, the temperature dependent MET method with a ≥1000 particle count threshold still optimizes the detection of blowing snow.

The wind speed thresholds found without the dependency of temperature were all greater than 4 m s^{-1} and increased with the increasing particle count threshold. The wind speed thresholds found omitting temperature dependency were equal to the average of each temperature bin in Table 5. Larger biases were found when temperature was omitted (Table 8). R-squared values were like those found using temperature.

Synthesizing Tables 5-8 and Figure 18, the temperature dependent MET method with a ≥ 1000 particle count threshold optimized the detection of blowing snow periods. This method had the lowest bias at +1.6% and an R-squared value of 0.85. Furthermore, the regions of lowest FAR coincided with the regions of best calculated frequency. Periods of maximum particle concentrations and lower visibilities aligned with observed temperature and wind speeds. For these reasons, the temperature dependent MET method with a ≥ 1000 particle count threshold was selected as the parameters used to identify blowing snow periods. The visibility threshold used was 9 km and the wind speed values used for each temperature bin are found in Table 5.

3.2.4. Other Factors Influencing Blowing Snow

Once the ≥ 1000 particle count threshold was chosen, blowing snow intensity and occurrence was explored as a function of snow age, visibility, wind speed, and temperature. The intent of this analysis was to distinguish how each factor influenced blowing snow. Figure 20 displays a scatter plot of particle count and visibility colored by temperature. The lowest visibilities are associated with the largest particle counts and temperatures ranging from 0 ˚C to -10 ˚C. The large concentration of particles observed for these temperatures is likely due to the combination of falling precipitation and blowing snow. This is expected as warmer temperatures are more conducive to falling precipitation. Few cases of blowing snow are observed for temperatures < -25˚C. This could be due to the increased cohesion and kinetic resistance of the aged snowpack (Li and Pomeroy 1997a). If the snowpack is compacted, there are minimal particles available to be lofted and/or the wind speed required to dislodge particles is substantially higher than if there was fresh snow on the surface (Li and Pomeroy 1997a).

The region of lowest visibility and highest particle concentrations is observed when prior precipitation has occurred < 12 h from the observation (Fig. 21). This supports the idea that during this timeframe, there is active precipitation occurring, or had just occurred. There are several cases of large particle concentrations associated with low visibility for times precipitation had not occurred recently (> 72 h). These times are likely periods of blowing and/or drifting snow with no falling precipitation. The median days since last precipitation for each 1000 m visibility bin and the associated median wind speed are displayed in Fig. 22. There is a balance between fresh snow and older snow. In the lowest visibility bins, regardless of the snow age, the fastest winds are observed. The median wind speeds decrease with increasing visibility. In other words, strong winds are needed to reduce the visibility.

A roughly logarithmic relationship is seen between particle count and visibility with the most intense periods associated with the strongest wind speeds (Fig. 23). There is a significant reduction in visibility as particle concentrations increases. For example, the 0 – 1000 m visibility bin shows ~30,000 particles whereas, the 1000 – 2000 m visibility bin shows ~15,000 particles (Fig. 24). Particle concentrations are increasing owing to the increase in small sized particles. In Fig. 24, the largest concentrations are in particle diameters ≤ 1.125 mm.

Blowing snow has been demonstrated to be dependent on snow age, wind speed, and temperature (Li and Pomeroy 1997a). Such variables were analyzed in this study, however, in practice such variables provided no additional insight on the intensity and occurrence of blowing snow. Figures 20-24 demonstrated that the identified blowing snow periods occurred in situations during or immediately following precipitation and during periods where precipitation had not occurred in > 2 days. Overall, the lowest visibilities were associated with the highest particle concentrations and the fastest wind speeds.
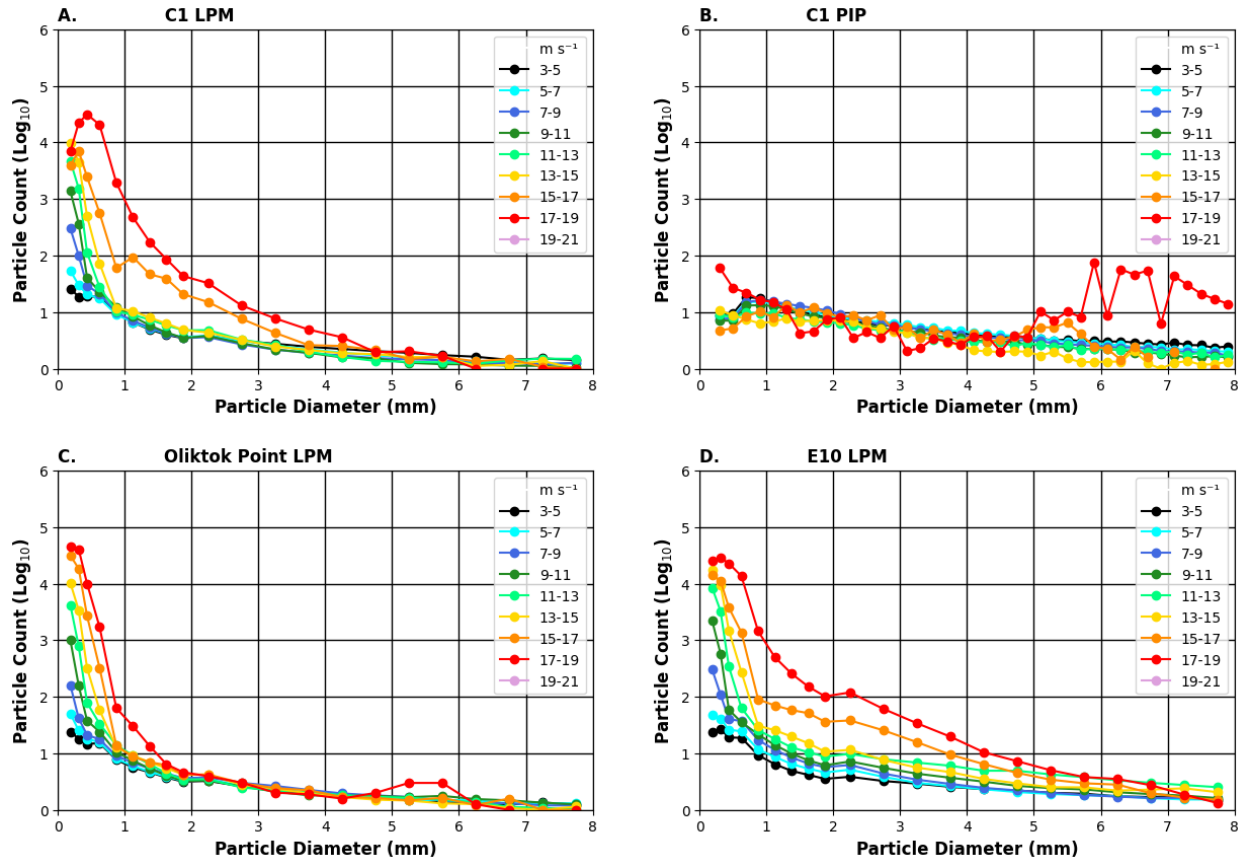
Figure 6: PSDs by wind speed for (A) NSA C1 LPM, (B) NSA C1 PIP, (C) Oliktok Point LPM, and (D) NSA E10 LPM. The particle count threshold was set to > 0 and the particle diameter threshold was set to ≤ 8 mm. All counts are for 5-min bins.
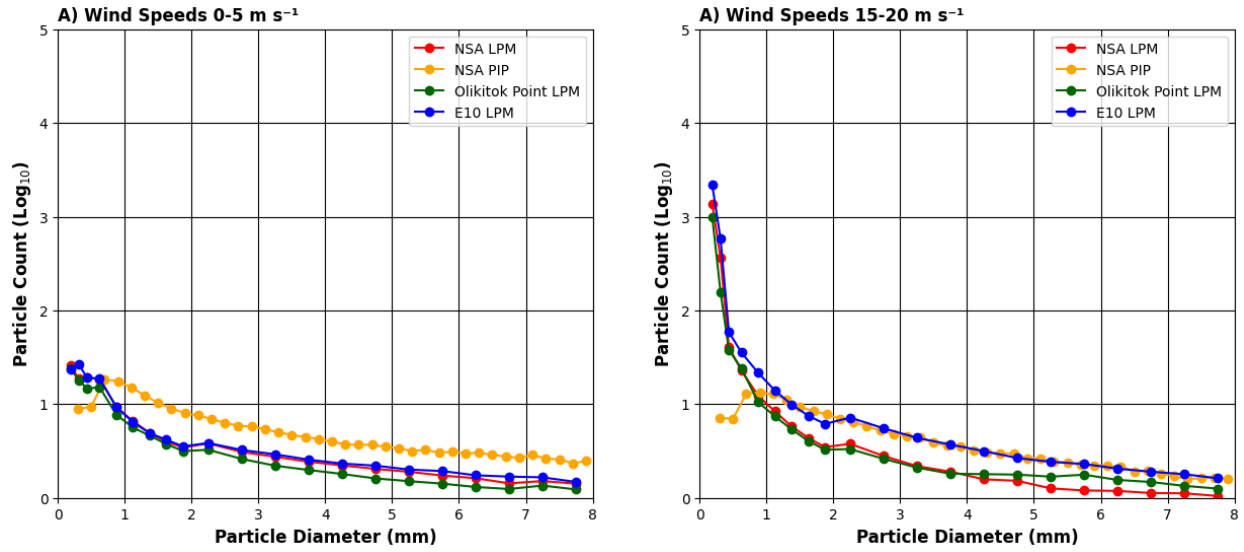
Figure 7: Mean PSDs segregated by instrument for wind speeds between (A) 0-5 m s^{-1} (falling snow) and (B) 15-20 m s^{-1} (blowing snow).
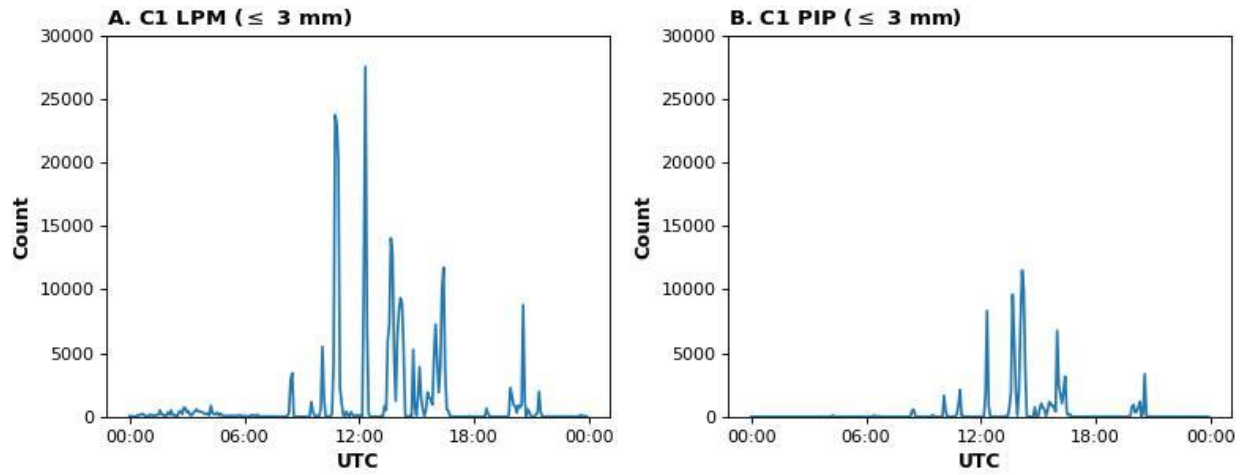
Figure 8: Time series of small particle counts (diameters ≤ 3 mm) on 1 November 2019 for (A) NSA C1 LPM and (B) NSA C1 PIP.
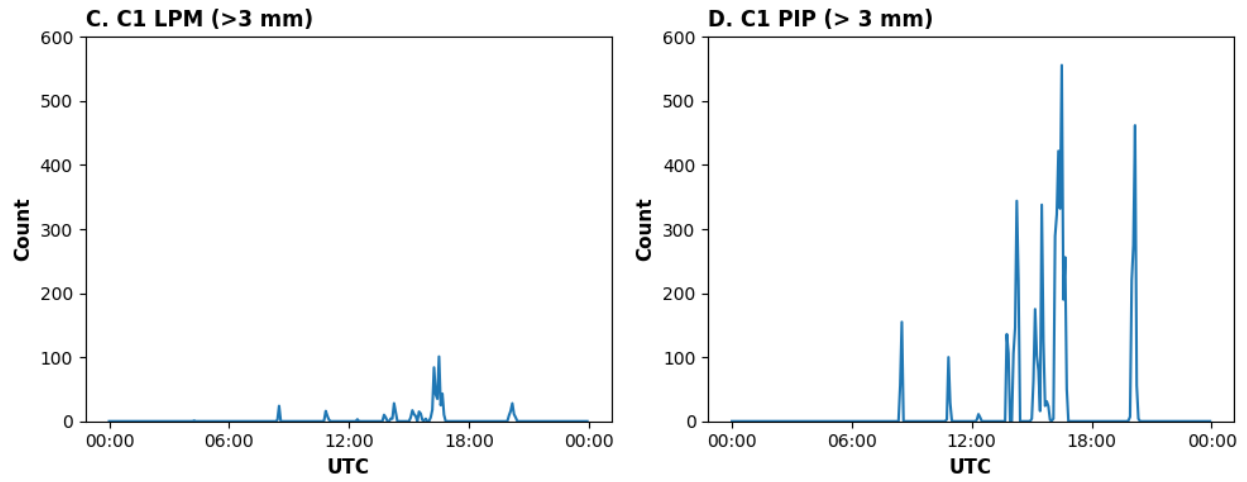
Figure 9: As in Figure 8 except for large diameter (diameters > 3 mm) particles.
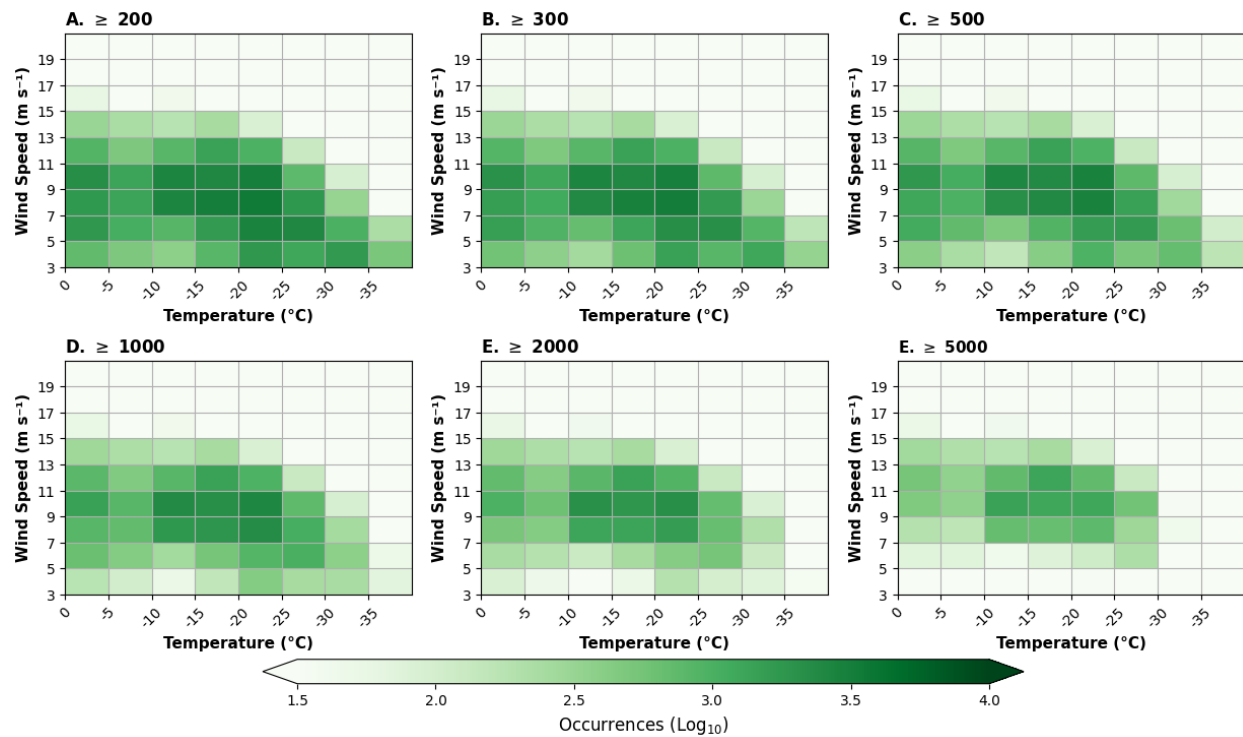
Figure 10: 2-D histograms segregated by wind speed (m s^{-1}) and temperature (°C) for particle count thresholds of (A) ≥ 200, (B) ≥ 300, (C) ≥ 500, (D) ≥ 1000, (E) ≥ 2000, and (F) ≥ 5000
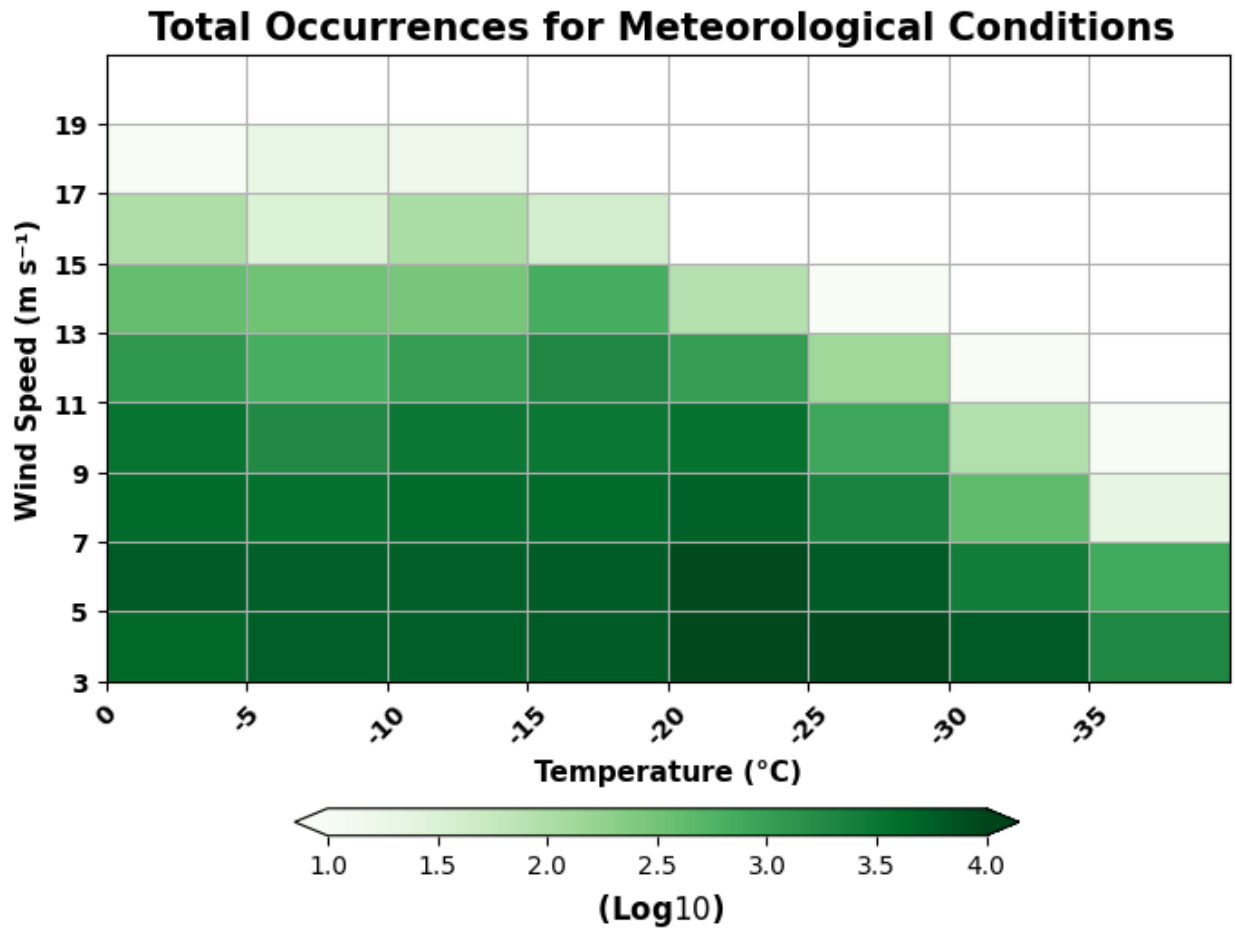
Figure 11: 2-D histogram showing the total number of times that the set of different meteorological conditions were observed.
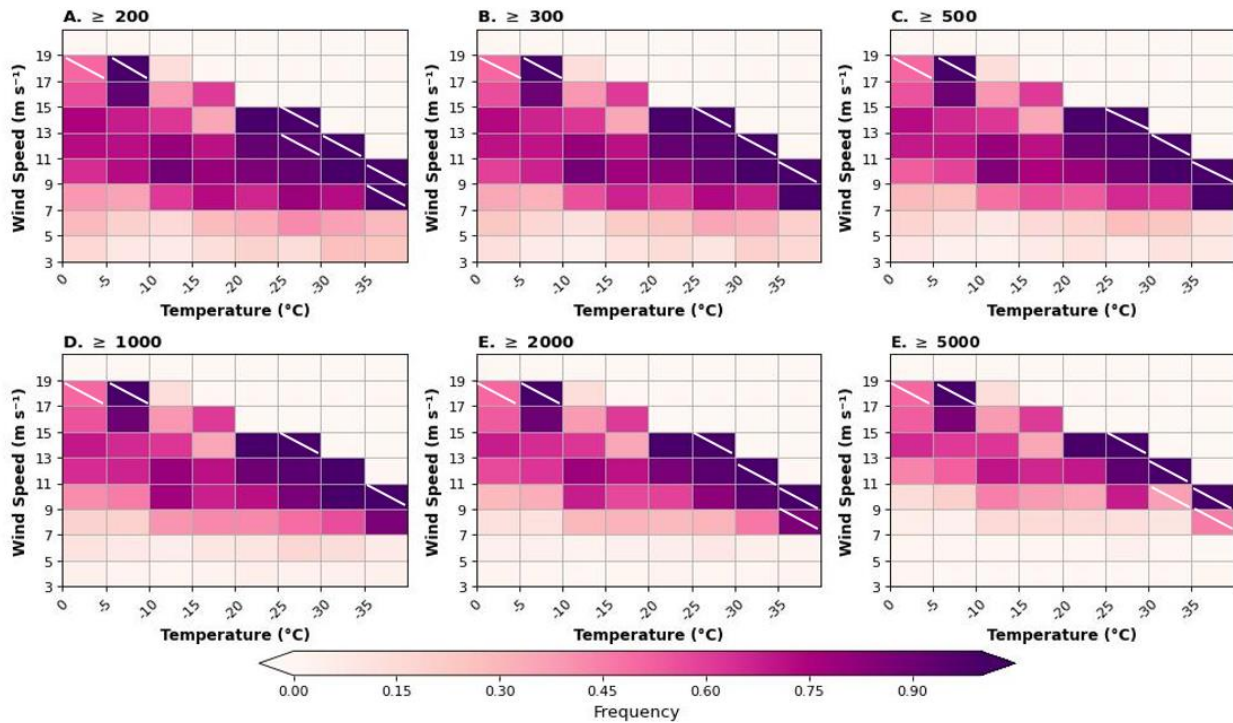
Figure 12: 2-D histograms showing the frequency of each set of different meteorological conditions for particle count thresholds of (A) ≥ 200, (B) ≥ 300, (C) ≥ 500, (D) ≥ 1000, (E) ≥ 2000, and (F) ≥ 5000. The white slashes represent bins that contained > 20 times.
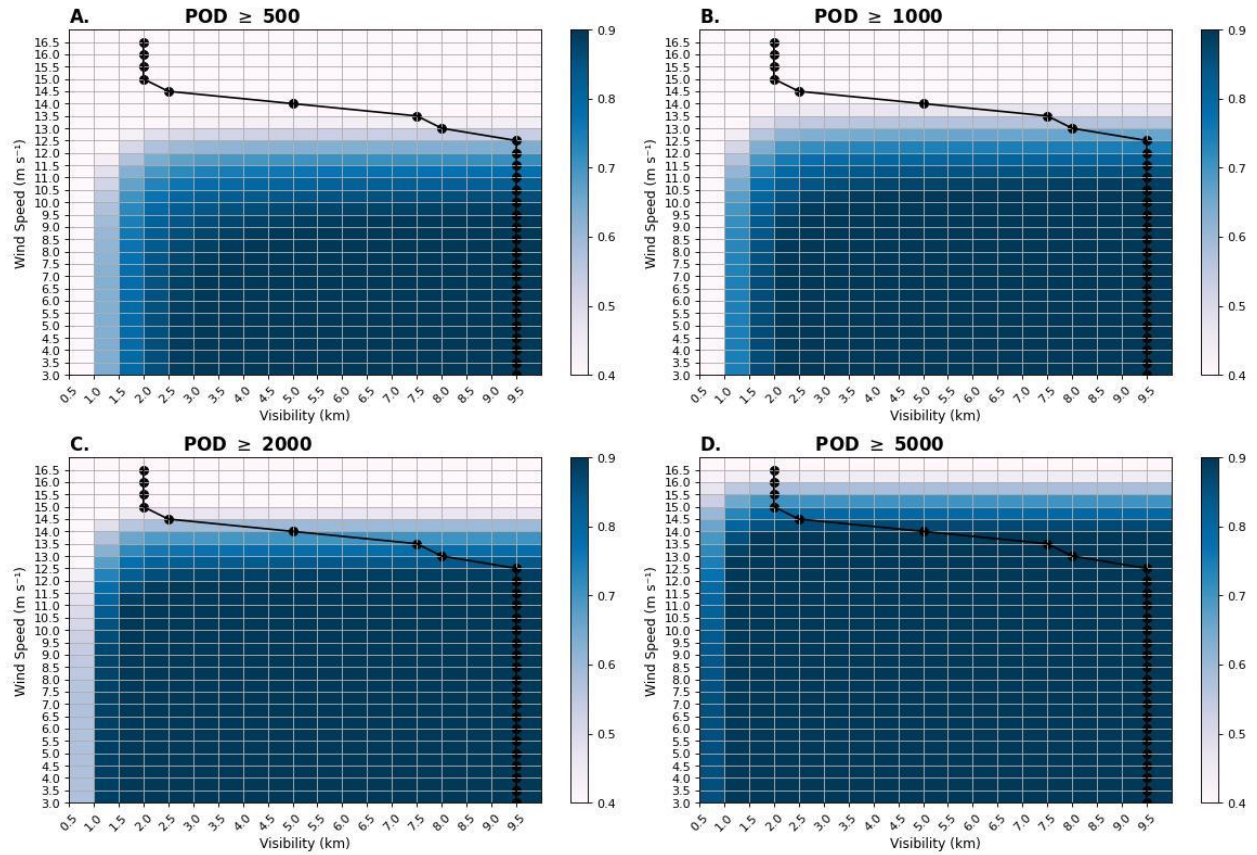
Figure 13: POD values calculated for each wind speed and visibility bin for particle count thresholds of A) ≥ 500, B) ≥ 1000, C) ≥ 2000, and D) ≥ 5000. The black line indicates the highest POD value for each row of wind speed.
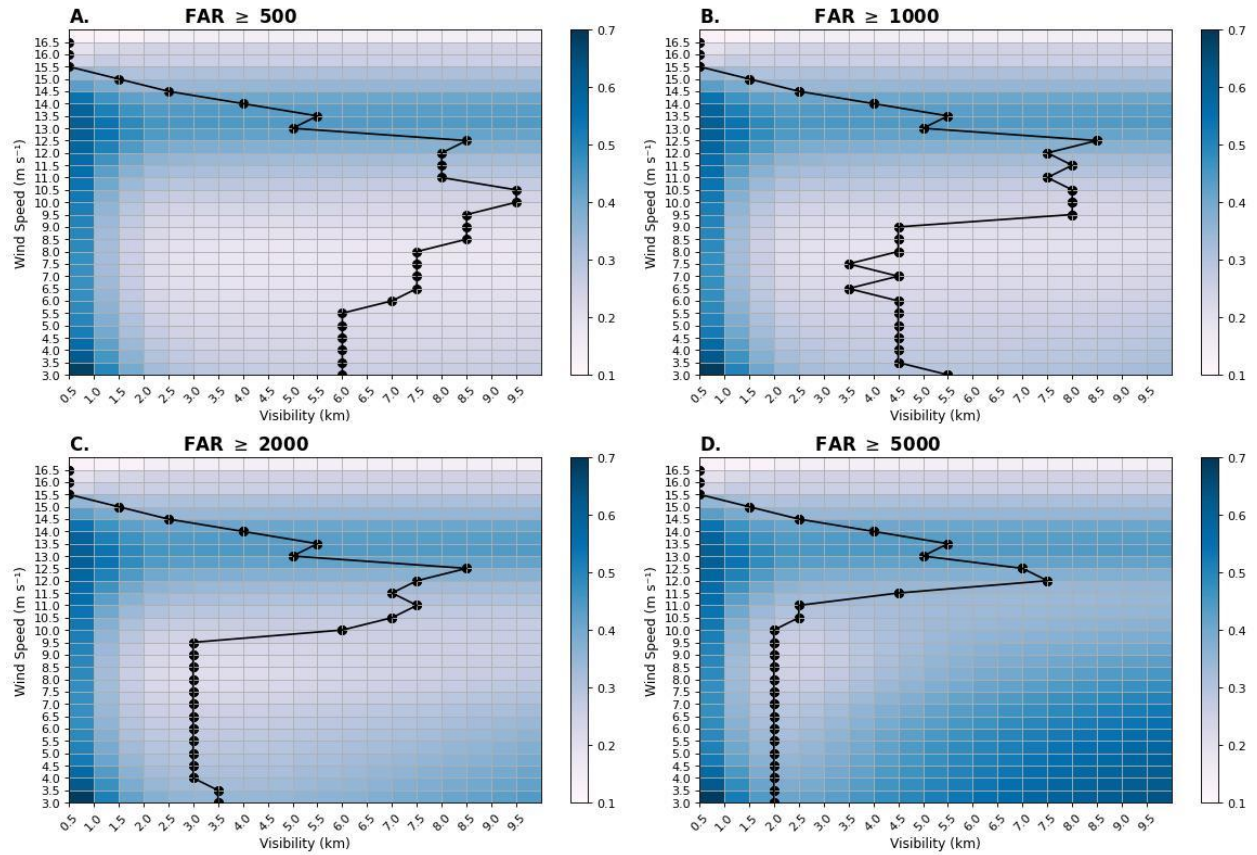
Figure 14: As in Figure 13 except for FAR. The black line indicates the lowest FAR value for each row of wind speed.
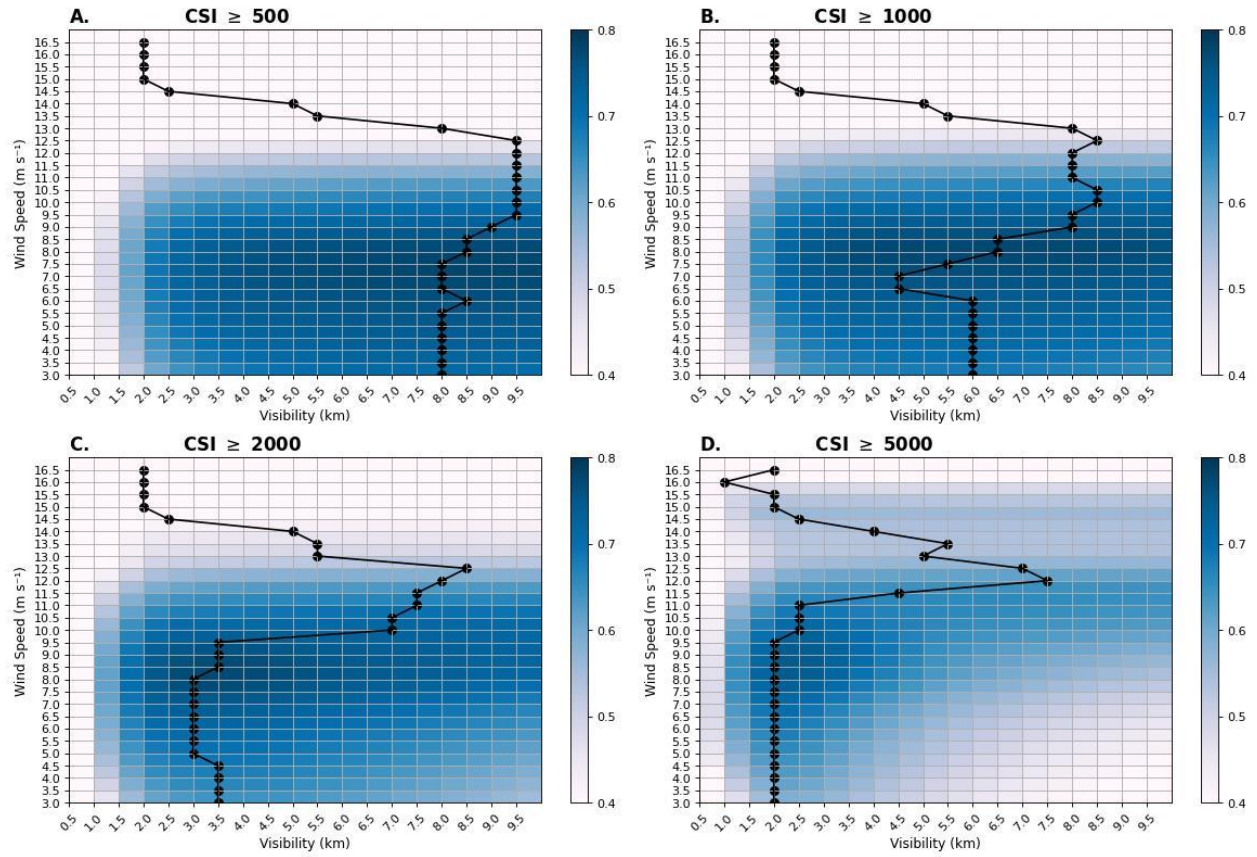
Figure 15: As in Figure 13 except for CSI. The black line indicates the highest CSI value for each row of wind speed.
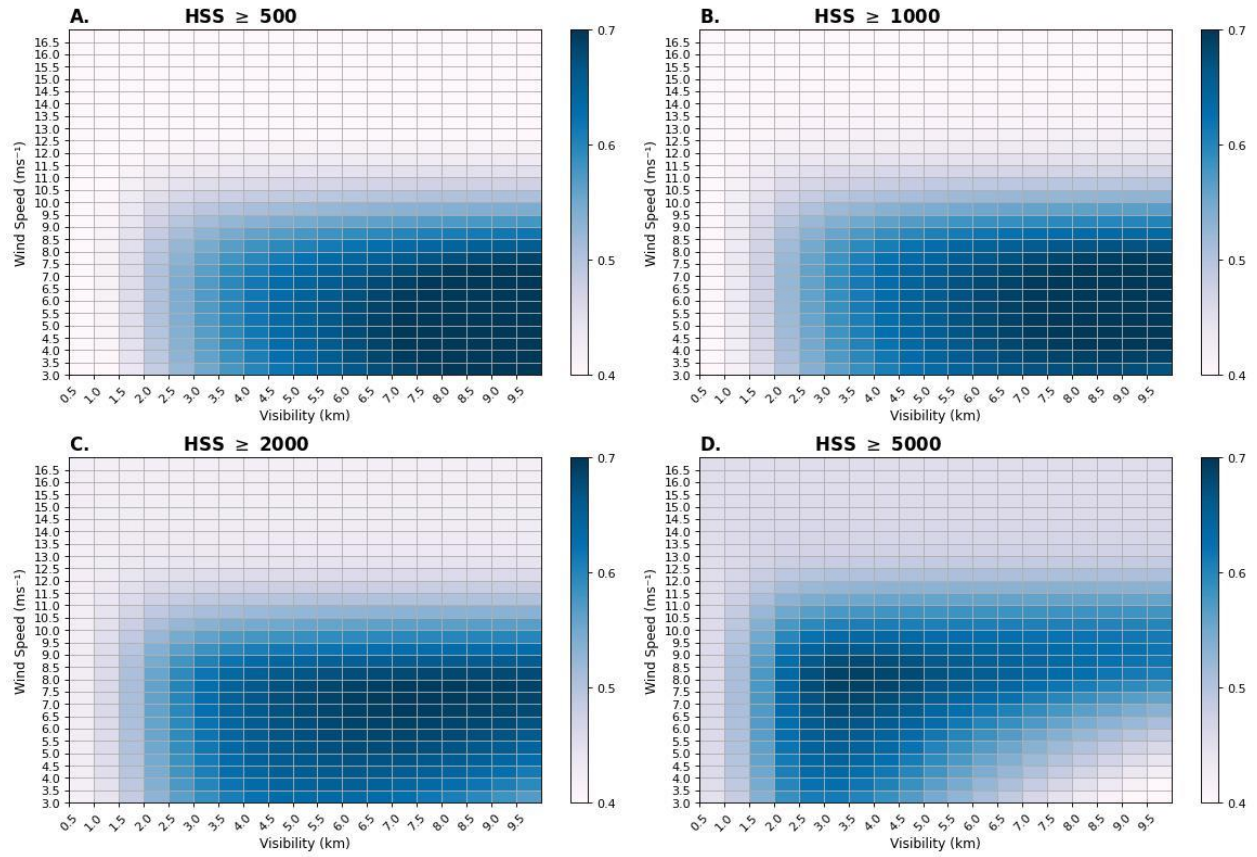
Figure 16: As in Figure 13 except for HSS. The black line indicates the highest HSS value for each row of wind speed.
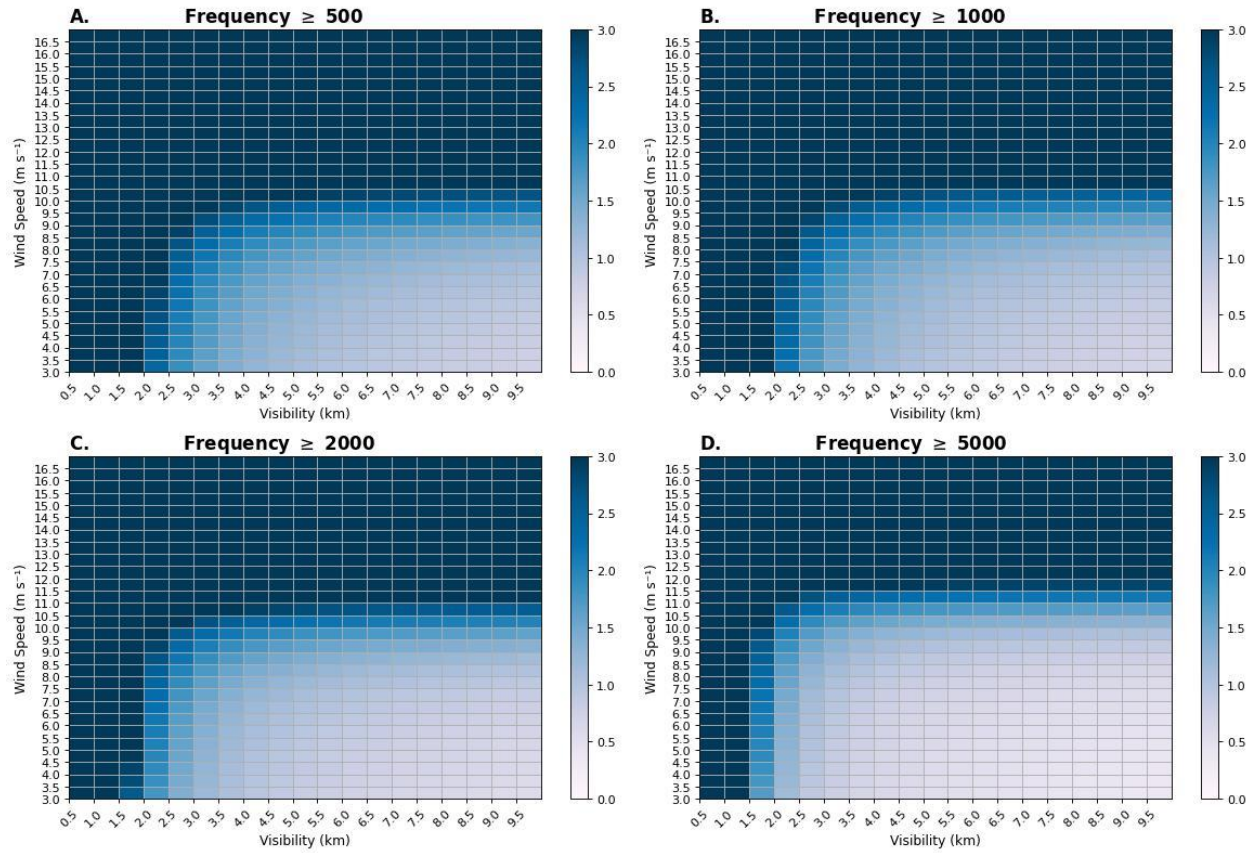
Figure 17: As in Figure 13 except for frequency. A value of one represents no bias compared to the particle count.
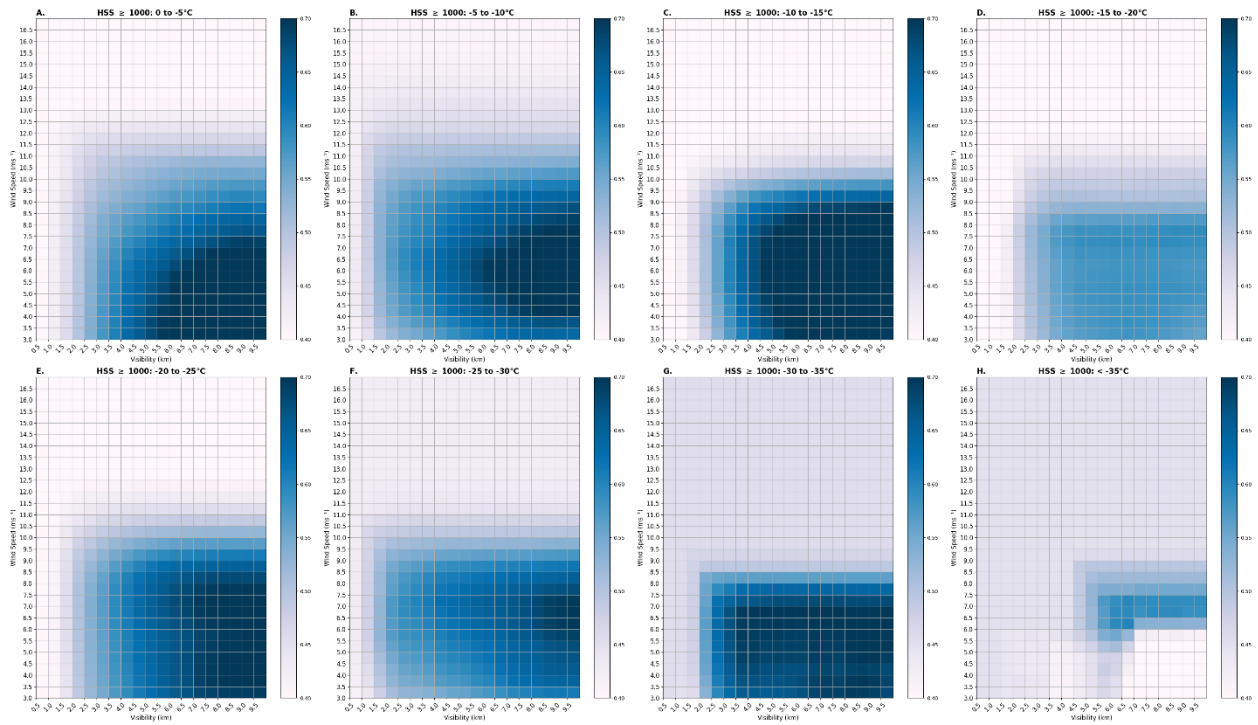
Figure 18: HSS values calculated for each temperature bin and a particle count threshold of ≥ 1000. The black line indicates the highest HSS value for each row of wind speed.
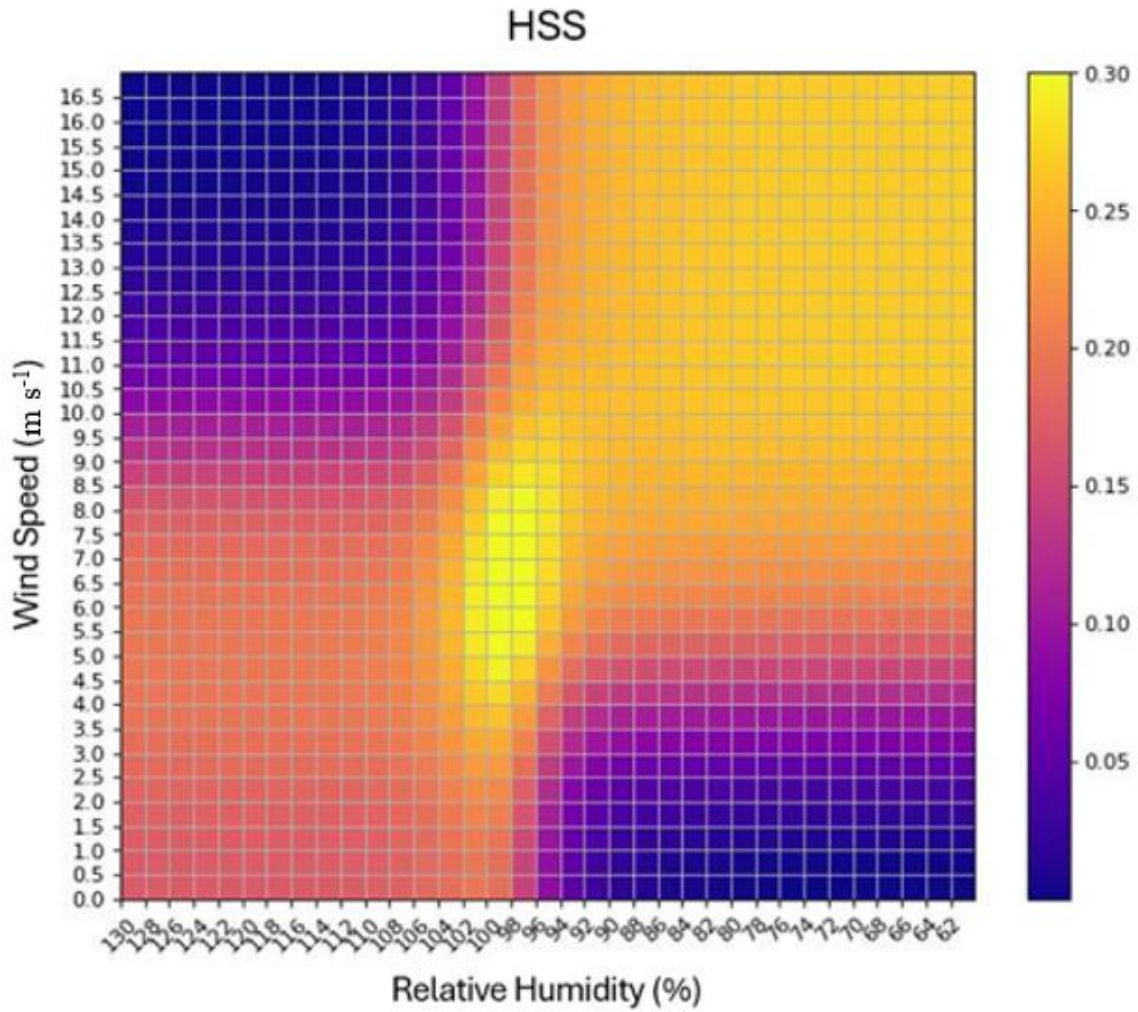
Figure 19: HSS as a function of wind speed and relative humidity (with respect to ice). A visibility threshold of ≤ 9 km was applied.
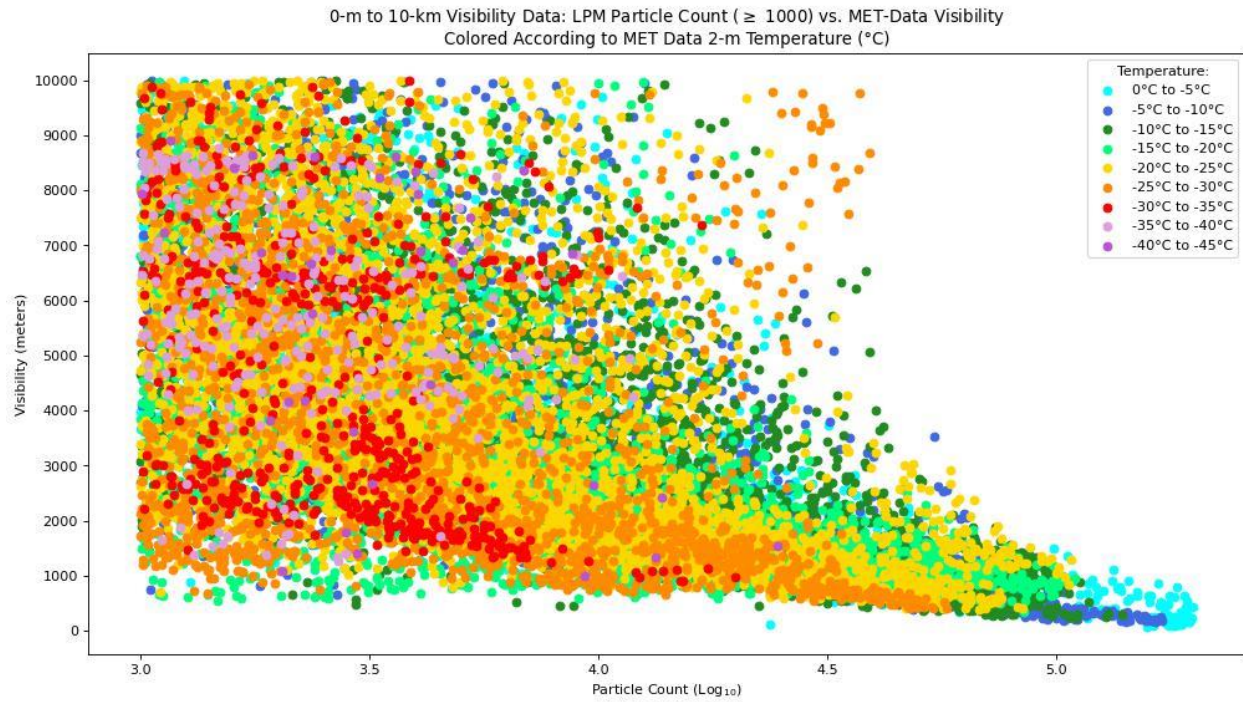
Figure 20: LPM particle count plotted against visibility. Individual observations are colored by temperature.
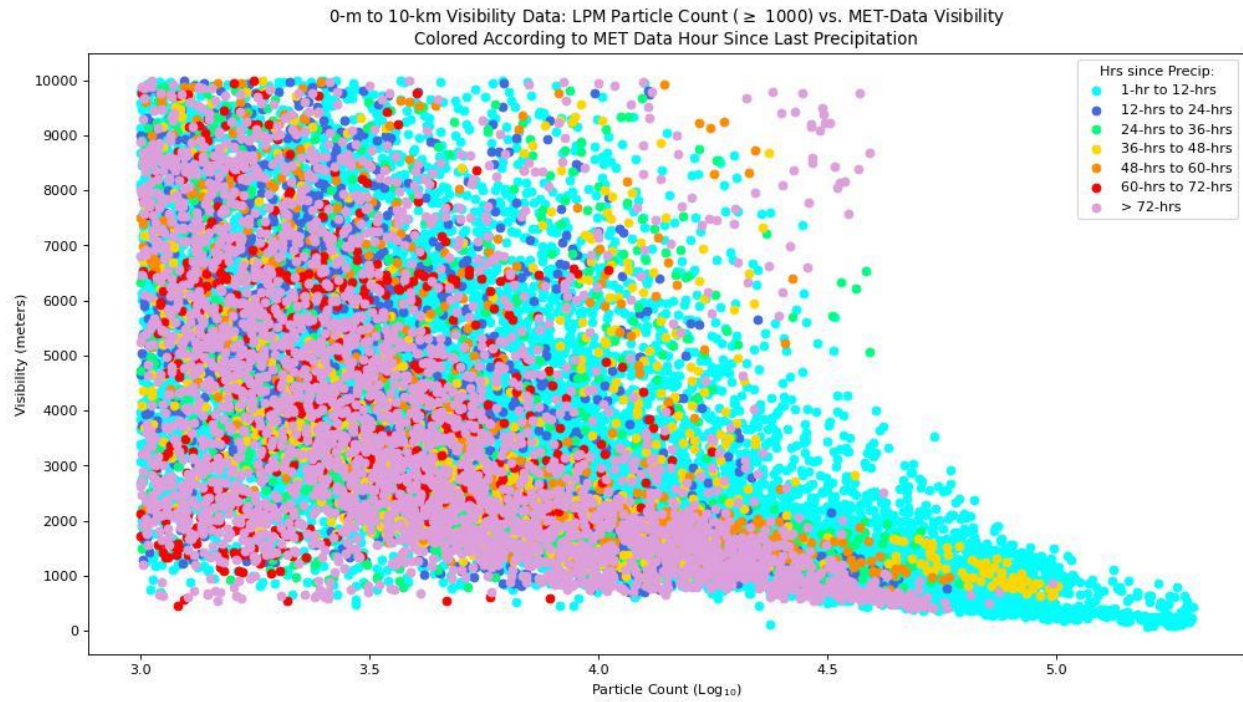
Figure 21: LPM particle count plotted against visibility. Each data point is colored according to the hours since last precipitation.
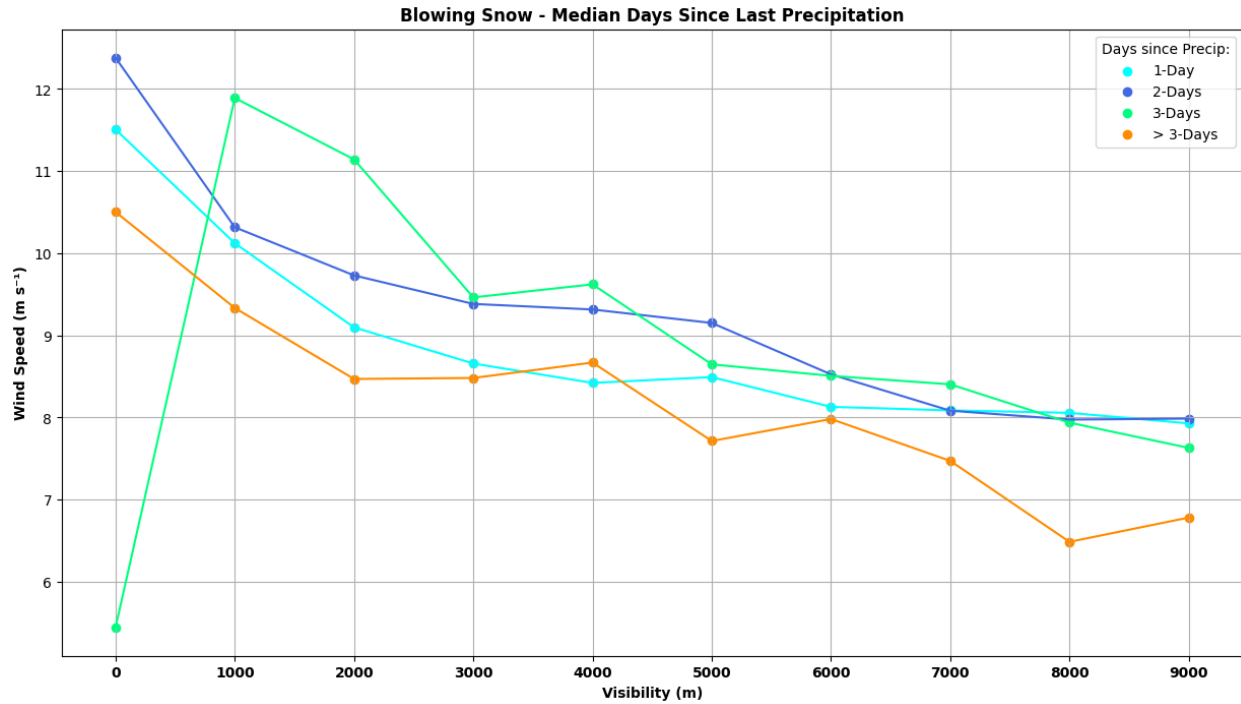
Figure 22: Line plot displaying the median visibility and wind speed for every 1000 m visibility bin segregated by days since last precipitation.
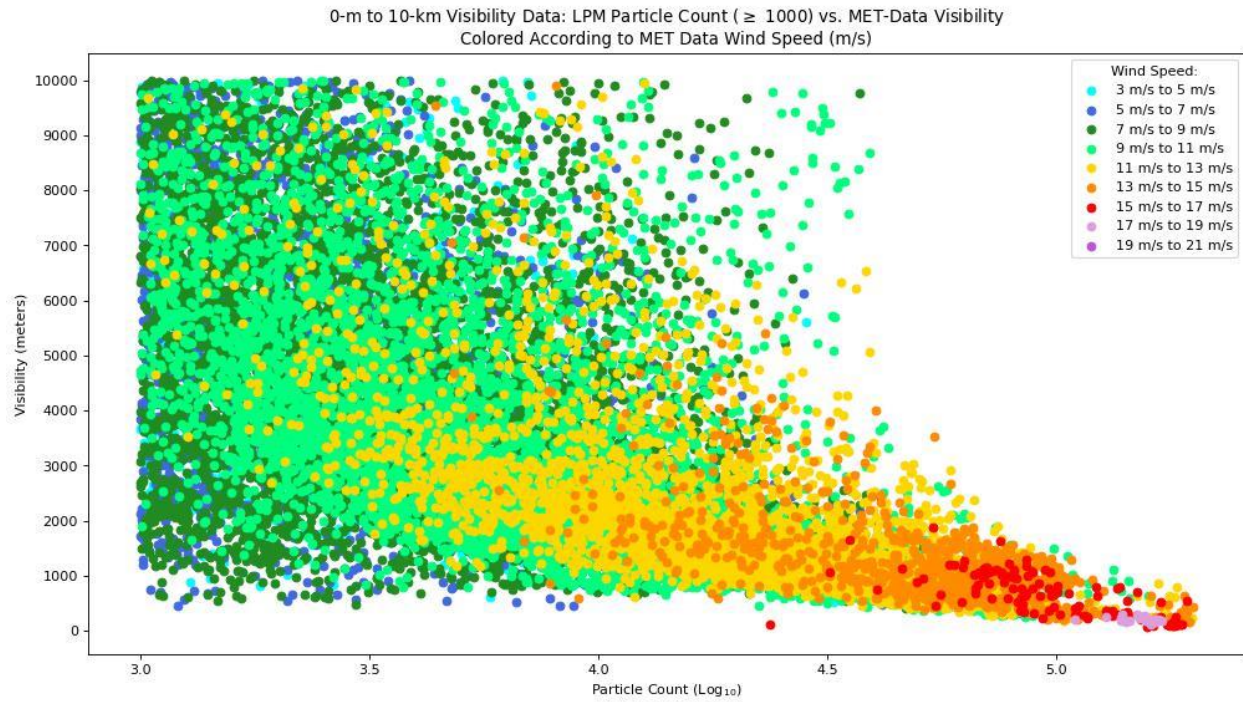
Figure 23: LPM particle count plotted against visibility. Each data point is colored according to wind speed.
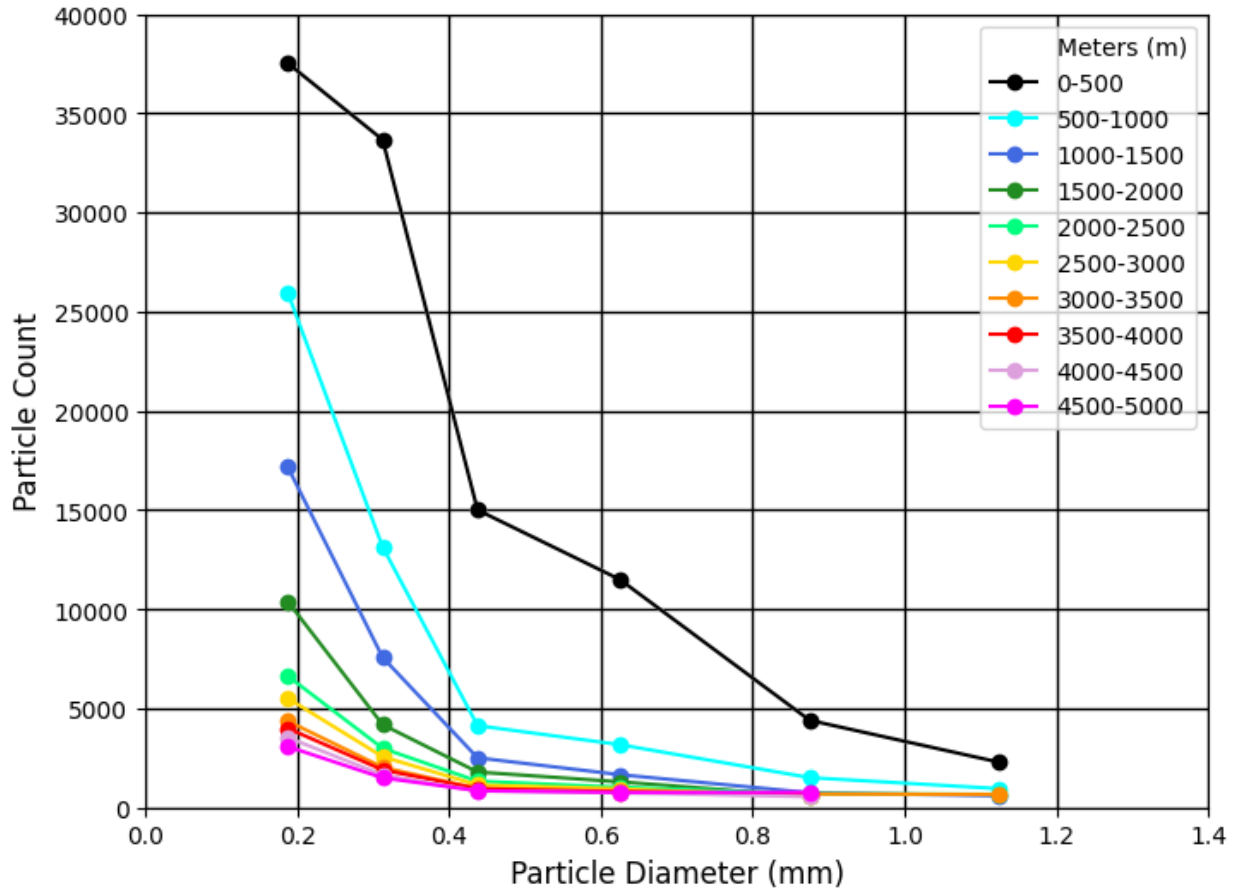
Figure 24: PSD plot segregated by visibility for periods of blowing snow.

Table 5: Wind speed thresholds for each temperature bin using the MET method.

Temperature Range	≥ 500 (m s⁻¹)	≥ 1000 (m s⁻¹)	≥ 2000 (m s⁻¹)	≥ 5000 (m s⁻¹)
0 ˚C to -5 ˚C	3	3.5	5.5	6
-5 ˚C to -10 ˚C	5.5	6	6	6.5
-10 ˚C to -15 ˚C	5	6	7	7
-15 ˚C to -20 ˚C	4.5	7	7.5	7.5
-20 ˚C to -25 ˚C	3.5	6.5	7	7
-25 ˚C to -30 ˚C	5.5	7	8	8.5
-30 ˚C to -35˚C	5	6.5	7.5	8.5
< -35˚C	4	6.5	7	8.5

Table 6: Temperature dependent MET method calculation results.

Particle Count Threshold	Temperature Dependent HSS	R-Squared	Particle Imager Frequency	MET Frequency	Bias
500	0.8,0.8,0.76,0.79,0.58,0.7,0.71	0.90	37.07%	42.78%	5.71%
1000	0.81,0.76,0.8,0.61,0.75,0.78,0.78	0.85	33.96%	35.56%	1.6%
2000	0.76,0.75,0.79,0.59,0.67,0.72,0.72	0.83	28.28%	31.29%	3.01%
5000	0.76,0.74,0.74,0.6,0.6,0.6,0.6	0.72	18.73%	20.98%	2.25%

Table 7: MET method wind speed thresholds without the inclusion of temperature.

Particle Count Threshold:	≥ 500	≥ 1000	≥ 2000	≥ 5000
Wind Speed (m s^{-1})	4.5	6	7	7.5

Table 8: MET method calculation results derived without the inclusion of temperature.

Particle Count Threshold	HSS	R-Squared	Particle Imager Frequency	MET Method	Bias
500	0.74	0.88	36.19%	43.12%	6.93%
1000	0.71	0.86	33.08%	37.67%	4.59%
2000	0.69	0.80	27.4%	29.18%	1.78%
5000	0.69	0.71	17.85%	21.67%	5.82%

CHAPTER 4

RESULTS – HISTORICAL BLOWING SNOW RECORD

To develop a historic record of blowing snow, the meteorological thresholds determined in Chapter 3 were applied to all meteorological data to derive a climatological frequency of blowing snow for SOM nodes. These frequencies were then applied to the historical record of atmospheric states to retrieve a historic record of blowing snow from 1979 to 2022. Blowing snow trends were assessed from the SOM-only blowing snow frequency. This chapter will discuss the results of this analysis. First, the winning SOM will be introduced. Second, the results of the climatological frequency of blowing snow will be discussed. Third, the historic blowing snow frequencies will be covered. Lastly, the blowing snow trends will be discussed.

4.1 SOMs

4.1.1 Winning SOM

The first step to derive the climatological frequency of blowing snow was to establish a winning SOM. As mentioned prior, a winning SOM is defined as a SOM in which 1) spatial distribution of node frequency is present, 2) connectiveness between nodes exists with minimal distortion, and 3) surface high- and low-pressure systems are plotted on opposing sides of the SOM feature map. An 8 × 5 MSLP-only trained SOM was selected (Fig. 25). This SOM was trained using a learning rate of 0.0005 and a sigma of 4. The selected values for sigma and the learning rate were based on several sensitivity tests conducted. The sensitivity tests involved the changing

of the learning rate and sigma values to understand how each parameter altered the SOM output. Generally, as the learning rate increased the SOM system became increasingly unstable. The maximum learning rate tested was 1 while the best SOM outputs were observed with rates < 0.005. As mentioned in Chapter 2 section 2.3.3., the sigma values were set to 1-y, however, sigma values < 1-y were also tested. Similar to the learning rates, the reduction in the sigma value resulted in the SOM system becoming unstable.

The winning SOM displays low-pressure systems located in the lower lefthand corner of the SOM (Fig. 25). Furthermore, a clear gradient in patterns is seen from high-pressure to low-pressure systems. Minimal distortion is present in the SOM and data is equally distributed among nodes (Figs. 26 and 27).

The composite 2 m temperature (˚C) and 10 m wind barb (knots) plot for each SOM node is shown in Fig. 28. A strong geographic signal is seen in the composite temperature. Northern Alaska observes substantially colder temperatures than southern Alaska as to be expected. For all low-pressure system nodes, the prevailing wind direction is a north-northeasterly wind. The mean wind speed for each SOM node for grid point closest to NSA is displayed in Fig. 29. As expected, the strongest winds are associated with the low-pressure systems with a corresponding stronger horizontal surface pressure gradient (Fig. 25). Wind speeds in the low-pressure nodes range from $12.32 - 20.67$ m s^{-1} while high-pressure systems have winds ~7.7 m s^{-1} slower. One high-pressure system node (node 7) had a local maxima in wind speeds with a mean wind speed of 13.13 m s^{-1}, whereas the remaining high-pressure nodes have wind speeds between $7 - 11$ m s^{-1}. A strong gradient in wind speed was present across the SOM.

4.1.2. SOM Discussion

Overall, the SOM is properly categorizing synoptic-scale patterns. The regions of low-pressure systems correspond to the regions of maximum wind speed (associated with a stronger horizontal surface pressure gradient). Additionally, no high-pressure systems are plotted near a low-pressure system within the SOM space. Independent variables such as wind speed/direction and temperature are physically consistent with what is expected. This provides confidence that the SOM can be used to understand patterns associated with blowing snow.

4.2 BLOWING SNOW FREQUENCY

4.2.1. Climatological Frequency

The climatological frequency is defined as the frequency of blowing snow per SOM node for the duration MET data were available at NSA. The meteorological thresholds determined in Chapter 3 are applied to the MET data and segregated according to the SOM nodes. The number of times blowing snow occurred within the node is divided by the total amount of times within the node. This process was done using two methods. The first method derived the frequencies excluding timeframes that the MET reported > 50% missing 5-min time intervals per month and year. The second method used the same methodology; however, the missing data threshold was increased to > 75%. The results of both methods resulted in minor differences (on the order of 0.02% between the 50% and 75% thresholds), therefore the 75% missing data threshold was applied. The climatological frequency for each SOM node from 2003 – 2022 is shown in Fig. 30. The largest blowing snow frequencies are associated with the low-pressure systems. Lower frequencies of blowing snow are seen in the central region of the SOM. High-pressure systems are accompanied by fewer blowing snow cases.

Blowing snow frequency follows a seasonal cycle. The peak winter months show (i.e., December, January, and February) the highest average monthly MET blowing snow frequencies ranging from 20 - 22.7% (Fig. 31). January shows the largest maxima (22.7%). As the winter season progresses, the frequency of blowing snow decreases (Fig. 31). For example, the average blowing snow frequency for March is 18.1% and April is 17.1%. October shows the lowest blowing snow frequency (16.2%). The SOM-only derived blowing snow frequency shows a similar seasonal cycle. November, December, and January have the highest frequencies ranging from 19.5 - 21.6%. October and April show the lowest frequencies (16 - 18%). To quantitatively compare the SOM-only and MET methods, linear regression is performed (Fig. 32). The R-squared value is 0.436.

4.2.2. Climatological Frequency Discussion

The derived climatological frequency of blowing snow aligns with the synoptic-scale patterns depicted in the SOM. The highest blowing snow frequencies occur in the low-pressure nodes with the highest wind speeds and strongest horizontal surface pressure gradient. As the SOM nodes gradually transition to high-pressure systems, the blowing snow frequency gradually decreases (Fig. 30). The LPM-detected mean wind direction for blowing snow was 58˚ while the SOM mean wind direction was 45˚. The nodes associated with the highest blowing snow frequencies align with synoptic-scale patterns favorable for blowing snow. This further proves that the SOM is correctly segregating synoptic-scale patterns and foreshadows the ability of the SOM to classify specific atmospheric processes.

The MET and SOM-only methods show minor differences in the monthly blowing snow frequencies. Both datasets were hypothesized to have minor discrepancies. The discrepancies are likely because the climatological frequency, used to derive the SOM-only values, is based solely

on synoptic scale patterns. The climatological frequency was derived with a temperature parameter; however, when applied to the SOM data, temperature is not directly accounted for. No method will perform perfectly. The climatological frequency (i.e., the SOM-only based method) performed reasonably well, and thus, the climatological frequency of blowing snow can be used to detect blowing snow conditions in the absence of hydrometeor imager data and meteorological data.

4.2.3. Historic Blowing Snow Frequency

A historic record of blowing snow at NSA was calculated from 1979 –2022. The average monthly blowing snow frequencies are shown in Fig. 33. October shows the lowest frequency of blowing snow (16.8%). December, January, and February show the highest frequencies of blowing snow with frequencies ranging from 20 – 22%. The results of this analysis closely resemble the monthly blowing snow frequencies observed using the MET-based method (Fig. 31). The monthly average blowing snow differences for each month are as follows: October (± 2%), November (± 1.9%), December (± 0.06%), January (± 1%), February (± 0.07%), March (± 3.4%), and April (± 3.7%) The saddle seasons display the least amount of blowing snow. October shows a blowing snow frequency of 16.8%, March shows a frequency of 18.6%, and April shows a frequency of 18.4% (Fig. 33).

Summarizing this section, the SOM can be used to objectively classify periods of blowing snow in the absence of ground-based observations. The meteorological thresholds can be used to identify periods of blowing snow when in-situ observations are available. In the absence of in-situ observations, the climatological frequencies of blowing snow can be used in tandem with the SOM to derive blowing snow frequencies. The results of this analysis are a blowing snow "look-up table."

4.3 BLOWING SNOW TRENDS

Blowing snow trends were investigated through linear regression and p-value significance testing with an alpha of 0.05 (95% confidence) using a one-tail test. The goal was to determine if there was an observed change in blowing snow over time and if so, was the trend statistically significant. The linear regression performed on the average annual blowing snow frequency derived from the SOM is displayed in Fig. 34. The calculated percentage of change in blowing snow frequency per decade was -0.49%; however, the statistical significance was weak with a p-value of 0.15. The same analysis used to generate Fig. 34 was used to calculate the slope, percentage of change per decade, and significance for each month within the SOM. The results of this analysis are displayed in Table 9. December observed a percentage of change per decade of -0.09% with a p-value of 0.32. January observed a percentage of change per decade of -0.13% and a p-value of 0.12. March observed a percentage of change per decade of -0.05% and a p-value of 0.51. April observed a percentage of change per decade of -0.07% and a p-value of 0.36. The months of December, January, March, and April displayed a negative slope with weak statistical significance. October observed a percentage of change per decade of 0.11% with a p-value of 0.08. February observed a percentage of change per decade of 0.1% and a p-value of 0.26. The months of February and October displayed a positive slope with weak statistical significance. November observed a percentage of change per decade of -0.17% with a p-value of 0.02. The month of November was the only month that showed a statistically significant.

4.3.1 Blowing Snow Trends Discussion

Annual blowing snow frequencies did not show a significant change due to changing atmospheric patterns. A similar result was found for monthly blowing snow frequencies for all months excluding November. Though no significant changes were observed in blowing snow

frequencies, that does not mean blowing snow frequency is not changing. Temperature within the Arctic has been increasing over the decades. For example, a quick analysis of temperature was performed using the 2 m ERA5 Reanalysis data to compare the percentage of times temperatures $\geq 0\,^{\circ}\text{C}$ for the first decade of data (i.e., 1979 – 1989) and the last decade of data (i.e., 2010 – 2020). From 1979 – 1989 the percentage of times with temperatures $\geq 0\,^{\circ}\text{C}$ was 0.5%, whereas, from 2010 – 2020 that percentage was closer to 2.5%. With a warming climate, patterns that have historically supported blowing snow are no longer supporting blowing snow due to the increasing temperatures and the strength and intensity of these events may be evolving. This notion poses a potential source of error in the derived blowing snow frequencies as the SOM-only method does not directly include temperature.
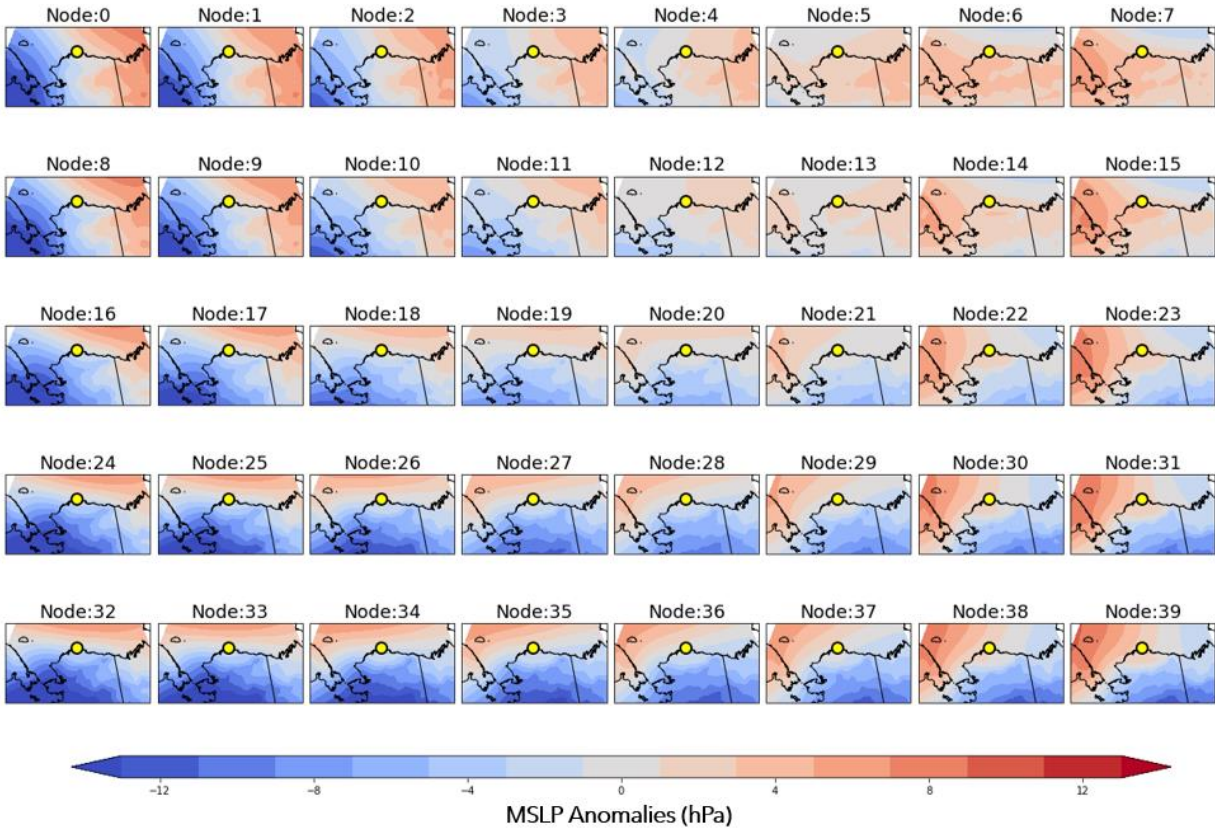
Figure 25: MSLP-only 8 × 5 SOM. Each node is contoured according to MSLP anomalies (hPa). The yellow dot represents the location of NSA.
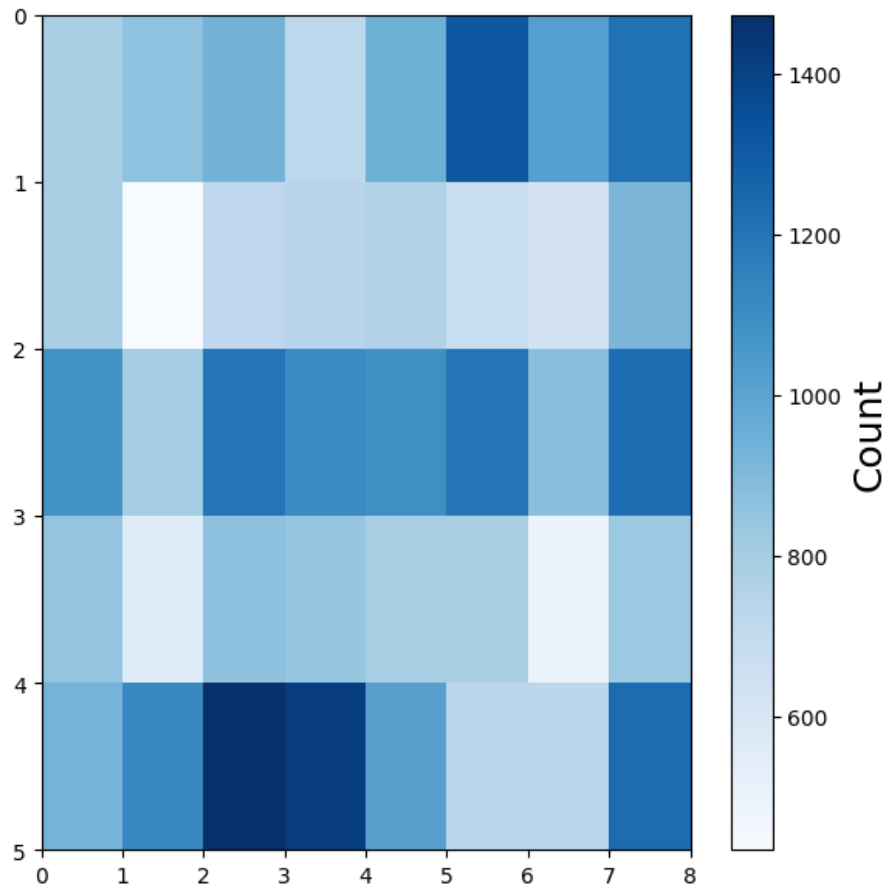
Figure 26: MSLP-only 8 × 5 SOM frequency plot. The values on the *x*-axis and *y*-axis represent the node number.
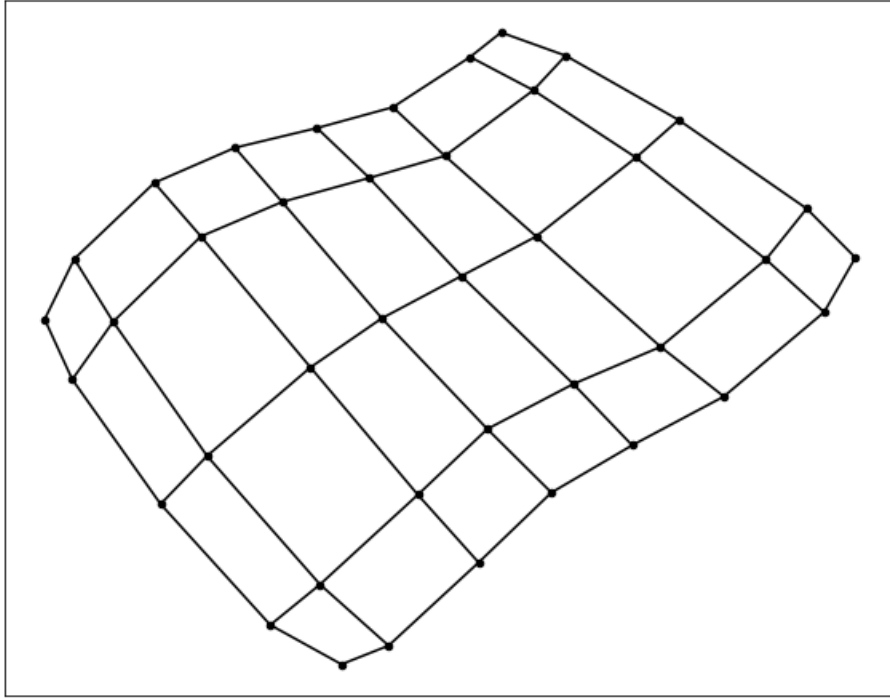
Figure 27: MSLP-only 8 × 5 SOM Sammon plot. Each black dot represents a node.
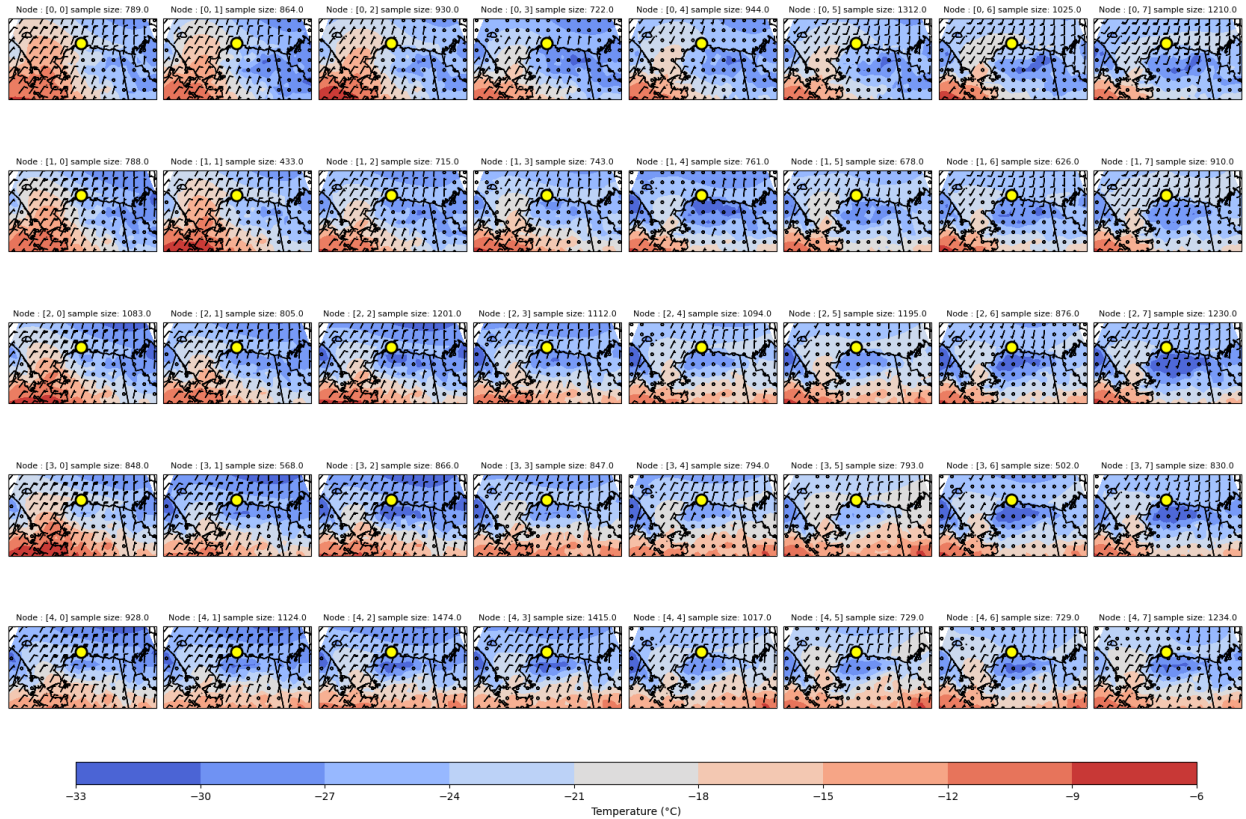
Figure 28: Composite 2 m temperature and 10 m wind barbs for the 8 × 5 SOM. The yellow dot represents the location of NSA. A half barb represents wind speeds of 5 knots or ~ 2.57 m s⁻¹, whereas a full wind barb represents wind speeds of 10 knots or ~ 5.14 m s⁻¹.
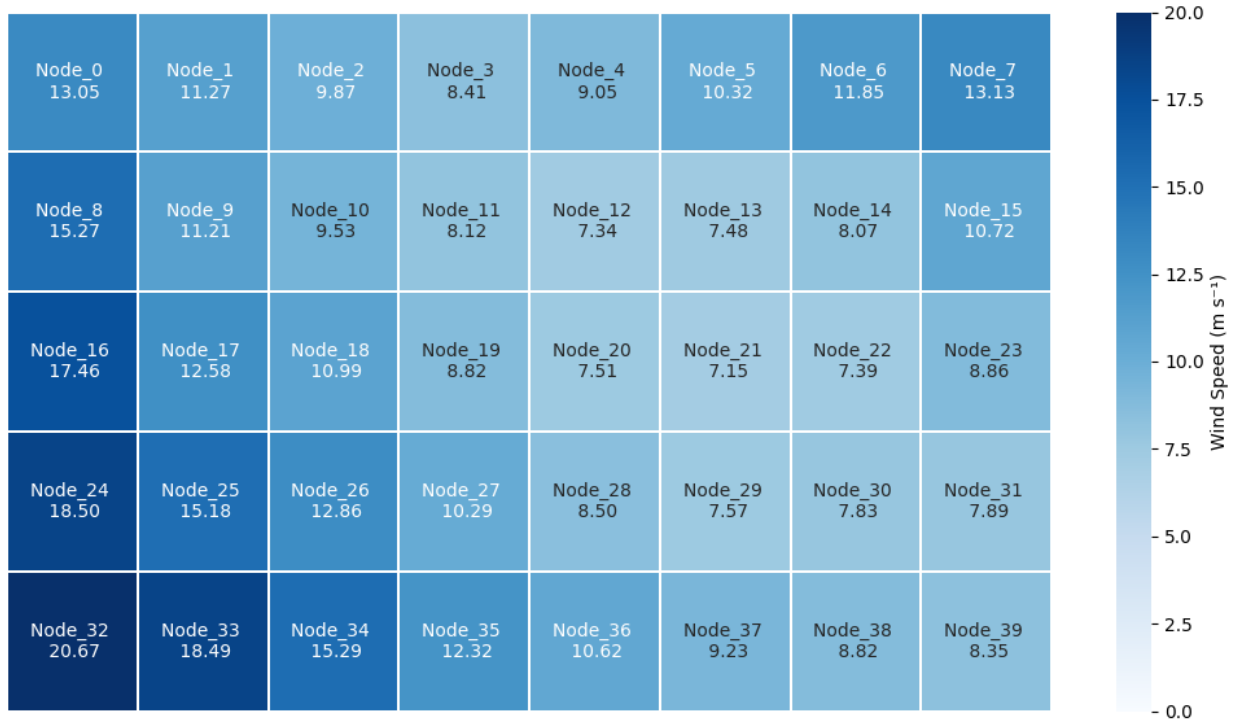
Figure 29: Average 10 m wind speed for NSA for each SOM node.
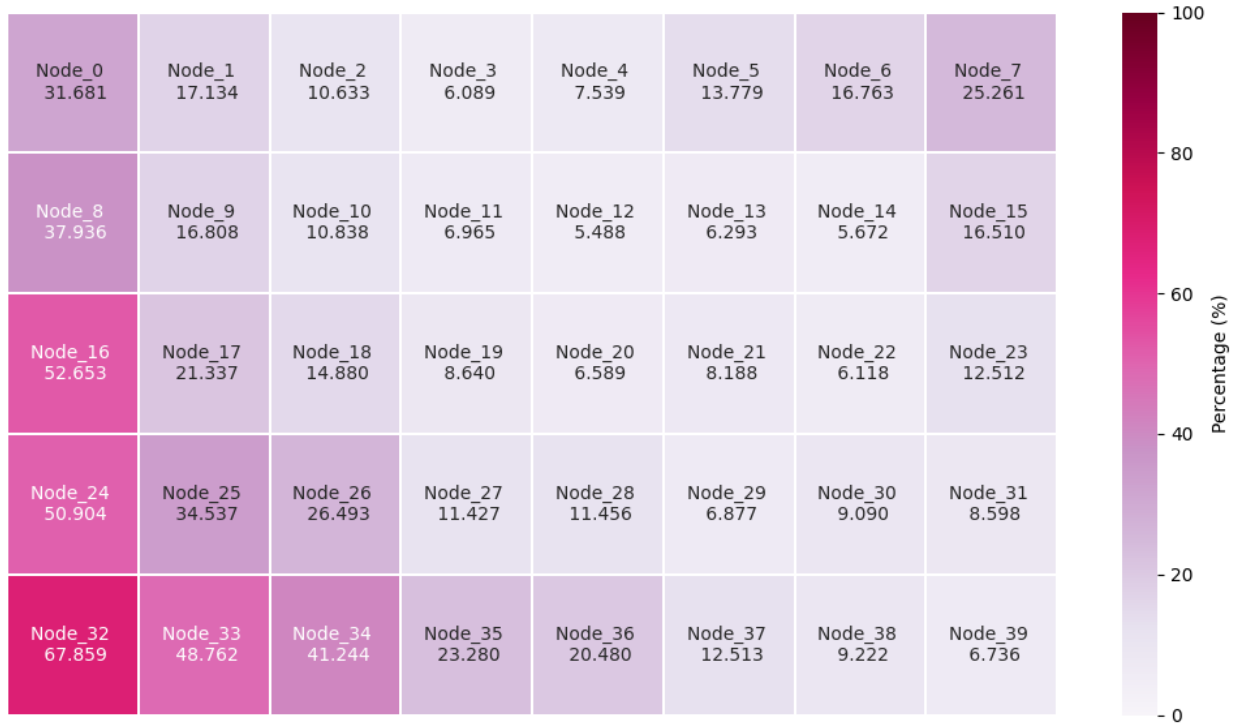
Figure 30: Climatological frequency of blowing snow derived for the MSLP-only 8 × 5 SOM.
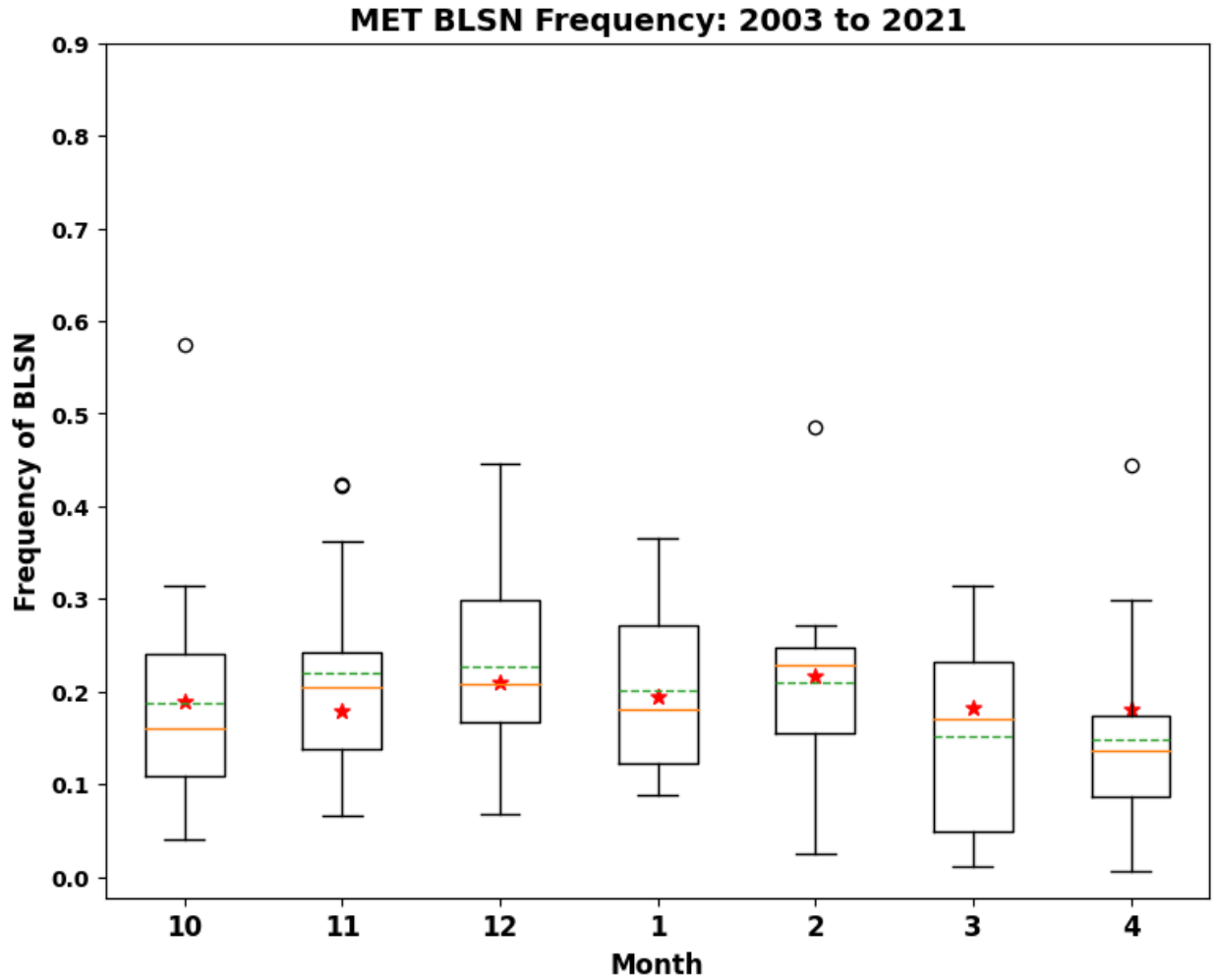
Figure 31: Box and whiskers plot displaying the average blowing snow (BLSN) frequency for each month using the MET method. The green dashed line represents the mean, and the orange solid line represents the median. The 25th, 50th, and 75th percentiles are displayed in addition to the minimum and maximum. The outliers are represented by circles. The red stars represent the SOM-only derived mean monthly blowing snow frequencies for each month from 2003 – 2021.
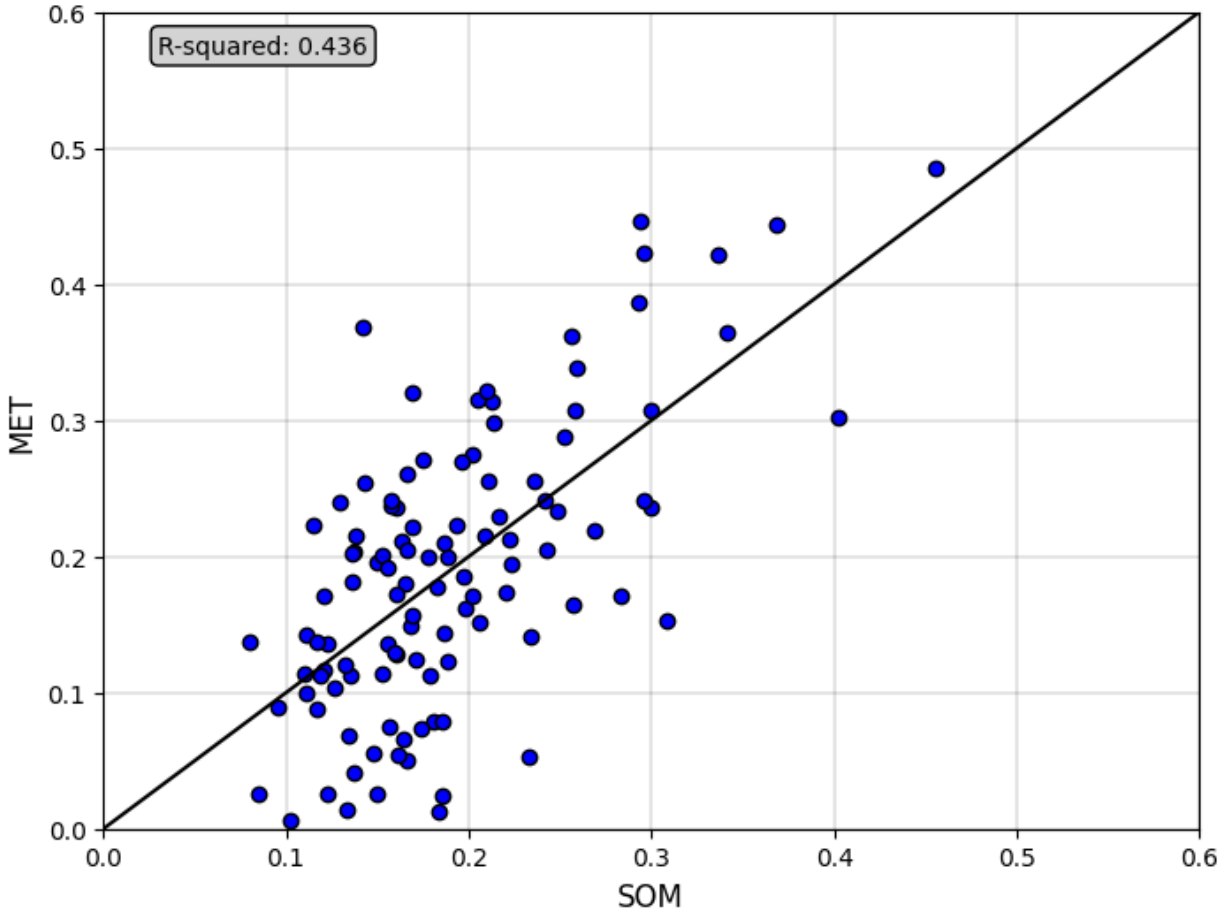
Figure 32: Linear regression analysis performed on the MET and SOM monthly blowing snow frequencies from 2003 – 2021. The black solid line represents the 1-to-1 line.
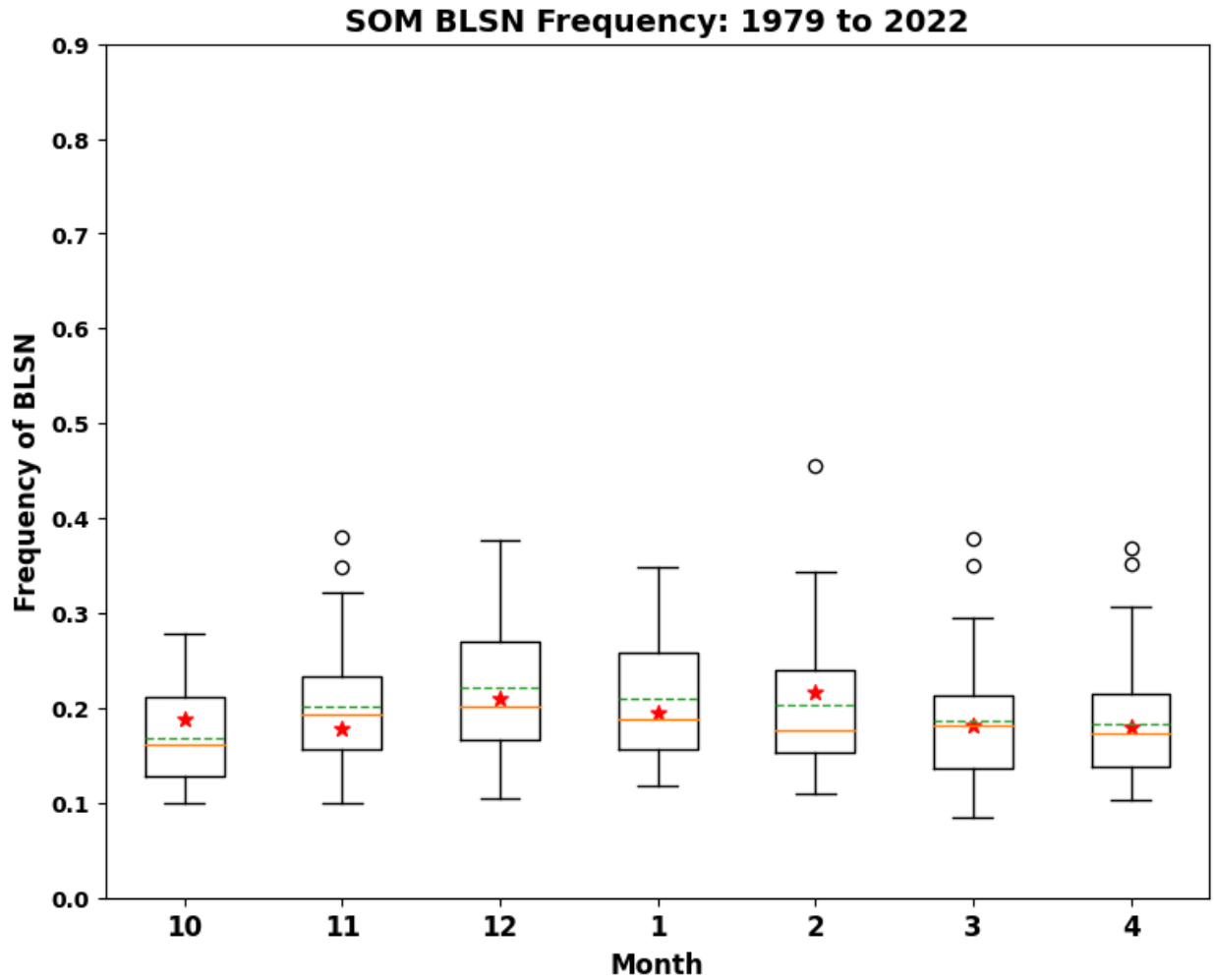
Figure 33: Box and whiskers plot displaying the average blowing snow (BLSN) frequency for each month calculated by applying the climatological frequencies of blowing snow to the SOM. The green dashed line represents the mean, and the orange solid line represents the median. The 25th, 50th, and 75th percentiles are displayed in addition to the minimum and maximum. The outliers are represented by circles. The red stars represent the SOM-only derived mean monthly blowing snow frequencies for each month from 2003 – 2021.
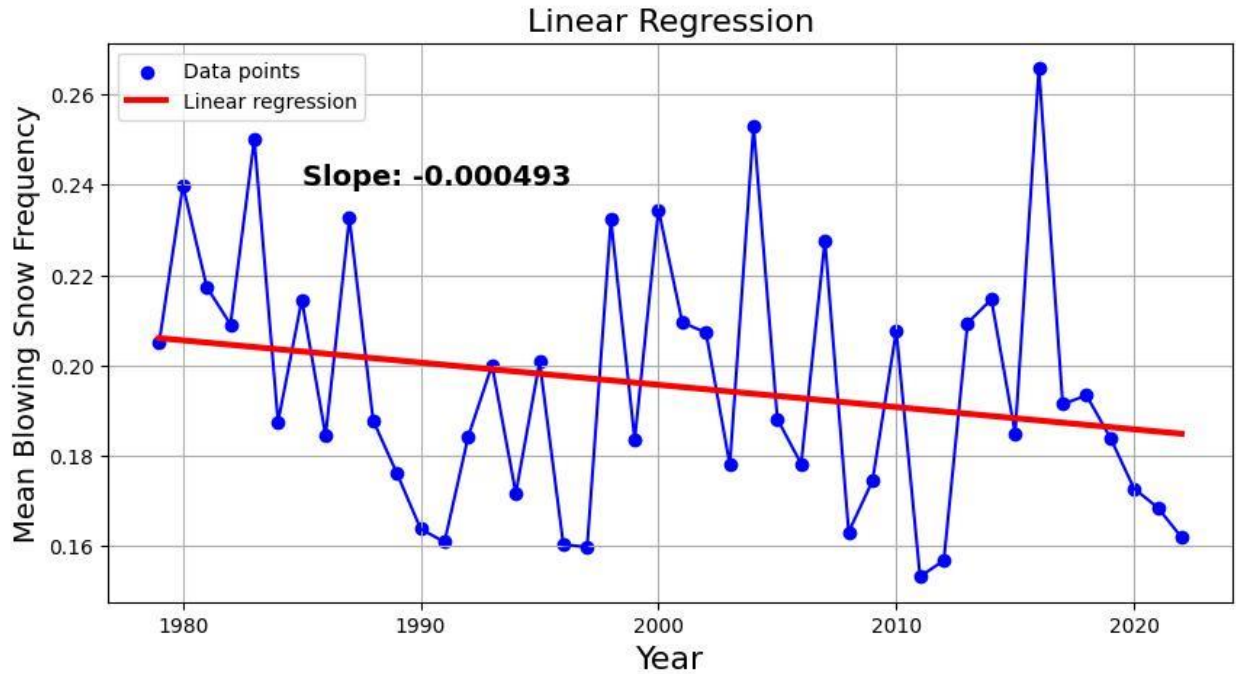
Figure 34: Annual blowing snow frequencies from 1979 to 2022 with an applied linear regression analysis. The annual blowing snow frequency is represented by the blue dots. The linear regression is represented by the red line. Additionally, the slope for the trendline is included within the plot.

Table 9: Monthly slope and significance values for the SOM-derived blowing snow frequencies.

Month	Slope	Significance (p-value)
10	0.0011	0.08
11	-0.0017	0.02
12	-0.0009	0.32
1	-0.0013	0.12
2	0.0010	0.26
3	-0.0005	0.51
4	-0.0007	0.36

CHAPTER 5

CONCLUSIONS AND LIMITATIONS

This thesis had two main objectives. The first was to develop a method to identify blowing snow periods using in situ instrumentation at NSA. The second was to create a long-term record of blowing snow at NSA and analyze if there had been changes in blowing snow cover. Blowing snow is not included in numerical models due to the lack of verification in blowing snow parameters; furthermore, there are limited studies that have focused on the use of in situ instrumentation in the detection of blowing snow at ARM sites. NSA offered an unprecedented opportunity to study blowing snow over a long period of time. The PIP, LPM, and MET datastreams were used to develop a mechanism for blowing snow identification using just meteorological variables. SOMs were used to generate a long-term record and to observe trends in blowing snow. The results of this work will be summarized here.

HYDROMETEOR IMAGER COMPARISON

The two disdrometers selected to represent "ground truth" were the LPM and PIP. To determine the strengths and weaknesses of each instrument in the detection of blowing snow, PSDs segregated by wind speed were made for each. From this analysis, it was found that the PIP struggled with the detection of small diameter particles. The overall concentrations for particles with diameters ≤ 3 mm reported by the PIP were substantially lower than that of the LPM. For example, the 1 Nov. 2019 case study had LPM counts for 5-minute summed time intervals that exceeded 25,000, whereas the PIP only detected counts less than 15,000. The discrepancies in the

overall concentrations of particles reported by the PIP were hypothesized to be due to the imaging process (Maahn et al. 2023). The PIP (as deployed at NSA) was not useful for detecting blowing snow. The LPM can be and was used to represent ground truth at NSA.

METEOROLOGICAL VARIABLES

To develop a method of blowing snow detection based purely on meteorological variables, a variety of analyses were performed to determine the best set of meteorological thresholds in the prediction of blowing snow. 2 m temperature, 2 m relative humidity, 10 m wind speed, and 2 m visibility were investigated using forecaster's 2×2 contingency table analysis.

Through this analysis, the selected parameters for the detection of blowing snow were the temperature dependency ≥ 1000 particle count method. This method resulted in the best blend of (1) high HSS, (2) low frequency bias, and an (3) R-squared value closest to 1. For the selected method, the HSS values were all $> 60\%$ and the R-squared value was 0.85. Additionally, the bias observed was +1.6% which was the closest to truth.

The wind speed and temperature relationship observed in Li and Pomeroy (1997a) was not found in this work. As the temperature decreased from 0 ˚C to -25 ˚C, the wind speed threshold showed no significant change; wind speed magnitudes increased on the order of $2 - 2.5 \text{ ms}^{-1}$. The differences between this study and Li and Pomeroy (1997a) are likely due to several factors. First, this study was not confined to strictly blowing snow events. Second, the vegetation and terrain at NSA varied greatly from the study region in Li and Pomeroy (1997a). Lastly, this study did not exclusively look at wind speed thresholds for blowing snow initialization. Despite this discrepancy, blowing snow periods can be identified with strong confidence using meteorological observations.

CLIMATOLOGICAL FREQUENCY

The meteorological thresholds were applied to the entirety of the MET datastream and then segregated according to the corresponding SOM nodes to derive the climatological frequency. The climatological frequency represented the frequency of blowing snow per SOM node.

The "winning" SOM was an 8 × 5 SOM trained using a learning rate of 0.0005 and a sigma of 4. A composite temperature and wind barb plot was made for the SOM. Furthermore, an average wind speed plot for the center point (i.e., NSA) within the SOM was made. Collectively, these plots displayed the ability of the SOM to properly categorize patterns. The regions of low-pressure systems corresponded to the highest wind speeds. The prevailing wind direction for the low-pressure nodes was a north – north-east.

The nodes associated with the most blowing snow aligned with synoptic scale patterns. The highest blowing snow frequencies were observed in the low-pressure nodes with the highest wind speeds. Additionally, the prevailing wind direction for identified periods of blowing snow by the LPM was a north-north-east direction. Linear regression was performed on the monthly blowing snow frequency identified by the SOM-only method and the MET based method. The linear regression concluded in an R-squared value of 0.436. The SOM was able to discriminate between patterns with and without significant blowing snow conditions. The climatological frequency performed reasonably well and could be used to detect blowing snow in the absence of LPM and MET data.

HISTORIC BLOWING SNOW RECORD AND BLOWING SNOW TRENDS

The climatological frequency represented the expected value of blowing snow for each specific SOM node. The values were applied to the entirety of the SOM to derive a historic record

of blowing snow at NSA from 1979 – 2022. October had the lowest frequency of blowing snow. December and January had the highest frequencies of blowing snow.

Linear regression was performed on the annual mean blowing snow frequencies to analyze trends. There was an observed negative slope, however, there were no statistically significant changes in blowing snow frequency over time due to purely atmospheric patterns. The percentage of change in blowing snow frequencies over the 44-year period was 2.16%. A similar analysis was conducted on the monthly mean blowing snow averages. October and February observed a positive slope; however, the statistical significance was weak. December, January, March, and April observed a negative slope with weak statistical significance. November was the only month that displayed a significant change in blowing snow frequencies solely from changing atmospheric patterns.

LIMITATIONS

Research conducted in the Arctic and Antarctic pose unique challenges. First and foremost, the Arctic climate is rapidly evolving. The direct impacts of climate change on various atmospheric phenomena are unknown. The temperatures within the Arctic are warming 50% faster than US-lower forty-eight (Ballinger et al. 2023). With that being said, the methodology used to derive the climatological frequency and the historic blowing snow record did not directly account for temperature. Patterns that have historically observed blowing snow are no longer observing blowing snow due to increased temperatures. The lack of temperature being accounted for in the climatological frequency and the historic blowing snow record may induce errors within the analysis. Additionally, the meteorological thresholds selected were based on performance against ground truth. Ground truth data (i.e., LPM data) was only available for a ~ 3-year period. The selected meteorological thresholds may not be completely representative due to the relatively short

ground truth dataset. Human-based observations were not available for this site. Furthermore, no cross checking was done for the LPM as the PIP could not be used in the detection of blowing snow conditions.

The second major limitation of Arctic research is sea ice. Sea ice was excluded from this analysis due to the lack of data availability and the complex nature of sea ice. For this study, the main impact sea ice posed was in the form of leeds. A leed is a region of exposed ocean among forming ice sheets. Leeds are most common during the transitional seasons. The presence or lack thereof of leeds is hypothesized to increase and/or decrease blowing snow frequencies. During onshore flow events, the presence of leeds can act to reduce blowing snow frequencies. The impact of leeds becomes minuscule during peak winter. The challenge in accounting for leeds is the region of study is highly localized to the immediate offshore region. Generally, sea ice research is conducted using remote sensing methods that cover a very large geographic region. Focusing the data onto the immediate offshore region would be difficult. The role and extent that ice conditions influence blowing snow occurrences and variability is unknown.

FUTURE WORK

This study was one of few that incorporated in situ instrumentation into the detection of blowing snow periods. Though the yielded results performed reasonably well, the meteorological thresholds applied were derived using a time-limited dataset. The LPM dataset covered ~ 3 years. To optimize the performance of the meteorological thresholds a longer hydrometeor imager dataset is needed. The methodology would be identical; however, more years of data (i.e., > 5-8 years) will ensure that the meteorological thresholds selected truly represent blowing snow conditions and are not biased toward one particular year. Additionally, the data range should be extended to include the entirety of the transitional seasons (i.e., September and May) to fully capture the

seasonal cycle of blowing snow. As mentioned above, the current study omitted the influence of sea-ice. This research should be performed with the inclusion of sea ice data to determine the influence of sea ice.

Future research should focus on applying this methodology to other geographic areas. The results of this study found that the wind speed thresholds increase with increasing temperature for temperatures < - 25˚C. This varied from the results of Li and Pomeroy (1997a). The discrepancies between this study and Li and Pomeroy may be linked to the differences in terrain and geographic location. Applying the methodology in this study to various regions can provide insight on the differences observed between the studies and highlight potential errors in the Li and Pomeroy (1997a) parameters. Understanding the limitations and errors in the Li and Pomeroy (1997a) parameter is critical as most numerical models and blowing snow studies use those blowing snow parameters (Chen et al. 2022). One example location to apply this methodology is North Dakota. North Dakota is highly susceptible to blowing snow and blizzard conditions making it a prime region for blowing snow analysis.

Further investigation is needed to understand how the inclusion of temperature would influence the SOM-only derived blowing snow frequencies. The Arctic is warming and that warming influences the patterns associated with blowing snow. In addition, the occurrence and intensity of blowing snow should be further investigated. The impacts of climate change may be evident in the changing of blowing snow intensity and occurrence. Regardless of geographic location, the intensity of blowing snow and the parameterization of blowing snow intensity is critical to improve blowing snow and blizzard forecasting.

Collectively, these measures would further verify the blowing snow parameters and work toward the inclusion of blowing snow parameters into numerical models.

REFERENCES

Albergel, Clement & Dutra, Emanuel & Munier, S. & Calvet, Jean-Christophe & Muñoz Sabater, Joaquín & Rosnay, Patricia & Balsamo, Gianpaolo. (2018). ERA-5 and ERA-Interim driven ISBA land surface model simulations: Which one performs better?. Hydrology and Earth System Sciences Discussions. 10.5194/hess-2018-117.

Andreas, E. L., Guest, P. S., Persson, P. O. G., Fairall, C. W., Horst, T. W., Semmer, S. R., and Moritz, R. E., Near-surface water vapor over polar sea ice is always near ice saturation, *J. Geophys. Res.*, 107(C10), doi:10.1029/2000JC000411, 2002.

Barnston, A. G., 1992: Correspondence among the Correlation, RMSE, and Heidke Forecast Verification Measures; Refinement of the Heidke Score. *Wea. Forecasting*, **7**, 699–709, https://doi.org/10.1175/1520-0434(1992)007<0699:CATCRA>2.0.CO;2.

Ballinger, T. J., and Coauthors, 2023: Alaska terrestrial and marine climate trends, 1957-2021. *J. Climate*, https://doi.org/10.1175/JCLI-D-22-0434.1, in press.

Bartholomew MJ. 2020. Laser Disdrometer Instrument Handbook. Ed. by Robert Stafford, ARM user facility. DOE/SC-ARM-TR-137. 10.2172/1226796.

Benson, C. S., 1982: Reassessment of winter precipitation on Alaska's Arctic Slope and measurements on the flux of wind blown snow. Rep. UAG R-288, Geophysical Institute, University of Alaska, 26 pp. [Available from Geophysical Institute, University of Alaska, P.O. Box 757320, Fairbanks, AK 99775-7320.].

Berendes, T. A., Berendes, D. A., Welch, R. M., Dutton, E. G., Uttal, T. , and Clothiaux, E. E., "Cloud cover comparisons of the MODIS daytime cloud mask with surface instruments at the north slope of Alaska ARM site," in *IEEE Transactions on Geoscience and Remote Sensing*, vol. 42, no. 11, pp. 2584-2593, Nov. 2004, doi: 10.1109/TGRS.2004.835226.

Brubaker, Michael, Berner, James, Chavan, Raj & Warren, John (2011) Climate change and health effects in Northwest Alaska, Global Health Action, 4:1, DOI: 10.3402/gha.v4i0.8445

Burrows, W. R., and C. J. Mooney, 2021: Blizzard Conditions in the Canadian Arctic: Observations and Automated Products for Forecasting. *Wea. Forecasting*, 36, 1113–1129, https://doi.org/10.1175/WAF-D-20-0077.1.

Cassano, E. N., Lynch, A. H., Cassano, J. J., & Koslow, M. R. (2006). Classification of synoptic patterns in the western Arctic associated with extreme events at Barrow, Alaska, USA. *Climate Research*, *30*(2), 83–97. http://www.jstor.org/stable/24869238

——, Cassano, J. J., and Nolan, M. (2011), Synoptic weather pattern controls on temperature in Alaska, *J. Geophys. Res.*, 116, D11108, doi:10.1029/2010JD015341.

——, Glisan, Justin & Cassano, John & Gutowski, William & Seefeldt, Mark. (2015). Self-organizing map analysis of widespread temperature extremes in Alaska and Canada. Climate Research. 62. 199-218. 10.3354/cr01274.

Cassano, J. J., Cassano, E. N., Seefeldt, M. W., Gutowski, W. J., and Glisan, J. M. (2016), Synoptic conditions during wintertime temperature extremes in Alaska, *J. Geophys. Res. Atmos.*, 121, 3241– 3262, doi:10.1002/2015JD024404.

Chen, Q., Mirrielees, J. A., Thanekar, S., Loeb, N. A., Kirpes, R. M., Upchurch, L. M., Barget, A. J., Lata, N. N., Raso, A. R. W., McNamara, S. M., China, S., Quinn, P. K., Ault, A. P., Kennedy, A., Shepson, P. B., Fuentes, J. D., and Pratt, K. A.: Atmospheric particle abundance and sea salt aerosol observations in the springtime Arctic: a focus on blowing snow and leads, Atmos. Chem. Phys., 22, 15263–15285, https://doi.org/10.5194/acp-22-15263-2022, 2022.

Choi, S., Theys, N., Salawitch, R. J., Wales, P. A., Joiner, J., Canty, T. P., et al. (2018). Link between Arctic tropospheric BrO explosion observed from space and sea-salt aerosols from blowing snow investigated using Ozone Monitoring Instrument BrO data and GEOS-5 data assimilation system. *Journal of Geophysical Research: Atmospheres*, 123, 6954–6983. https://doi.org/10.1029/2017JD026889

Chung, Y., S. Bélair, and J. Mailhot, 2011: Blowing Snow on Arctic Sea Ice: Results from an Improved Sea Ice–Snow–Blowing Snow Coupled System. *J. Hydrometeor.*, 12, 678–689, https://doi.org/10.1175/2011JHM1293.1.

Coleman, J. S. M., and R. M. Schwartz, 2017: An Updated Blizzard Climatology of the Contiguous United States (1959–2014): An Examination of Spatiotemporal Trends. *J. Appl. Meteor. Climatol.*, 56, 173–187, https://doi.org/10.1175/JAMC-D-15-0350.1.

Cook DR and RC Sullivan. 2020. Eddy Correlation Flux Measurement System (ECOR) Instrument Handbook. Ed. by Robert Stafford, ARM user facility. DOE/SC-ARM/TR-052. 10.2172/1467448.

Cox, C. J., and Coauthors, 2017: Drivers and Environmental Responses to the Changing Annual Snow Cycle of Northern Alaska. *Bull. Amer. Meteor. Soc.*, 98, 2559–2577, https://doi.org/10.1175/BAMS-D-16-0201.1.

Cox, C. J., Stone, R. S., Douglas, D. C., Stanitski, D. M., & Gallagher, M. R. (2019). The Aleutian Low-Beaufort Sea Anticyclone: A climate index correlated with the timing of springtime melt in the Pacific Arctic cryosphere. *Geophysical Research Letters*, 46, 7464– 7473. https://doi.org/10.1029/2019GL083306

Daniel, J.S. R.W. Portman, H.L. Miller, S. Solomon, A.L. Langford, C.E. Eubank, R. Schofield, D.D. Turner, and M.D. Shupe, 2006: Cloud property estimates from

zenith spectral measurements of scattered sunlight between 0.9 and 1.7 um. J. Geophys. Res., 111, D16208, doi: 10.1029/2005JD006641.

de Boer, G., and Coauthors, 2018: A Bird's-Eye View: Development of an Operational ARM Unmanned Aerial Capability for Atmospheric Research in Arctic Alaska. *Bull. Amer. Meteor. Soc.*, 99, 1197–1212, https://doi.org/10.1175/BAMS-D-17-0156.1.

Déry, S. J., and M. K. Yau, 2001: Simulation of an Arctic ground blizzard using a coupled blowing snow–atmosphere model. *J. Hydrometeor.*, **2**, 579–598, https://doi.org/10.1175/1525-7541(2001)002<0579:SOAAGB>2.0.CO;2.

——, and L. Tremblay, 2004: Modeling the Effects of Wind Redistribution on the Snow Mass Budget of Polar Sea Ice. *J. Phys. Oceanogr.*, 34, 258–271, https://doi.org/10.1175/1520-0485(2004)034<0258:MTEOWR>2.0.CO;2.

Dewey, K. F., 1977: Lake-effect snowstorms and the record breaking 1976–77 snowfall to the lee of Lakes Erie and Ontario. *Weatherwise*, **30 ,** 228–231.

Dong, X., B. Xi, K. Crosby, C.N. Long, R.S. Stone, and M.D. Shupe, 2010: A 10-year climatology of Arctic cloud fraction and radiative forcign at Barrow, Alaska. J. Geophys. Res., 115, D17212, doi: 10.1029/2009JD013489.

Fang, Xing & Pomeroy, John. (2009). Modeling blowing snow redistribution to prairie wetlands. Hydrological Processes. 23. 2557 - 2569. 10.1002/hyp.7348.

Fargey, S., Henson, W., Hanesiak, J., and Goodson, R. (2014), Characterization of an unexpected snowfall event in Iqaluit, Nunavut, and surrounding area during the Storm Studies in the Arctic field project, *J. Geophys. Res. Atmos.*, 119, 5492–5511, doi:10.1002/2013JD021176.

Fehlmann, M., Rohrer, M., von Lerber, A., & Stoffel, M. (2020). Automated precipitation monitoring with the Thies disdrometer: biases and ways for improvement. *Atmospheric Measurement Techniques*, *13*(9), 4683-4698.

Gelaro, R., and Coauthors, 2017: The Modern-Era Retrospective Analysis for Research and Applications, Version 2 (MERRA-2). *J. Climate*, 30, 5419–5454, https://doi.org/10.1175/JCLI-D-16-0758.1.

Gervais, M., E. Atallah, J. R. Gyakum, and L. B. Tremblay, 2016: Arctic Air Masses in a Warming World. *J. Climate*, 29, 2359–2373, https://doi.org/10.1175/JCLI-D-15-0499.1.

Gold, S., E. White, W. Roeder, M. McAleenan, C. S. Kabban, and D. Ahner, 2020: Probabilistic Contingency Tables: An Improvement to Verify Probability Forecasts. *Wea. Forecasting*, **35**, 609–621, https://doi.org/10.1175/WAF-D-19-0116.1.

Gong, X., Zhang, J., Croft, B. *et al.* Arctic warming by abundant fine sea salt aerosols from blowing snow. *Nat. Geosci.* 16, 768–774 (2023). https://doi.org/10.1038/s41561-023-01254-8

Gossart, A., Souverijns, N., Gorodetskaya, I. V., Lhermitte, S., Lenaerts, J. T. M., Schween, J. H., et al. (2017). Blowing snow detection from ground-based ceilometers: Application to East Antarctica. *The Cryosphere*, 11(6), 2755–2772. https://doi.org/10.5194/tc-11-2755-2017

Gromke, C., Horender, S., Walter, B., & Lehning, M. (2014). Snow particle characteristics in the saltation layer. *Journal of Glaciology, 60*(221), 431-439. doi:10.3189/2014JoG13J079

Gultepe, I., A. J. Heymsfield, P. R. Field, and D. Axisa, 2017: Ice-Phase Precipitation. *Meteor. Monogr.*, **58**, 6.1–6.36, https://doi.org/10.1175/AMSMONOGRAPHS-D-16-0013.1.

Gutiérrez, J.M., Cano, R., Cofiño, A.S. and Sordo, C. (2005), Analysis and downscaling multi-model seasonal forecasts in Peru using self-organizing maps. Tellus A, 57: 435-447. https://doi.org/10.1111/j.1600-0870.2005.00128.x

Hartmann, B., and G. Wendler, 2005: The Significance of the 1976 Pacific Climate Shift in the Climatology of Alaska. *J. Climate*, 18, 4824–4839, https://doi.org/10.1175/JCLI3532.1.

Helms, C. N., Munchak, S. J., Tokay, A., and Pettersen, C.: A comparative evaluation of snowflake particle shape estimation techniques used by the Precipitation Imaging Package (PIP), Multi-Angle Snowflake Camera (MASC), and Two-Dimensional Video Disdrometer (2DVD), Atmos. Meas. Tech., 15, 6545–6561, https://doi.org/10.5194/amt-15-6545-2022, 2022.

Hersbach, H, Bell, B, Berrisford, P, et al. The ERA5 global reanalysis. *Q J R Meteorol Soc*. 2020; 146: 1999–2049. https://doi.org/10.1002/qj.3803

Hewitson, Bruce C., and Robert G. Crane, eds. *Neural nets: applications in geography: applications for geography*. Vol. 29. Springer Science & Business Media, 1994.

Huang, J. and Jaeglé, L.: Wintertime enhancements of sea salt aerosol in polar regions consistent with a sea ice source from blowing snow, Atmos. Chem. Phys., 17, 3699–3712, https://doi.org/10.5194/acp-17-3699-2017, 2017.

Hunt, A., Watkiss, P. Climate change impacts and adaptation in cities: a review of the literature. *Climatic Change* 104, 13–49 (2011). https://doi.org/10.1007/s10584-010-9975-6

Inatsu, M., S. Kawazoe, and M. Mori, 2021: Trends and Projection of Heavy Snowfall in Hokkaido, Japan, as an Application of Self-Organizing Map. *J. Appl. Meteor. Climatol.*, 60, 1483–1494, https://doi.org/10.1175/JAMC-D-21-0085.1.

Johnson, N. C., S. B. Feldstein, and B. Tremblay, 2008: The Continuum of Northern Hemisphere Teleconnection Patterns and a Description of the NAO Shift with the Use of Self-Organizing Maps. *J. Climate*, 21, 6354–6371, https://doi.org/10.1175/2008JCLI2380.1.

Kay, J. E., M. M. Holland, C. M. Bitz, E. Blanchard-Wrigglesworth, A. Gettelman, A. Conley, and D. Bailey, 2012: The influence of local feedbacks and northward heat transport on the equilibrium Arctic climate response to increased greenhouse gas forcing. *J. Climate*, **25**, 5433–5450, doi:10.1175/JCLI-D-11-00622.1.

Kennedy, A.D., Dong, X. & Xi, B. Cloud fraction at the ARM SGP site: reducing uncertainty with self-organizing maps. *Theor Appl Climatol* **124**, 43–54 (2016). https://doi.org/10.1007/s00704-015-1384-3

——, Trellinger A, Grafenauer T, Gust G. A Climatology of Atmospheric Patterns Associated with Red River Valley Blizzards. *Climate*. 2019; 7(5):66. https://doi.org/10.3390/cli7050066

Kim, S., & Chiang, J. C. H. (2022). Atmospheric river lifecycle characteristics shaped by synoptic conditions at genesis. *International Journal of Climatology*, 42(1), 521–538. https://doi.org/10.1002/joc.7258

Kohonen, T.; "The self-organizing map," in *Proceedings of the IEEE*, vol. 78, no. 9, pp. 1464-1480, Sept. 1990, doi: 10.1109/5.58325.

——, Hynninen, J.; Kangas, J.; Laaksonen, J. SOM_PAK: The self-organizing map program package. Espoo Helsinki Univ. Technol. Lab. Comput. Inf. Sci. 1996, 1, 39–40.

Kulie, M. S., and Coauthors, 2021: Snowfall in the Northern Great Lakes: Lessons Learned from a Multisensor Observatory. *Bull. Amer. Meteor. Soc.*, 102, E1317–E1339, https://doi.org/10.1175/BAMS-D-19-0128.1.

Landrum, L. L., & Holland, M. M. (2022). Influences of changing sea ice and snow thicknesses on simulated Arctic winter heat fluxes. *The Cryosphere*, *16*, 1483-1495. doi:10.5194/tc-16-1483-2022.

Leonard, K., & Maksym, T. (2011). The importance of wind-blown snow redistribution to snow accumulation on Bellingshausen Sea ice. *Annals of Glaciology, 52*(57), 271-278. doi:10.3189/172756411795931651

Lenaerts, J. T. M., Medley, B., van den Broeke, M. R., & Wouters, B. (2019). Observing and modeling ice sheet surface mass balance. *Reviews of Geophysics*, 57, 376–420. https://doi.org/10.1029/2018RG000622

——, Hegerl, G. Relating changes in synoptic circulation to the surface rainfall response using self-organising maps. *Clim Dyn* 44, 861–879 (2015). https://doi.org/10.1007/s00382-014-2169-6.

Letcher, T. W., S. L. LeGrand, and C. Polashenski, 2021: Applying a Physically Based Blowing Snow Diagnostic Parameterization to Improve Wintertime Visibility Forecasts in the WRF Model. *Wea. Forecasting*, **36**, 615–626, https://doi.org/10.1175/WAF-D-20-0106.1.

Li, Long & Pomeroy, John. (1997a). Estimates of Threshold Wind Speeds for Snow Transport Using Meteorological Data. Journal of Applied Meteorology - J APPL METEOROL. 36. 205-213. 10.1175/1520-0450(1997)036<0205:EOTWSF>2.0.CO;2.

——, (1997b), Probability of occurrence of blowing snow, *J. Geophys. Res.*, 102(D18), 21955–21964, doi:10.1029/97JD01522.

Liston, G. E., and M. Sturm, 2002: Winter Precipitation Patterns in Arctic Alaska Determined from a Blowing-Snow Model and Snow-Depth Observations. *J. Hydrometeor.*, 3, 646–659, https://doi.org/10.1175/1525-7541(2002)003<0646:WPPIAA>2.0.CO;2.

——, Itkin, P., Stroeve, J., Tschudi, M., Stewart, J. S., Pedersen, S. H., Reinking, A. K., and Elder, K.: A Lagrangian Snow-Evolution System for Sea-Ice Applications (SnowModel-LG): Part I – Model Description, J. Geophys. Res.-Oceans, 125,e2019JC015913, https://doi.org/10.1029/2019jc015913, 2020a.

Loeb, N. A., & Kennedy, A. (2021). Blowing snow at McMurdo station, Antarctica during the AWARE Field Campaign: Surface and ceilometer observations. *Journal of Geophysical Research: Atmospheres*, 126, e2020JD033935. https://doi.org/10.1029/2020JD033935

——, (2023). Blowing snow at McMurdo station, Antarctica during the AWARE field campaign: Multi-instrument observations of blowing snow. *Journal of Geophysical Research: Atmospheres*, 128, e2022JD037590. https://doi.org/10.1029/2022JD037590

Loikith, P. C., B. R. Lintner, and A. Sweeney, 2017: Characterizing Large-Scale Meteorological Patterns and Associated Temperature and Precipitation Extremes over the Northwestern United States Using Self-Organizing Maps. *J. Climate*, 30, 2829–2847, https://doi.org/10.1175/JCLI-D-16-0670.1.

Lott, N., T. Ross, and M. Sittel, 1996: The winter of '95–'96: A season of extremes. National Climatic Data Center, Tech. Rep. 96-02, Asheville, NC, 15 pp.

Maahn, Maximilian & Moisseev, Dmitri & Steinke, Isabelle & Maherndl, Nina & Shupe, Matthew. (2023). Introducing the Video In Situ Snowfall Sensor (VISSS). 10.5194/egusphere-2023-655.

Mallett, Robbie & Stroeve, J.C. & Tsamados, Dr Michel & Landy, Jack & Willatt, Rosemary & Nandan, Vishnu & Liston, Glen. (2021). Faster decline and higher variability in the sea ice thickness of the marginal Arctic seas when accounting for dynamic snow cover. The Cryosphere. 15. 2429-2450. 10.5194/tc-15-2429-2021.

Mahesh, A., R. Eager, J. R. Campbell, and J. D. Spinhirne, 2003: Observations of blowing snow at the South Pole. Journal of Geophysical Research: Atmospheres, 108, https://doi.org/10.1029/2002JD003327.

McAfee, S. A., 2014: Consistency and the Lack Thereof in Pacific Decadal Oscillation Impacts on North American Winter Climate. *J. Climate*, 27, 7410–7431, https://doi.org/10.1175/JCLI-D-14-00143.1.

Melo, D. B., Sharma, V., Comola, F., Sigmund, A., & Lehning, M. (2022). Modeling snow saltation: The effect of grain size and interparticle cohesion. *Journal of Geophysical Research: Atmospheres*, 127, e2021JD035260. https://doi.org/10.1029/2021JD035260

Meredith, M., Sommerkorn, M., Cassotta, S., Derksen, C., Ekaykin, A., Hollowed, A., Kofinas, G., Mackintosh, A., Melbourne-Thomas, J., Muelbert, M., Ottersen, G., Pritchard, H., and Schuur, E.: Polar Regions, in: IPCC Special Report on the Ocean and Cryosphere in a Changing Climate, edited by: Portner, H.-O., Roberts, D., Masson-Delmotte, V., Zhai, P., Tignor, M., Poloczanska, E., Mintenbeck, K., Alegria, A., Nicolai, M., Okem, A., Petzold, J., Rama, B., and Weyer, N., 203–320, IPCC, 2019.

Mellor, M.: 1965, *Blowing Snow*, CRREL Monograph, Part III, Section A3c, U.S. Army Corps of Engineers, Cold Regions Research and Engineering Laboratory, Hanover, NH, U.S.A., 79 pp.

Meshesha, Derege & Tsunekawa, Atsushi & Tsubo, Mitsuru & Haregeweyn, N. & Amogne, Firew Tegegne. (2016). Evaluation of kinetic energy and erosivity potential of simulated rainfall using Laser Precipitation Monitor. CATENA. 137. 237-243. 10.1016/j.catena.2015.09.017.

Michaelides, Silas & Tymvios, Filippos & Michaelidou, T.. (2009). Spatial and temporal characteristics of the annual rainfall frequency distribution in Cyprus. Atmospheric Research - ATMOS RES. 94. 606-615. 10.1016/j.atmosres.2009.04.008.

Miljković, D., "Brief review of self-organizing maps," *2017 40th International Convention on Information and Communication Technology, Electronics and Microelectronics (MIPRO)*, Opatija, Croatia, 2017, pp. 1061-1066, doi: 10.23919/MIPRO.2017.7973581.

Munich RE, 2015: Winter storm/blizzard/ice storm. Munich Reinsurance America, Inc., accessed 1 November 2015. [Available online at http://www.munichre.com/us/weather-resilience-and-protection/rise-weather/weather-events/winter-storm/index.html.]

Mwasiagi, Josphat Igadwa, ed. *Self Organizing Maps: Applications and Novel Algorithm Design*. BoD–Books on Demand, 2011.

Naaim-Bouvet, Hervé Bellot, Kouichi Nishimura, Christophe Genthon, Cyril Palerme, et al.. How to detect snow fall occurence during blowing snow event?. 2012 International Snow Science Workshop, Sep 2012, Anchorage, United States. p. 976 - p. 982. hal-00744559

Natita, W., Wiboonsak, W., & Dusadee, S. (2016). Appropriate Learning Rate and Neighborhood Function of Self-organizing Map (SOM) for Specific Humidity Pattern Classification over Southern Thailand. International Journal of Modeling and Optimization, 6, 61-65.

Palm, S. P., Yang, Y., Spinhirne, J. D., and Marshak, A. (2011), Satellite remote sensing of blowing snow properties over Antarctica, *J. Geophys. Res.*, 116, D16123, doi:10.1029/2011JD015828.

Persad, G, B H Samset, L J Wilcox, Robert J Allen, Massimo A Bollasina, Ben B B Booth, Céline Bonfils, et al. 2023. "Rapidly Evolving Aerosol Emissions Are a Dangerous Omission from Near-Term Climate Risk Assessments". *Environmental Research: Climate* 2 (3). IOP Publishing: 032001. doi:10.1088/2752-5295/acd6af.

Pettersen C, Bliven LF, von Lerber A, Wood NB, Kulie MS, Mateling ME, Moisseev DN, Munchak SJ, Petersen WA, Wolff DB. The Precipitation Imaging Package: Assessment of Microphysical and Bulk Characteristics of Snow. *Atmosphere*. 2020; 11(8):785. https://doi.org/10.3390/atmos11080785

——, Kulie MS, Wood NB, Shates JA, Anderson J, Mateling ME, Petersen WA, von Lerber A, Wolff DB. The Precipitation Imaging Package: Phase Partitioning Capabilities. *Remote Sensing*. 2021; 13(11):2183. https://doi.org/10.3390/rs13112183

Pickering, Ben & III, Ryan & Harrison, Dawn. (2019). The Disdrometer Verification Network (DiVeN): a UK network of laser precipitation instruments. Atmospheric Measurement Techniques. 12. 5845-5861. 10.5194/amt-12-5845-2019.

Pomeroy JW, Gray DM. 1990. Saltation of snow. Water Resources Research. 26: 1583-1594.

——, and Male, D. (1988). Optical Properties of Blowing Snow. *Journal of Glaciology, 34*(116), 3-10. doi:10.3189/S0022143000008996

——, and Male DH. 1992. Steady-state suspension of snow. Journal of Hydrology. 136: 275-301.

——, Marsh, Philip & GRAY, D.. (1997). Application of distributed blowing snow model to the Arctic. Hydrological Processes. 11. 1451 - 1464. 10.1002/(SICI)1099-1085(199709)11:11<1451::AID-HYP449>3.0.CO;2-Q.

Ritsche et al. ARM Surface Meteorology Systems Handbook. 2011. 10.2172/1007926.

Schaefer, J. T., 1990: The Critical Success Index as an Indicator of Warning Skill. *Wea. Forecasting*, **5**, 570–575, https://doi.org/10.1175/1520-0434(1990)005<0570:TCSIAA>2.0.CO;2.

Schwartz, R. M., and T. W. Schmidlin, 2002: Climatology of Blizzards in the Conterminous United States, 1959–2000. *J. Climate*, 15, 1765–1772, https://doi.org/10.1175/1520-0442(2002)015<1765:COBITC>2.0.CO;2.

Sheridan, S. C., & Lee, C. C. (2011). The self-organizing map in synoptic climatological research. Progress in Physical Geography: Earth and Environment, 35(1), 109–119. https://doi.org/10.1177/0309133310397582

Shulski, Martha D. and Mark W. Seeley. "Application of Snowfall and Wind Statistics to Snow Transport Modeling for Snowdrift Control in Minnesota." Journal of Applied Meteorology 43 (2004): 1711-1721.

Shulski, M., Wendler, G., The Climate of Alaska, University of Alaska Press (2007), p. 288, https://scholar.google.com/scholar_lookup?title=The%20Climate%20of%20Alaska&publication_year=2007&author=M.%20Shulski&author=G.%20Wendler

Shupe, M.D., P. Kollias, P.O.G. Persson, and G.M. McFarquhar, 2008: Vertical motions in Arctic mixed-phase stratus. J. Atmos. Sci., 65, 1304-1322.

Smith, Elyse. "Timeline of the Blizzard of 2022." *Wgrz.com*, 31 Dec. 2022, https://www.wgrz.com/article/weather/severe-weather/timeline-of-the-wny-blizzard-of-2022-buffalo-niagara/71-31e533fe-edd2-4201-86c8-2fe678fb784e.

Sullivan R, D Cook, V Ghate, V Kotamarthi, and Y Feng. 2019. "Improved Spatiotemporal Representativeness and Bias Reduction of Satellite-Based Evapotranspiration Retrievals via Use of In Situ Meteorology and Constrained Canopy Surface Resistance." *Journal of Geophysical Research: Biogeosciences*, , 10.1029/2018JG004744. ONLINE. Research Highlight

Taylor, P. The Thermodynamic Effects of Sublimating, Blowing Snow in the Atmospheric Boundary Layer. *Boundary-Layer Meteorology* **89**, 251–283 (1998). https://doi.org/10.1023/A:1001712111718

Tobin, D. C., Revercomb, H. E., Knuteson, R. O., Lesht, B. M., Strow, L. L., Hannon, S. E., Feltz, W. F., Moy, L. A., Fetzer, E. J., and Cress, T. S. (2006), Atmospheric Radiation Measurement site atmospheric state best estimates for Atmospheric Infrared Sounder temperature and water vapor retrieval validation, *J. Geophys. Res.*, 111, D09S14, doi:10.1029/2005JD006103.

Wang, Z., Bi, L., Yi, B., & Zhang, X. (2019). How the inhomogeneity of wet sea salt aerosols affects direct radiative forcing. *Geophysical Research Letters*, 46, 1805–1813. https://doi.org/10.1029/2018GL081193

Warren, S. G., Rigor, I. G., Untersteiner, N., Radionov, V. F., Bryazgin, N. N., Aleksandrov, Y. I., and Colony, R.: Snow depth on Arctic sea ice, J. Climate, 12, 1814–1829, https://doi.org/10.1175/1520-0442(1999)012<1814:SDOASI>2.0.CO;2, 1999.

Wilks, D. S., 2019: Forecast Verification. Statistical Methods in the Atmospheric Sciences, 4thed. Elsevier, 374-38

Yu T, Chandrasekar V, Xiao H, Joshil SS. Characteristics of Snow Particle Size Distribution in the PyeongChang Region of South Korea. *Atmosphere*. 2020; 11(10):1093. https://doi.org/10.3390/atmos11101093

Zhang D, Comstock J, Xie H, Wang Z. Polar Aerosol Vertical Structures and Characteristics Observed with a High Spectral Resolution Lidar at the ARM NSA Observatory. *Remote Sensing*. 2022; 14(18):4638. https://doi.org/10.3390/rs14184638.

——, Li, Z., Chen, H., and Cribb, M. (2013), Validation of a radiosonde-based cloud layer detection method against a ground-based remote sensing method at multiple ARM sites, *J. Geophys. Res. Atmos.*, 118, 846– 858, doi:10.1029/2012JD018515.

——, Wang, Z., Luo, T., Yin, Y., and Flynn, C. (2017), The occurrence of ice production in slightly supercooled Arctic stratiform clouds as observed by ground-based remote sensors at the ARM NSA site, *J. Geophys. Res. Atmos.*, 122, 2867– 2877, doi:10.1002/2016JD026226.

——, Wang, Jianwu & Jin, Daeho & Oreopoulos, Lazaros & Zhang, Zhibo. (2018). A Deterministic Self-Organizing Map Approach and its Application on Satellite Data based Cloud Type Classification. 2027-2034. 10.1109/BigData.2018.8622558.